MASTERARBEIT | MASTER'S THESIS

Titel | Title

Searching for Chemically Peculiar stars in stellar associations

verfasst von | submitted by

Lukas Kueß BSc

angestrebter akademischer Grad | in partial fulfilment of the requirements for the degree of

Master of Science (MSc)

Wien | Vienna, 2024

Studienkennzahl lt. Studienblatt | Degree programme code as it appears on the student record sheet:	UA 066 861
Studienrichtung lt. Studienblatt | Degree programme as it appears on the student record sheet:	Masterstudium Astronomie
Betreut von | Supervisor:	Univ.-Doz. Dr. Ernst Paunzen

Caeli enarrant gloriam Dei et opera manuum eius adnuntiat firmamentum

Ps 19,2

Declaration of Authorship

This thesis is my own work based on research conducted by myself. Any knowlegde adapted from research by other scientists has been indicated to the best of my knowledge and belief and can be found in the bibliography. If problems of copyright infringement arise, please contact me so that these issues can be resolved.

Lukas Kueß, 2024

Acknowledgements

I want to thank my supervisor Ernst Paunzen for what felt like infinite (not always deserved) patience and the guiding I was given during this work. Additionally, I thank Stefan Hümmerich for helping me with the classification of the LAMOST spectra, Stefan Meingast and Alena Rottensteiner for valuable ideas and the data I needed to go after them.
As for my friends, I have to give thanks for Flo and Annica. You two have been motivating me and showing interest into my work, spending time with you and your wonderful daughter was always a very needed distraction. My colleagues Vali and Julia for sharing the braincell and lending it to me in crucial situations.
Last but not least, I have to thank my girlfriend Lena, just for existing (and for believing that I was intelligent).
A last special thank you goes to "Der Heilige Ofenkäse". Ofi, you were a great form of entertainment and motivation (you know what you did) during the time of me working on this thesis.

This thesis makes use of data products from the Two Micron All Sky Survey, which is a joint project of the University of Massachusetts and the Infrared Processing and Analysis Center/California Institute of Technology, funded by the National Aeronautics and Space Administration and the National Science Foundation. This thesis includes data collected by the TESS mission, which are publicly available from the Mikulski Archive for Space Telescopes (MAST). Funding for the TESS mission is provided by NASA's Science Mission directorate. This work has made use of data from the European Space Agency (ESA) mission *Gaia* (`https://www.cosmos.esa.int/gaia`), processed by the *Gaia* Data Processing and Analysis Consortium (DPAC, `https://www.cosmos.esa.int/web/gaia/dpac/consortium`). Funding for the DPAC has been provided by national institutions, in particular the institutions participating in the *Gaia* Multilateral Agreement. Guoshoujing Telescope (the Large Sky Area Multi-Object Fiber Spectroscopic Telescope LAMOST) is a National Major Scientific Project built by the Chinese Academy of Sciences. Funding for the project has been provided by the National Development and Reform Commission. LAMOST is operated and managed by the National Astronomical Observatories, Chinese Academy of Sciences. This Thesis makes use of VOSA, developed under the Spanish Virtual Observatory (`https://svo.cab.inta-csic.es`) project funded by MCIN/AEI/10.13039/501100011033/ through grant PID2020-112949GB-I00. VOSA has been partially updated by using funding from the European Union's Horizon 2020 Research and Innovation Programme, under Grant Agreement nº 776403 (EXOPLANETS-A).

Abstract

The chemically peculiar (CP) stars on the upper main sequence of the Hertzsprung-Russell diagram (HRD) have been puzzling astronomers since their discovery in the end of the nineteenth century. A research question not answered to satisfaction up until this day has always been the origin and evolution of the peculiarities found in the spectra of those stars, especially in the youngest of those objects.
This thesis aims to shed some light on the question of the origin of peculiarities in stellar associations, some of the youngest known aggregations of stars.
I use literature collections of open clusters and associations and re-clustered the stars in their regions to determine membership probabilities using . These members ($p_{memb} \geq 0.5$) were then analysed with different methods to determine which ones are likely to be CP stars. First, I used synthetic photometry in the well-established Δa system on the new low resolution *Gaia* BP/RP spectra to look for the flux depression at $\lambda5200$. Additionally, spectral data from LAMOST were classified using MKCLASS. At last, a light curve analysis on a nearby (up to about 300 pc) subset was performed using frequency analysis on photometric data from the TESS satellite.
Another interest regarding the early stages of stellar evolution of CP stars was to determine which ones are still in their Pre-Main Sequence (PMS) phase. Here, a combination of fitting the Spectral Energy Distribution (SED) and a new method for finding emission line stars by synthetic photometry was performed.
Out of all the ~330 thousand stars in the target list, approximately 970 are likely CP stars or candidates. From those, around 100 stars still seem to be in their Pre-Main Sequence (PMS) phase.
I conclude that it is possible to find CP stars in young aggregations of stars. Additionally, there is a number of CP stars that appear to still be in their PMS evolution. This may allow us to constrain effects that lead to the formation of such objects and can improve the theories dealing with star formation. To do this, the stars need to be observed in much more detail to find out what exactly is going on.

Kurzfassung

Die chemisch pekuliaren (CP) Sterne der oberen Hauptreihe im Hertzsprung-Russel Diagramm haben Astronominnen und Astronomen seit ihrer Entdeckung am Ende des 19. Jahrhunderts vor viele Fragen gestellt. Eine Frage, die bis heute nicht zufriedenstellend geklärt werden konnte ist die Frage nach dem Ursprung der Pekuliaritäten, speziell in den jüngsten dieser Objekte.

Die vorliegende Masterarbeit versucht, einen Beitrag zur Lösung der Frage nach dem Ursprung der Pekuliaritäten in Sternassoziationen, einigen der jüngsten Ansammlungen von Sternen, zu leisten.

Ich nutze Kataloge von offenen Sternhaufen und Assoziationen und bestimme deren Mitglieder und Mitgliedswahrschinlichkeiten eben dieser mit dem HDBSCAN-Algorithmus. Die Mitglieder mit hoher Wahrscheinlichkeit ($p_{memb} \geq 0.5$) wurden dann mit verschiedenen Methoden Analysiert, um herauszufinden, welche davon CP-Sterne sind oder sein könnten. Zuerst, habe ich mithilfe von synthetischer Photometrie im gut etablierten Δa System anhand der neuen *Gaia* BP/RP Spektren mit niedriger Auflösung nach der bekannten Flussdepression bei $\lambda 5200$ gesucht. Weiters kamen LAMOST-Spektren zum Einsatz, die mithilfe des Programms MKCLASS automatisch klassifiziert wurden. Schlussendlich habe ich anhand von Lichtkurven des Satelliten TESS an einer Untermenge der Sterne (näher als etwa 300pc) mithilfe einer Frequenzanalyse nach charaktaristischer Variabilität gesucht.

Eine weitere intressante Fragestellung, insbesondere in Hinblick auf die frühesten Phasen der Sternentwicklung, ist es, zu bestimmen, welche Objekte sich immer noch im Entstehungsprozess befinden. Hierfür wurde eine Kombination aus photometrischen Messungen der Spektralen Energieverteilung (SED) und einer neuen Methode, die Emissionslinien mittels synthetischer Photometrie entdecken kann von mir angewandt.

Etwa 970 von den etwa 330 Tausend Sternen in der endgültigen Liste an möglichen Objekten zeigen Charakteristiken von CP Sternen. Etwa 100 von diesen zeigen auch Anzeichen von Sternen in ihrer Entstehungsphase.

Daraus schließe ich, dass es durchaus CP Sterne in den jüngeren Sternhaufen und Assoziationen gibt, wovon einige sich noch in der Entstehungsphase befinden. Dies könnte uns erlauben, die Theorien der Entstehung dieser Objekte nochmals zu verfeinern oder weiterzuentwickeln. Dafür werden jedoch detailliertere Beobachtungen und Analysen vonnöten sein.

Contents

List of Tables

List of Figures

1. Chemically peculiar stars and Stellar Associations

This chapter gives an overview what chemically peculiar (CP) stars and stellar associations are and which processes are important in those objects.

1.1. Chemically peculiar stars

When Maury & Pickering (1897) classified spectra of stars, some of those stars, for example α^2 CVn, were described as having *peculiar* spectra. In the case of α^2 CVn, it was noted that the star shows a weak Ca K line compared to stars of similar spectra and simultaneously a strong Si II doublet around λ4130 was reported.
After observing the peculiar star 78 Vir, Babcock (1947) noticed the presence of a rather strong magnetic field. This marks the beginning of the so-called magnetic A type stars.

Subsequently, more and more peculiar stars were discovered and finally, Preston (1974) put together a classification scheme for those stars. This classification, as seen in Table 1.1, is still widely used today, with some refinement by the work of Smith (1996) that included the λ Boo stars and the He-rich stars. This new classification can be seen in Table 1.2.

CP group	**Classical name**	**Discovery criteria**	$T_{eff}[K]$
1	metallic line Am	weak Ca II and/or Sc II enhanced heavy metals	7000 - 10000
2	magnetic, mCP Ap	enhanced Si, Cr, Sr, Eu et al.	8000 - 15000
3	HgMn	enhanced Hg II λ3984 Mn II	10000 - 15000
4	He-weak	Weak helium lines	13000 - 20000

Table 1.1.: Classical classification scheme for CP stars, adopted from Preston (1974)

Smith (1996) also lists the spectral types and one can easily see from Table 1.2 that the chemical peculiarities arise in spectral types B to F.

Classical name	Type Preston	Discovery criteria	SpT	$T_{\text{eff}}[K]$
λ Boo	-	weak Mg weak metals	A0 - F0	7500 - 9000
Am/Fm	CP1	weak Ca II/Sc II enhanced metals	A0 - F4	7000 - 10000
Bp/Ap	CP2	enhanced Sr, Cr Eu and/or Si	B6 - F4	7000 - 16000
HgMn	CP3	enhanced Hg II and/or Mn II	B6 - A0	10500 - 16000
He-weak	CP4	weak He I compared with colours	B2 - B8	14000 - 20000
He-rich	-	enhanced He I compared with colours	B2	20000 - 25000

Table 1.2.: "Newer" classification of CP stars, adopted from Smith (1996)

1.1.1. Origin of the peculiarities

The book "*Stellar spectral classification*" by Gray & Corbally (2009) gives an overview of the processes that lead or can lead to the peculiarities described in the section above, especially the ones mentioned in Table 1.1. Here, a short summary of the processes is given.

CP1 (Am/Fm) stars

Generally, in A-type stars, we can observe a phenomenon called *chemical separation*. This effect is a consequence of the interplay of radiative accelerations of some elements and gravitational settling of others. When an atom or ion absorbs a photon, the momentum of the photon gets transferred to the atom/ion which results in a net force in the outward direction since the radiation field is directed towards the surface of the star. When the outwards acceleration overwhelms the gravitational acceleration, the atom/ion rises to the surface. This is especially true for elements with a large number of spectral lines in the ultra-violet (UV) part of the spectrum (e.g. Fe, Ni, Cr). In "normal" A-type stars, those effects are overwhelmed by the fast rotation ($v \sin i$[1] $\gtrsim$ 100km s^{-1}) where meridional circulation sets in and mixes the envelope of the star. Since all, or at least most of the Am stars seem to be slow rotators ($v \sin i \lesssim$ 100km s^{-1}) now meridional convection can occur and the chemical separation is present. This slow rotation may be a result of all or most of those stars being found in binary systems (Paunzen, 2020) which resulted in tidal braking in at least one of the members (Abt, 2009).

[1] $v \sin i$ is the line-of-sight rotational velocity. v itself is the rotational velocity on the equator of the star. Since any given star is most likely observed at an angle i with respect to the rotation axis, the factor $\sin i$ is introduced to correct the measurement for an unknown inclination angle. Thus, the quantity $v \sin i$ is a lower limit for the true rotational velocity of the star. Per definition, if we look at the equator, the angle $i = 90°$ and thus $\sin i = 1$ which means we measure the true rotational velocity.

CP2 (Bp/Ap) stars

The origin of those peculiarities is generally attributed to the present of the strong magnetic fields (up to tens of kG, Bychkov et al. (2021)) in this subclass. In addition to the chemical separation described above, we now also have to consider the forces acting on ions in the presence of a magnetic field: charged ions get captured and thus have a lower diffusion rate, leading to spotted abundance anomalies in the vicinity of the magnetic poles. This then can be observed as spectroscopic (in the lines of the element/ion in question) and/or photometric variability. In the case of Si I, however, the same principle as in the Am stars is at work, meaning, we can observe Si lines in regions not aligned with the magnetic poles of the star.

CP3 (HgMn) stars

Like the Am/Fm stars, most of the HgMn stars seem to be binaries and thus slow rotators. Adelman et al. (2003) have inferred a connection in the evolution of HgMn stars and Am/Fm stars and thus a similar origin of the peculiarities can be an explanation of the peculiarities(Dolk et al., 2003).

CP4 (He-weak) and He-strong stars

This subclass can be seen as an extension of the CP2 stars onto hotter spectral types (B2-B8, see Tab. 1.2) and thus have similar explanations for the origin of the peculiarities, although the temperatures in these hotter stars tend to favour the lighter elements such as helium. They also show similar spectral and photometric variability as the CP2 stars (Pedersen & Thomsen, 1977).

λ Bootis stars

Here, multiple theories have been developed. For example, Michaud & Charland (1986) suggested that the under-abundances in this group are explained by diffusion and mass-loss. A higher mass-loss rate ($\sim 10^{-13}\mathrm{M}_{\odot} yr^{-1}$) gives way to the occurrence of a He-convection zone despite the slow rotation. Another possible explanation could be the *accretion/diffusion* theory by Venn & Lambert (1990). The basic idea is that the star accretes metal-poor material from the Interstellar Medium (ISM) which can explain the under-abundances of almost all heavier elements. In this scenario, if a binary system passes through an interstellar cloud, both stars should display similar spectral features. However, as pointed out by Alacoria et al. (2022), there is little to no evidence for this scenario.

1.1.2. Photometric detection using Δa photometry

The classifications mentioned above purely correspond to spectroscopic detection. However, in case of the magnetic chemically peculiar (mCP) (mostly belonging to the CP2 category), it was observed, that the continuum of the spectrum dips around λ5200. One of the first

observations of this flux depression was made by Kodaira (1969) in the spectrum of HD 221568. Similar effects were found in many other mCP stars. An explanation for the flux depression is given by Khan & Shulyak (2007). They mention, while iron is the most important element in this phenomenon, there is also a contribution by other elements such as Si and Cr.
Maitzen (1976) used this feature to detect these stars via a photometric method, the so-called Δa photometry. For this, a three-filter system was defined:

- g_1 at $\lambda 5020$
- g_2 at $\lambda 5200$
- y as the Strömgren y filter

From that, one can define the peculiarity index as

$$a = g_2 - \frac{(g_1 + y)}{2} \tag{1.1}$$

and then compare it to the a-value of a normal star (a_0) of the same spectral type using the quantity Δa, defined as:

$$\Delta a = a - a_0(g_1 - y) \tag{1.2}$$

with the colour $(g_1 - y)$ correcting for temperature differences in the stars. This system is very potent in discovering mCP stars, since almost all of them exhibit positive Δa values (Paunzen et al. (2005). This method has also led to the discovery of mCP stars in the Large Magellanic Cloud (LMC) (Paunzen et al. (2006)).

1.1.3. Spectroscopic and photometric Variability

Some of the mCP stars show strong magnetic fields, the first one to be discovered that way was, as mentioned earlier, 78 Vir (HD 118022, Babcock (1947)). Those magnetic fields can reach field strengths of up to tens of kG (e.g. Bagnulo et al. (2003); Mathys (2017)). The origin of those strong magnetic fields is still controversial, a case for the magnetic field of the ISM to be frozen in the star can be made (See Appendix A for a short mathematical description) (Braithwaite & Spruit, 2004). However, we still lack the understanding of how such a magnetic field can be preserved on the upper main sequence, although Schleicher et al. (2023) suggested that the magnetic field could be sustained when the stellar core transforms from the convective to the radiative state during the pre-main sequence phase, where the lack of convection provides an environment where the magnetic field is not dissipated by the turbulent motions present in regions with convection.
On the other hand, we can readily observe the effects that the magnetic field has on the star. Stibbs (1950) was one of the first that observed photometric variability and the variability of the magnetic field in the star HD 125248. He proposed that this behaviour and also the variability of spectral lines as observed by e.g. Deutsch (1947) can be

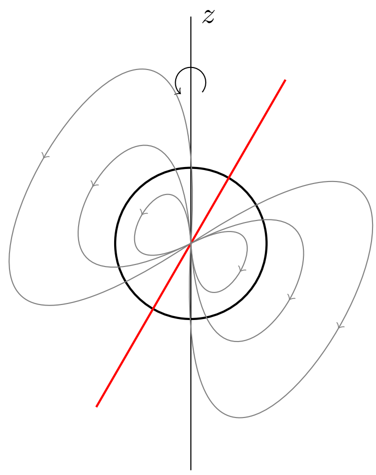

Figure 1.1.: Schematic model of the oblique rotator. The star (black circle) rotates around the z-axis, while the magnetic field axis is inclined (red). An approximation of the magnetic field lines is shown in gray.

explained with a model that has a magnetic field axis that is inclined with respect to the rotational axis of the star (Fig. 1.1). This is called the *Oblique Rotator* theory (Stibbs, 1950).

The photometric variability is classically seen as a so-called double wave (Fig. 3.7) that arises from chemical spots that form at the magnetic poles. Those inhomogeneities in chemical surface composition are a result of atomic diffusion processes (Michaud et al., 1981). This class of variable stars is commonly known as α^2 Canum Venaticorum (ACV) variables in both the General Catalog of Variable Stars (GCVS) (Samus' et al., 2017) and the Variable Star Index (VSX) (Watson et al., 2006). There are also analogues of the ACV variables on the hotter part of the upper main sequence, the so-called SX Arietis (SXARI) stars (Balona, 2022). Some mCP stars also show pulsational variability with periods between around 5 and 30 minutes. They are called rapidly oscillating Ap (roAp) stars and need to be confirmed using spectroscopy to distinguish them from the class of δ Scuti (DSCT) stars that have similar pulsation properties. Additionally, the roAp stars are cooler than classical DSCT stars and can be found in the region of γ Doradus (GDOR) stars when looking at an Hertzsprung-Russell diagram (HRD) (Balona et al., 2011).

1.2. Stellar associations

Stellar associations, a term coined Ambartsumian (1947), are very young (few tens of Myr) and very loose (stellar density $< 0.1 \mathrm{M}_{\odot} pc^{-3}$, Blaauw (1964); Wright et al. (2023)) stellar aggregates. Ambartsumian (1947) defined the sub-types OB (for associations with predominantly O and B type stars) and T (for associations with cooler T-Tauri starts).

van den Bergh (1966) introduced a third subclass, the R associations that are affiliated with reflection nebulae. Classically, they are named after the constellation they are in[2] and the sub-type (OB, T, R) and sometimes, if more than one association is present in the region of a constellation, they also get numbered (e.g. The Chamaeleon 1 and Chamaeleon 2 associations). A prime example of this naming convention would be the Per OB1 association.
Since those stellar aggregates are very young (up to a few tens of Myr, Wright et al. (2023)), they prove to be extremely well suited to investigate what traces of the recent Star Formation (SF) are left in the stars (Carraro, 2020). Due to that young age, they can contain open clusters as well as star forming regions inside their boundaries (Wright et al., 2023).

1.2.1. How do associations form?

Basically, two scenarios have been accepted to be responsible for the formation of associations (a more detailed description can be found in Carraro (2020)):

- The stars are formed where they are observed, since SF does not seem to have a preferred scale and happens on hierarchical structures from galactic to individual stars. So, over-densities in the ISM can happen everywhere and at any scale.
- Here, the stars are formed in clusters (Lada & Lada, 2003). Then, UV radiation and stellar winds blow away the remaining gas which leads to the cluster not being in virial equilibrium any more. This results in the aggregate becoming loose and disperse over time.

1.2.2. Detecting stellar associations

Detecting stellar associations has not always been a simple task. Due to the relatively low densities compared to open clusters ($\leq 0.1 M_{\odot} pc^{-3}$ (Blaauw, 1964)), they are hard to detect based on only the positions of the stars. The methods to find and define associations rely on combinations of different astrometric properties such as distances and proper motions combined with age estimations and spectroscopic measurements (e.g. Luhman (2007)). The last decades used the data from the HIgh Precision Parallax COllecting Satellite (*Hipparcos*) mission for this. However, since the advent of the *Gaia* mission (Gaia Collaboration et al., 2016) we deal with data of unprecedented quality and precision.
This set of astrometric data is then used in finding open clusters and associations and also allows us to accurately determine which of the suspected members are real confident members and which can be discarded. This is primarily done via clustering algorithms such as *Hierarchical Density-Based Spatial Clustering of Applications with Noise* (HDBSCAN) (McInnes et al., 2017), for example. Recent studies of detecting open clusters and

[2] As defined by the International Astronomical Union (IAU) (`https://www.iau.org/public/themes/constellations/`)

associations are, for example Cantat-Gaudin & Anders (2020); Kerr et al. (2021); Hunt & Reffert (2023).
Additionally, other methods are used for the determination of the members of clusters and associations. Those include, but are not limited to

- Unsupervised Photometric Membership Assignment in Stellar Clusters (UPMASK) (Krone-Martins & Moitinho, 2015)
- Significant Mode Analysis (SigMA) (Ratzenböck et al., 2023a,b)
- Gaussian Mixture Models (GMM) (Agarwal et al., 2021)

Cantat-Gaudin & Casamiquela (2024) list a few more examples and offer a discussion on the astrometric properties of open clusters and associations.

1.2.3. Ages of associations

Many phenomena in stellar evolution are strongly correlated with or dependent on the age of the star in question. However, determining the age of a group/cluster of stars, let alone one single star, is a non-trivial task and always dependent on the method used as well as the underling models and the assumptions made in the model. However, there are a few commonly used methods that generally produce reliable results.

Isochrones

Fitting an isochrone to the Colour-magnitude diagram (CMD) of a cluster is the most frequently used method for determining a clusters age. The advantage is that one can not only determine the age of the cluster but also make an estimate of distance, extinction values and metallicity. However, the method strongly depends on the underlying model used, as well as the observational data, and can vary significantly when comparing different values of those properties. Commonly used theoretical isochrones for this are the PAdova TRieste Stellar Evolution Code (PARSEC) isochrones (Bressan et al., 2012), the MIST isochrones (Dotter, 2016) and the values from the *Dartmouth Stellar Evolution Code* (Dotter et al., 2008).

Lithium Depletion Boundary (LDB)

Lithium is a relatively volatile element in the sense that it burns at relatively low temperatures compared to a stellar core. In the pp-chain, ^{6}Li is converted to ^{7}Be at temperatures of $\sim 1.3 \cdot 10^6$K (e.g. Burke et al. (2004)). This means, we can observe lithium only in the spectra of low-mass stars that have not (yet) reached those temperatures in their convective envelopes. Comparing the lithium abundance over a range of effective temperatures to models, one can determine the age of the cluster in question. The best chance of measuring the lithium abundance is measuring the λ6708-doublet in the red part of the spectra.
The equivalent width W_λ of a spectral line is defined via

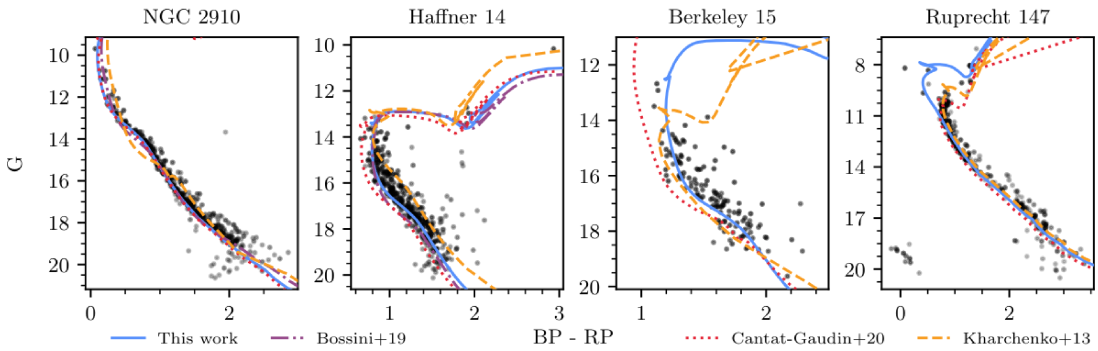

Figure 1.2.: Some open clusters with fitted isochrones and a comparison with literature. This is Fig. 7 in Hunt & Reffert (2023).

$$W_\lambda = \int \frac{F_c - F_s}{F_c} d\lambda \tag{1.3}$$

where F_c is the continuum level of the spectrum and F_s is the actuall flux of the spectrum. A recent example working with this method is Galindo-Guil et al. (2022).

Kinematic age

Under the assumption that all stars in a cluster or association formed more or less simultaneously and gradually disperse over time, we can in principle trace back their orbits to the point where they are the closest and thus revealing the age of the association. For this, one needs accurate measurements of the astrometric properties α, δ, $\mu_{\alpha_\star} = \mu_\alpha cos\delta$, μ_δ, v_{rad}. See e.g. Miret-Roig et al. (2020) for an application on the β Pictoris group.

1.3. Star formation and pre-main sequence evolution

In short, Star Formation (SF) happens like this:
We first start by looking at a MC that collapses under gravity. Then, a protostar is formed that gets its luminosity by the energy of accretion on its core. After some time, depending on its mass, the outer layers get blown away and we arrive at the so-called *birth-line* (e.g. Stahler (1983); Palla & Stahler (1990); Lada (2005)). In this stage we can observe emission lines (primarily hydrogen) in the spectra of the star and when looking at the Spectral Energy Distribution (SED), infrared excess is seen. Only after this stage, the hydrogen fusion starts in the star, meaning the protostar arrives on the Zero-Age main sequence (ZAMS). See Fig. 1.3 for an illustration of this process.

There are associations, open clusters and moving groups that are really young. The Chamaeleon I association, for example, is only about 2 Myr old (Luhman, 2007). Thinking about this, one can also look for CP stars that are still in their PMS phase. The stars that are located in the upper parts of the Hertzsprung-Russell diagram (HRD) and are

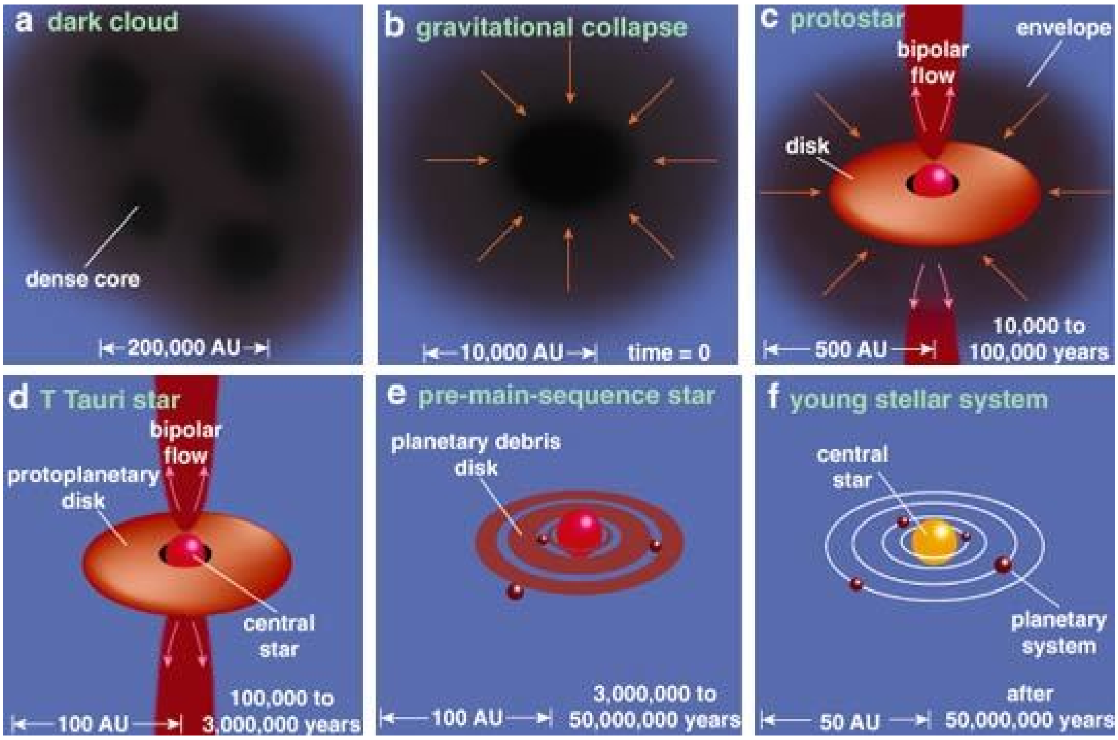

Figure 1.3.: Schematic view of the star formation process described in the text. Taken from Sahoo (2016)

still in their Pre-Main Sequence (PMS) phase are called *Herbig Be/Ae* stars. So those are the stars we need to look for when trying to find CP stars that are still in their PMS phase.
So far, not many PMS CP stars have are known. Netopil et al. (2014) analysed stars in the open cluster Stock 16 and found that one star seemed to be showing peculiarities commonly found in Am stars. Cariddi et al. (2018) found three PMS mCP candidates in Hogg 16, another open cluster. Recently Potravnov et al. (2023a,b) reported two CP stars, one being a He-weak (CP4) star and one an mCP star showing magnetic field strengths of up to 3.5kG. Lastly, Kueß et al. (2024) reported nine mCP stars that are also in their PMS evolution, with one candidate that has not been named in the literature before, strengthening an argument by Folsom et al. (2012) who suggested a link between Herbig Ae/Be stars and mCP stars.

2. Data

In this chapter, an overview of the used surveys and data, as well as the reduction and preparation of said data is described.

2.1. Used surveys

For this work, the combined data products of different surveys have been made use of. Those surveys are

- *Gaia* Data Release 3 (*Gaia* DR3)
- TESS Input Catalog (TIC)v8.2
- Data Release 9 from the *Large Sky Area Multi-Object Fiber Spectroscopic Telescope* (LAMOST)

2.1.1. *Gaia* Data Release 3 (*Gaia* DR3)

The *Gaia* mission (see Gaia Collaboration et al. (2016) for a detailed description) was launched in 2013 and scans the sky for astrometric (position and proper motions) measurements with unprecedented accuracy and also photometric measurements in three filters (Fig. 2.1). This rich dataset has resulted in a plethora of new discoveries, especially dealing with the structure of the milky way as well as discoveries stellar clusters and associations or moving groups (e.g. Meingast et al. (2019); Alves et al. (2020).
The latest data release (*Gaia* DR3) includes measurements in position, radial velocity, Gaia Blue Photometer (G_{BP}), Gaia Red Photometer (G_{RP}), Gaia G Photometer (G) and proper motions (μ_α, μ_δ) for 1,811,709,771 sources, with full astrometry for 1,467,744,818 sources (Gaia Collaboration et al., 2016, 2022). In this data release, we also have low resolution spectra covering the whole wavelength range from 300-1100nm observed by *Gaia* (De Angeli et al., 2023; Montegriffo et al., 2022). An example can be seen in Fig. 2.1. Those spectra, although no detailed analysis of the elements present can be done, are-well suited for the detection of mCP stars making use of (synthetic) Δa-photometry as demonstrated by Paunzen & Prišegen (2022) and also this work (see chapter 3). Additionally, they can be used to perform synthetic photometry with a precision that is similar to the values obtained by modern ground-based photometry (Gaia Collaboration et al., 2023).

[1]Downloaded here: `https://www.cosmos.esa.int/web/gaia/edr3-passbands`

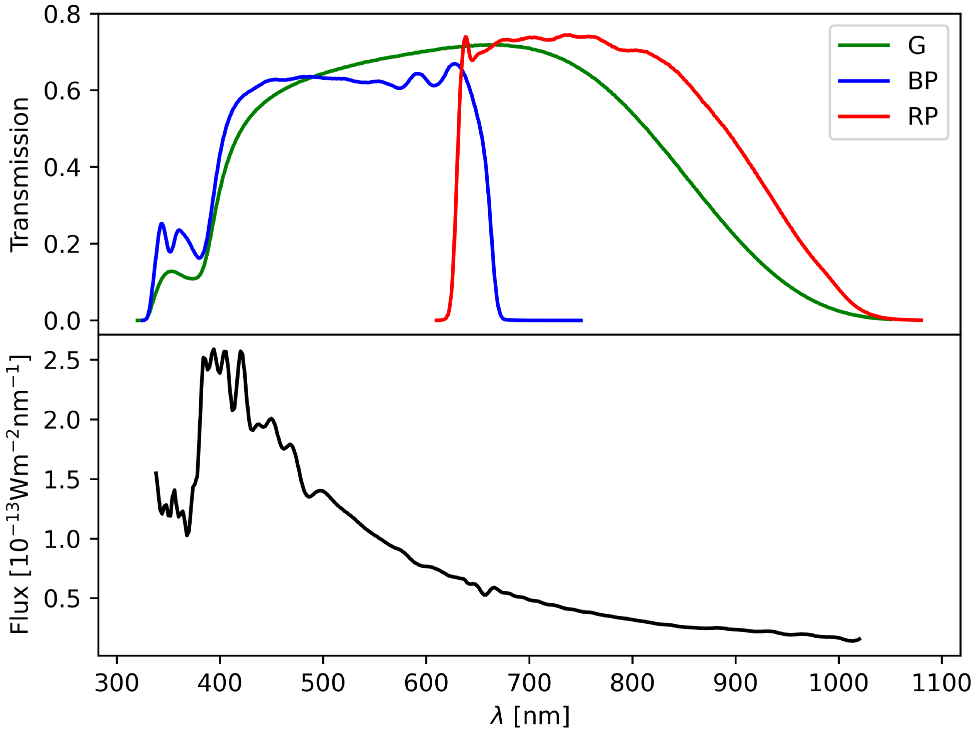

Figure 2.1.: *Upper*: *Gaia* DR3 passbands published by the *Gaia* consortium [1]. The passbands were defined for *Gaia* Early Data Release 3 (*Gaia EDR3*). *Lower*: Example BP/RP spectrum of *Gaia* DR3 6126469139186679808, An A-type star as can be seen by the Balmer jump in the violet part of the spectrum and the rest if the continuum.

2.1.2. *Transiting Exoplanet Survey Telescope* (TESS)

TESS is a spacecraft started in 2018. It consists of four small ($\sim$ 10cm) apertures, each with a Field of View (FOV) of $24° \times 24°$ each, resulting in a total FOV of $96° \times 24°$ (Ricker et al., 2015). Every month it observes this portion of the sky as so-called *sectors*. They overlap in the polar regions which are then called the Continuous Viewing Zone (CVZ). The sectors are observed in cadences of two seconds that are downloaded in cadences of 20 seconds for few pre-selected targets that are studies using asteroseismology, two minutes (Short Cadence (SC)) for objects of interest in terms of hunting for planets and finally in 30-minute cadences (Long Cadence (LC)) for all observed pixels. The data are stored in the so-called Full-Frame Image (FFI). Those are created every 30 minutes by the spacecraft and can be accessed e.g. through the Mikulski Archive for Space Telescopes

(MAST)[2]. The primary scientific goal of the spacecraft is to look for exoplanets using the transit method. However, since it not only observed plant hosting stars, we also can make use of the light curves of variable stars. This thesis makes use of the TESS Input Catalog (TIC) v8.2 (Paegert et al., 2021).

2.1.3. *Large Sky Area Multi-Object Fiber Spectroscopic Telescope* (LAMOST)

LAMOST, also known as *Guo Shoujing Telescope* is a survey telescope located at the Xinglong Station northeast of Bejing, China (Cui et al., 2012; Zhao et al., 2012). Using a focal plane designed for Multi-Object Spectroscopy (MOS), it can observe roughly 4000 objects at the same time, making it a very useful tool for large spectroscopic surveys. One of the main goals is to give an insight in the chemical history of our galaxy. With a spectral resolution of $R \sim 1000 - 1500$, its data products (spectra in the wavelength range from $3700 - 9000$Å) are well-suited for spectral classification and have already lead to the discovery of numerous CP stars (e.g. Hümmerich et al. (2020); Shang et al. (2022)). An example spectrum can be seen in Fig.2.2. However, the telescope has one disadvantage. Due to its limited movement, it can only observe the sky between $\sim -10°$ and $+90°$, so many interesting parts of the galactic plane can not be observed by this instrument. This thesis makes use of DR8[3] the second to last public data release at the time of writing.

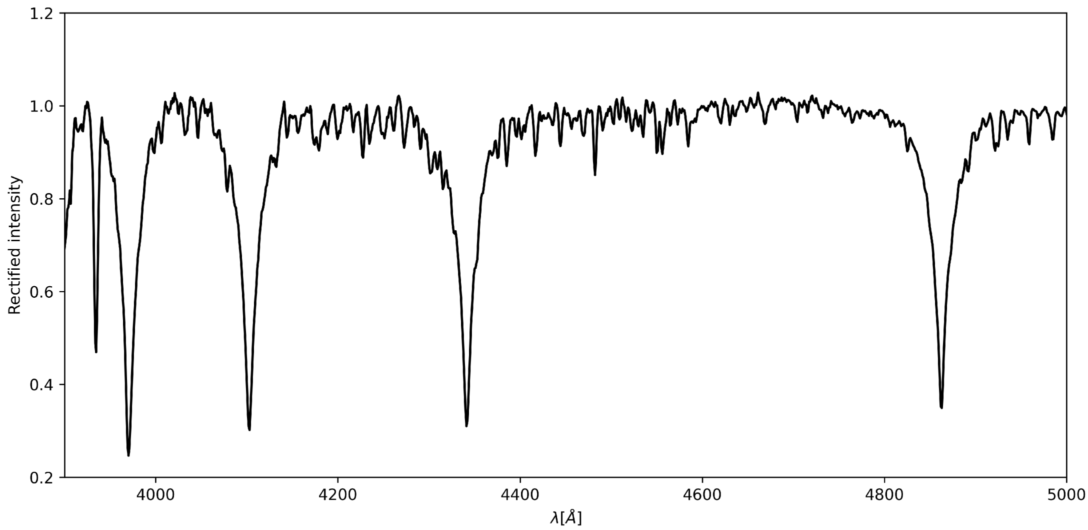

Figure 2.2.: Blue-violet part of an example spectrum from LAMOST

[2] https://archive.stsci.edu/
[3] http://www.lamost.org/dr8/

2.2. List of Associations

For the purpose of generating a list of young CP stars, it is necessary to get a list of known associations. Here, three recent publications were used:

1. The *Stars with Photometrically Young Gaia Luminosities Around the Solar System* (SPYGLASS) (Kerr et al., 2021). This catalog includes 27 young ($\lesssim$ 100 Myr) regions in a volume contained by a ~300pc radius.

2. The extensive catalogue of stellar associations and open clusters from Hunt & Reffert (2023). The list includes 228 moving groups, 134 globular clusters and 6,805 open clusters, many of them newly detected.

3. For the Sco-Cen region the data from Ratzenböck et al. (2023a,b) was taken. They provide a list of 37 sub-clusters, all with accurate age estimations.

2.3. Data reduction and preparation

2.3.1. Used quality criteria

Astrometry

In order to get good astrometric and photometric quality for the sources described in Kerr et al. (2021) and Hunt & Reffert (2023), it was necessary to use certain quality criteria and cuts on the dataset. The good astrometry done by *Gaia* still has some instrumental and systematic effects. One of the quality criteria most widely used is the so-called *re-normalised unit weight error* (RUWE). While the unit-weight-error provides a good measure of goodness-of-fit, it is highly dependent on colour and magnitude of a given stellar source, so re-normalisation was needed (Lindegren, 2018). For a source with m parameters solved and N good (not considering outliers) observations, it is defined as:

$$RUWE = \frac{1}{f(G, G_{BP} - GRP)} \sqrt{\frac{\chi^2}{N - m}} \tag{2.1}$$

Where $f(G, G_{BP} - GRP)$ is a function of G and the G_{BP}-G_{RP} colour and $1/f(G, G_{BP} - GRP)$ is the normalisation factor. Additionally, χ^2 is the χ^2 statistics of the astrometric measurements R:

$$\chi^2 = \sum_k \left(\frac{R_k}{\sigma_k} \right)^2 \tag{2.2}$$

The ideal value of RUWE for single star sources is 1, all sources with $RUWE > 1.4$ can be considered either binaries or sources with poor astrometric measurements (Lindegren, 2018).
The second astrometric selection was made to remove sources that had a "bad" parallax measurement. In this case, a similar approach to Kerr et al. (2021) was taken. This paper

uses a value of $\varpi/\sigma_\varpi > 8$, the present thesis takes a slightly more cautious approach and uses $\varpi/\sigma_\varpi > 10$.

Photometry

According to Riello et al. (2021), the photometry of *Gaia* DR3 has systematic errors, especially for less bright sources. They recommend to exclude all sources with G_{BP}< 20.3 mag, because there is a systematic brightening in this magnitude region. Additionally, a filter on the flux excess factor C is imposed. For this, one has to calculate the corrected flux excess factor C^*:

$$C^* = C - f(G_{BP} - G_{RP}) \tag{2.3}$$

where $f(G_{BP} - G_{RP})$ is a polynomial of the form

$$f(x) = \sum a_i x^i \tag{2.4}$$

where the coefficients a_i are defined as follows:

a_i	$x < 0.5$	$0.5 \leq x < 4.0$	$x \geq 4.0$
a_0	+1.154360	+1.162004	+1.057572
a_1	+0.033772	+0.011464	+0.140537
a_2	+0.032277	+0.049255	-
a_3	-	-0.005879	-

Table 2.1.: Coefficients for the polynomial in Eq. 2.4, taken from Riello et al. (2021)

and C is defined as the ratio between the total fluxes in G_{BP} and G_{RP} combined and the total flux in G:

$$C = \frac{F_{BP} + F_{RP}}{F_G} \tag{2.5}$$

2.3.2. Astrometric transformations

The astrometric corrections and transformations follow the pre-processing done by Kerr et al. (2021).

Galactic to spherical coordinates

For the planned clustering, positions of the stars, consisting of galactic longitude l, galactic latitude b and the distance R from the sun were transformed into cartesian 3D spherical coordinates via the transformation

$$\begin{aligned} X &= R \cos l \cos b \\ Y &= R \sin l \cos b \\ Z &= R \sin b \end{aligned} \tag{2.6}$$

X, Y and Z are then the 3D distances from the sun in the three spatial dimensions. The actual distance to the sun is then defined as

$$R = \sqrt{X^2 + y^2 + z^2} \tag{2.7}$$

Galactic proper motions to transversal velocities

The commonly used coordinate system at our time is the so-called International Celestial Reference System (ICRS). It's center is the barycenter of our solar system with positions in it defined in relation to several distant quasars that are assumed to be stationary with respect to our solar system.
After the conversion to spherical coordinates, the proper motions in the equatorial (ICRS) system ($\mu_{\alpha\star} = \mu_\alpha \cdot \cos\delta$, μ_δ) given in the *Gaia* data needed to be converted to the galactic frame as well. Here, the transformations suggested by the *Gaia* consortium[4] were used. The proper motions $\mu_{\alpha\star}$, μ_δ are transformed to the galactic frame using auxiliary column matrices:

$$\vec{p}_{ICRS} = \begin{pmatrix} -\sin\alpha \\ \cos\alpha \\ 0 \end{pmatrix}, \qquad \vec{q}_{ICRS} = \begin{pmatrix} -\cos\alpha\sin\delta \\ -\sin\alpha\sin\delta \\ \cos\delta \end{pmatrix} \tag{2.8}$$

and

$$\vec{p}_{Gal} = \begin{pmatrix} -\sin l \\ \cos l \\ 0 \end{pmatrix}, \qquad \vec{q}_{Gal} = \begin{pmatrix} -\cos l\sin b \\ -\sin l\sin b \\ \cos b \end{pmatrix} \tag{2.9}$$

With those, the proper motion vectors can be written as:

$$\vec{\mu}_{ICRS} = \vec{p}_{ICRS}\mu_{\alpha\star} + \vec{q}_{ICRS}\mu_\delta \tag{2.10}$$

and in the galactic frame:

$$\vec{\mu}_{Gal} = \vec{p}_{Gal}\mu_{l\star} + \vec{q}_{Gal}\mu_b \tag{2.11}$$

The two can be transformed into each other, using the matrix A'_G:

$$A'_G = \begin{pmatrix} -0.0548755604162154 & -0.8734370902348850 & -0.4838350155487132 \\ +0.4941094278755837 & -0.4448296299600112 & +0.7469822444972189 \\ -0.8676661490190047 & -0.1980763734312015 & +0.4559837761750669 \end{pmatrix}$$

[4] https://gea.esac.esa.int/archive/documentation/GDR3/Data_processing/chap_cu3ast/sec_cu3ast_intro/ssec_cu3ast_intro_tansforms.html

Finally, the proper motions in the galactic frame can be calculated via

$$\vec{\mu}_{Gal} = A'_G \vec{\mu}_{ICRS} \tag{2.12}$$

and then

$$\mu_{l_\star} = \vec{p}^{\,T}_{Gal} \vec{\mu}_{Gal}, \qquad \mu_b = \vec{q}^{\,T}_{Gal} \vec{\mu}_{Gal} \tag{2.13}$$

3. Methods

The following pages give an overview of the methodology used in this work and describe the software and techniques used for this purpose.

3.1. Membership of Open Clusters and Associations

3.1.1. HDBSCAN

Since the downloaded sets of stars contained members and non-members of the clusters and associations, it was necessary to determine which stars are likely to belong to the aggregations. For this purpose, multiple methods exist and can be utilised. For example, one can look at the stars and see which ones are moving together (see e.g. Meingast & Alves (2019); Meingast et al. (2019)). Other authors relied on photometry combined with spectroscopic measures (e.g. Luhman (2007) for Cha I).
A relatively recent method is the so called *Hierarchical Density-Based Spatial Clustering of Applications with Noise* (HDBSCAN), Campello et al. (2013)[1]), an algorithm based on Density-Based Spatial Clustering of Applications with Noise (DBSCAN) (Ester et al., 1996).
It works by first calculating a core distance $core_k(x)$ to the k-nearest neighbours for each data point x. After that a new distance metric is defined, the *mutual reachability distance* using the original (e.g. euclidean) distance $d(a, b)$ between points a and b:

$$d_{mreach-k}(a, b) = max\{core_k(a), core_k(b), d(a, b)\} \tag{3.1}$$

Next, those distances are used to generate a minimum spanning tree using Prim's algorithm (Prim, 1957). From those spanning trees, a cluster hierarchy is built and finally the clusters are extracted. Depending on which hyper-parameters one chooses, clusters of different sizes and densities can be extracted.
Concerning the hyper-parameters, the `python` implementation of HDBSCAN (McInnes et al., 2017) allows for a few options that have a more or less strong impact on the result of the clustering:

- `min_cluster_size`
  This parameter describes the minimum number of points that a cluster should contain. Larger values result in clusters getting merged together, while lower values give more smaller clusters.

[1] `https://hdbscan.readthedocs.io/en/latest/index.html`

- `min_samples`
  Basically, it is a measure of how dense the resulting clusters should be. Setting it to a large value will determine only the densest parts of the data as clusters and leave all other points as "noise".

- `cluster_selection_epsilon`
  The choice of this hyper-parameter influences the distance between two clusters that should be separated. A higher value merges more clusters into one, a lower value gives a more detailed clustering with maybe more individually split up groups.

- `alpha`
  This one is a stricter method of doing the same thing as `min_samples`. However, the documentation advises not to touch it, if one has not tried more combinations of the other parameters. It is set to 1 by default and should not be changed too much.

- `cluster_selection_method`
  Here, a selection of how fine or detailed the clustering should be applied is selected. HDBSCAN allows for two methods:
  - `eom`
    This stands for "excess of mass" and does exactly that. It searches for the over-densities in the n-dimensional parameter space and finds out where, according to the other parameters, the clusters are located. The method tends to favour less and larger clusters.
  - `leaf`
    With this method, one can recover smaller and finer granulated clusters in the dataset.

- `allow_single_cluster`
  Similar to `min_cluster_size`, this parameter is self-explaining. When set to `True`, HDBSCAN recovers only one cluster. `False` results in more clusters.

- `metric`
  Depending on which metric one chooses, the algorithm calculates the distance between the points in the n-dimensional data set in different ways. A few commonly used choices are:
  - Euclidean distance: $d(a,b) = |a-b|$
  - Manhattan distance: $d(a,b) = \sum_i |a_i - b_i|$
  - Minkowski distance: $d(a,b) = \left(\sum_i |a_i - b_i|^p\right)^{1/p}$
    This is a generalisation of the previous two. By choosing $p=1$, one gets the Manhattan distance and by setting $p=2$, the result is the Euclidean distance. This is analogous to the p-norm in mathematics.

– Mahalanobis distance: $d(a, b) = \sqrt{(a_i - b_i)^T S^{-1}(a_i - b_i)}$
The matrix S is the covariance matrix of the measurements.

3.1.2. Shortcomings of HDBSCAN

Compared to other clustering algorithms found in the literature, HDBSCAN seems to be the one that works best (Hunt & Reffert, 2021). However, it is not perfect. Hunt & Reffert (2021, 2023) describe in detail, the flaws that HDBSCAN has. In short, it can be overconfident in finding clusters, resulting in a large number of false positives. This however, is more a problem when dealing with the all-sky approach used by Kerr et al. (2021); Hunt & Reffert (2021) and Hunt & Reffert (2023) because of the large number and varying density of the stars in the volume those authors probed. In this thesis, it should not be too big a problem, since it only deals with relatively small volumes and thus should only recover the "real" clusters and associations. However, one still needs to make somewhat of a quality assessment and thus the membership probabilities calculated by the algorithm was taken into account in the further analysis, only using stars with a membership probability above a certain threshold should be used as "true" members.

3.1.3. Astrometry for clustering

For this work, the algorithm was used on an input data set consisting of five astrometric parameters following the method from Kerr et al. (2021):

- The 3D cartesian distances X, Y, Z (see Eqn. 2.6)

- The transversal velocities $v_{T_{l\star}}$, v_{T_b} in the galactic frame of the stars. Those are calculated from the proper motions simply by multiplying them with the distance:

$$\begin{aligned} v_{T_{l\star}} &= 4.74 \mu_{l_\star} R \\ v_{T_b} &= 4.74 \mu_b R \end{aligned} \tag{3.2}$$

The factor 4.74 in equation 3.2 ensures that the final values are in the correct units, i.e. km/s[2]. One could also use the 3D velocities U, V, W, corresponding to the 3D cartesian distances X, Y, Z. However, we do not have radial velocities for every star, so to not leave out too many sources I stuck with the galactic transversal velocities.

[2]The factor comes from a simple conversion:

$$\frac{(arcsec\, yr^{-1})(pc)}{km/s} = \frac{(4.84816 \cdot 10^{-6} rad)(3.1563 \cdot 10^{7} s)^{-1}(3.086 \cdot 10^{13} km)}{km/s} \approx 4.74$$

3.1.4. Clustering

Kerr et al. (2021)

For the clustering on the input sample generated from the list of Kerr et al. (2021), a "manual" grid search was performed. This is due to the fact that the downloaded sources for each cluster and association are stored in separate files, so the algorithm had to loop over multiple datasets containing different numbers of sources and densities thereof. Obviously, one single choice of the hyper-parameters does not give good results for all aggregates, so a parameter grid to find the best combination has to be used.
The parameters tried are:[3]

```
param_grid = {
    'min_cluster_size': [5, 10, 15, 20, 25, 30, 35, 40, 45, 50],
    'min_samples': [3, 5, 10, 20, 30, 40],
    'cluster_selection_method': ['eom', 'leaf'],
    'metric': ['euclidean', 'manhattan'],
    'algorithm': ['best']}
```

The optimal hyper-parameters for each dataset were scored using a silhouette score. Using the average distance $a(i)$ of the i-th data point in the cluster to each other member and the smallest average distance between the i-th data point of the cluster to the members of other clusters $b(i)$, it is defined as

$$s(i) = \frac{b(i) - a(i)}{max\{a(i), b(i)\}} \quad \text{where} \quad s(i) \in [-1, 1] \tag{3.3}$$

The higher, i.e. closer to 1, $s(i)$ is, the better is the evaluation. For clusters containing only one single data point, the value is set to zero.
The determination of the "correct" hyper-parameters was performed on a randomly determined subset (30%) of the sources in each file. The subsequent clustering on the cleaned dataset (see chapter 2) was done via:

```
# Create a data frame with the positions and tangential velocities of the
    star
X = {"x": data["x_gal"], # X position derived from galactic coordinates
     "y": data["y_gal"], # Y position derived from galactic coordinates
     "z": data["z_gal"], # Z position derived from galactic coordinates
     "v_t_l": data["v_t_l"], # transversal velocity along galactic
    longitude
     "v_t_b": data["v_t_b"]} # transversal velocity along galactic
    latitude

X = pd.DataFrame(X)
```

[3]Note that there is no real "true" answer when it comes to the parameters used in a clustering process. The parameter grid here has been determined by trying different combinations and narrowing down the parameters and their possible values to be used.

```

# Initiate clusterer with the best parameters: best_params
clusterer_final = hdbscan.HDBSCAN(
    min_cluster_size=best_params['min_cluster_size'],
    min_samples=best_params['min_samples'],
    cluster_selection_method = best_params['cluster_selection_method'],
    metric=best_params['metric'],
    algorithm=best_params['algorithm'])

# cluster the data
clusterer_final.fit(X)
```

An example of the results plotted can be seen in Fig. 3.1.
In total, the parameters of 171,137 stars in the regions of those aggregates were put into the clustering. 19,473 ($\sim 11.4\%$) were determined to be members of associations with a membership probability $p \geq 0.5$. Of those, the stars that belong to the white dwarf sequence have been removed using a brightness cut. This left 19,264 ($\sim 11.3\%$ of the downloaded sources) sources in the list.

Hunt & Reffert (2023)

The stars were downloaded in a similar fashion as the ones from the list of Kerr et al. (2021). However, before getting the cluster parameters for the ADQL query, the list was stripped from the globular clusters and a 5σ-cut was made on the astrometric S/N (see Hunt & Reffert (2023) for details) in the catalogue data to remove clusters that have low significance and thus might not be real. This left a list of 5,119 aggregates to be downloaded and analysed. A few differences were made in the quality cuts, lowering the parameters `visibility_periods_used` and ϖ/σ_{ϖ} both to 5 to raise the probability of fainter and more distant sources to be clustered. Otherwise the method stayed the same as above.

3.1.5. Problems with the clustering

A probable difficulty with the clustering problem is - additionally to the ones mentioned above - that HDBSCAN tends to favour the smaller choices for `min_cluster_size` and `min_samples`. Overall, the clusters still get recovered as intended, however for larger or less dense groups, it more likely gets split up into more clusters than are really present, even with setting the `method` parameter to `eom` instead of `leaf`. This likely is a result of how the algorithm works combined with the distribution of the astrometric data. However, this should not be too big a problem when keeping in mind that only small parts of the sky were searched and thus it is unlikely to have more than two or three (real) sub-clusters for most of the target groups in this study.

Another factor that has to be kept in mind is the reliability of the clusters. In general, the closer associations are more likely to have correct membership probabilities, simply due to the fact that the quality of data tends to be higher for nearby objects. However, compared to previous astrometric datasets, the data from *Gaia* is still exceptional at higher distances, suggesting that the method used in this work is not too bad.

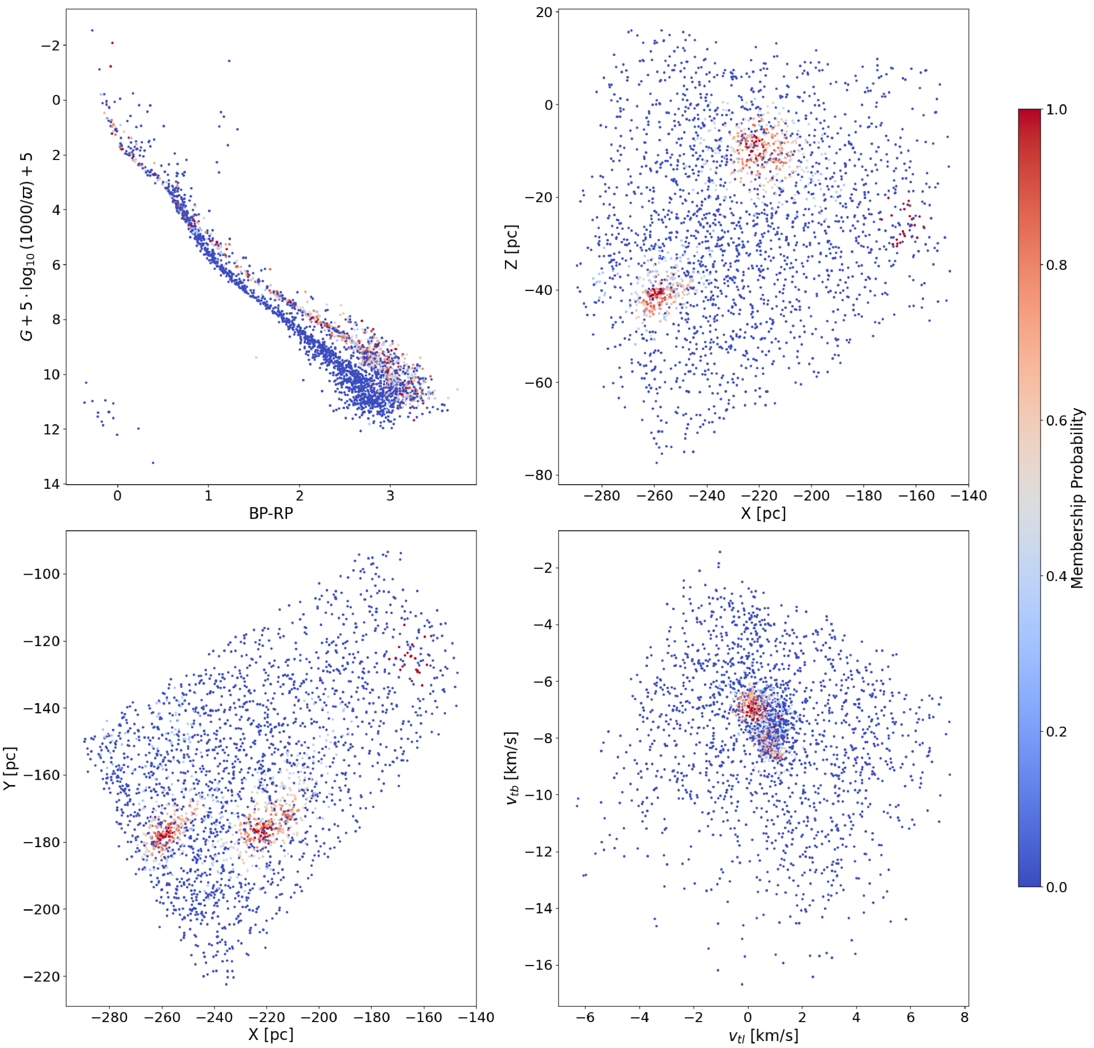

Figure 3.1.: Example for the result of clustering with HDBSCAN on the Monocerotis south-west association (called as such by Kerr et al. (2021)). *Upper left:* Colour-absolute magnitude ($G + 5 \cdot \log_{10}(1000/\varpi[\text{mas}]) + 5$) diagram. *Upper right:* X-Z plane of the positions of the sources. *Lower left:* X-Y plane of the position of the sources. *Lower right:* distribution of the transversal velocities ($v_{t_{l\star}}$, v_{t_b}). The stars are colour coded by membership probability.

3.2. Extinction

The resulting stars were matched to the StarHorse2021 catalogue prepared by Anders et al. (2022) to get extinction corrected sources. This catalogue, among extinction corrected and de-reddened photometry, also presents astrophysical parameters such as $T_{\rm eff}$, $\log g$, $M/{\rm M}_\odot$, A_V (line-of-sight extinction at $\lambda = 5420$Å), metallicity and distances as well as XYZ-positions in reference to the galactic centre. The extinction values have been calculated using the measurements of these datasets and surveys:

- *Gaia* EDR3 (Gaia Collaboration et al., 2016, 2021)
- 2MASS (Skrutskie et al., 2006)
- *Panoramic Survey Telescope and Rapid Response System* (Pan-STARRS1) (Chambers et al., 2016)
- *Wide-field Infrared Survey Explorer All Sky release* (AllWISE) (Cutri et al., 2013)

Due to the fact that Ratzenböck et al. (2023a,b) already provided well-clustered data and ages for 37 sub-regions in the Sco-Cen region, this part was left out from the clustering done in this work and were taken as they are. Combining this with the 430,230 stars resulting in the stars from Hunt & Reffert (2023), the total amount of stars considered to be members of associations resulted in 462,597 stellar sources that were matched to the StarHorse2 catalogue using the *Gaia* DR3 IDs. List included a total of 333,239 stars from the earlier selection. To select potential peculiar stars, a temperature cut was used, only leaving the stars with an effective temperature of $T_{\rm eff} \geq 6500$K or a spectral type earlier than about F5. This temperature cut left a final target list of 105,270 stars in that temperature range. See Fig.3.2 for a CMD of this selection.

3.3. Δa photometry

3.3.1. Downloading the *Gaia* BP/RP spectra

The source IDs of the determined member stars were used to get the *Gaia* BP/RP spectra. This can easily be done via a python script utilising an Astronomical Data Query Language (ADQL) routine (see Appendix A in De Angeli et al. (2023) for an example query). This then downloads the coefficients of the continuous representation for each available spectrum. The calibration of the spectra is then done with GaiaXPy[4], a custom python package provided by Montegriffo et al. (2022) that lets the user choose a wavelength grid to sample the spectral data. Basically, it takes the coefficients downloaded for a spectrum and applies them to a complicated set of base functions which then results in the final, absolute flux calibrated spectrum. A total of 64,005 spectra were downloaded and calibrated via this process.

[4] https://gaia-dpci.github.io/GaiaXPy-website/

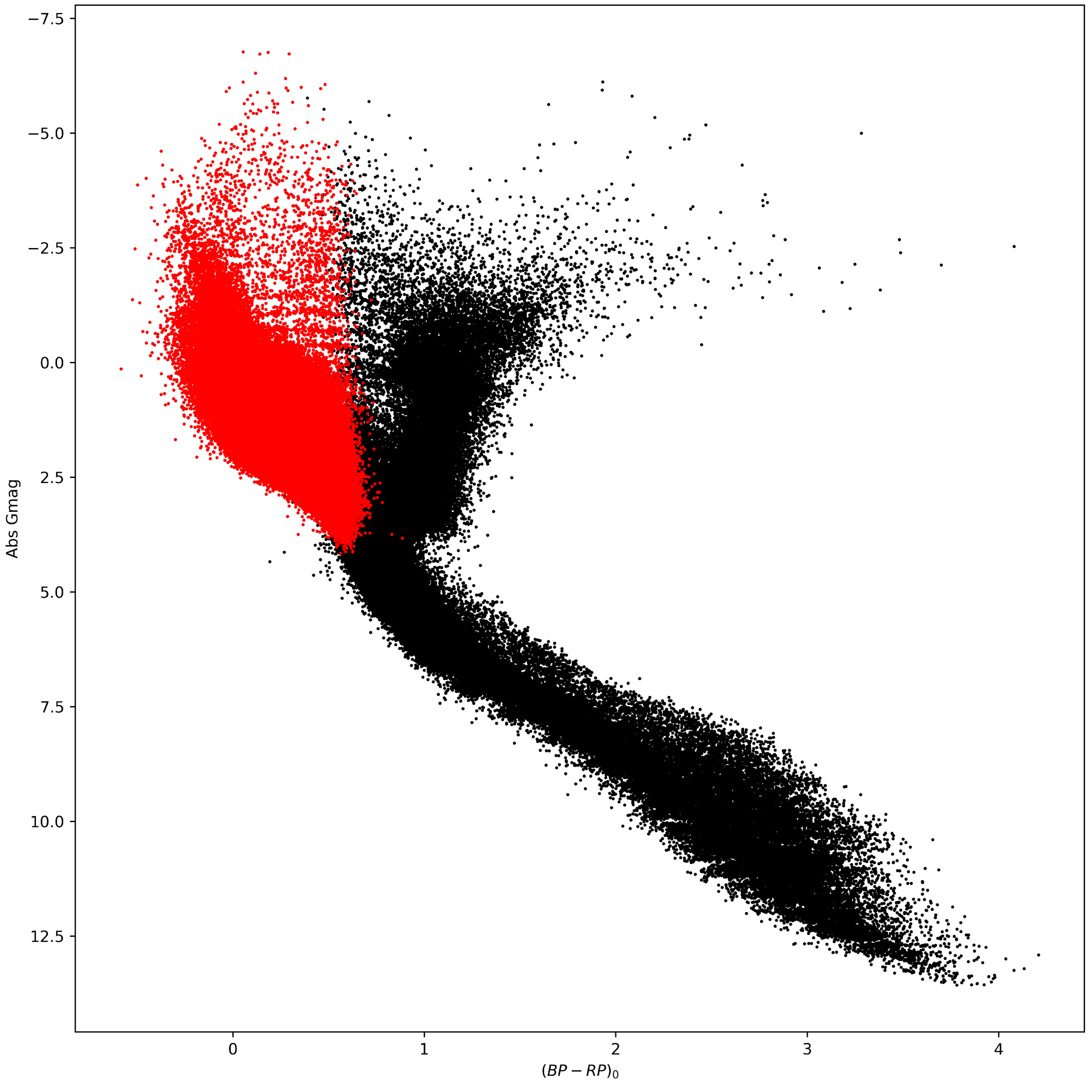

Figure 3.2.: Colour-absolute magnitude diagram of the stars that had a match in the `StarHorse2021` catalogue. The red stars are the ones selected with $T_{eff} \geq$ 6500K.

3.3.2. Signal-to-Noise Ratio

De Angeli et al. (2023) describe a quick calculation for estimating the S/N of the *Gaia* BP/RP spectra. For each of the two photometers (blue and red), the S/N can be calculated from the respective vector of coefficients and their errors by dividing the L_2 (euclidean) norm of the vector of coefficients by the L_2 norm of the vector of errors:

$$\text{SNR} = \frac{\|\texttt{bp/rp\_coefficients}\|_2}{\|\texttt{bp/rp\_coefficient\_errors}\|_2} \tag{3.4}$$

After calculating these values, I took the mean between the S/N of the red photometer and blue photometer as the final S/N of the spectrum:

$$SNR_{final} = \frac{1}{2}(SNR_{BP} + SNR_{RP}) \tag{3.5}$$

All spectra with values greater than $SNR_{final} = 100$ were considered for the subsequent analysis.

3.3.3. Normalisation and truncation

In order to get the synthetic magnitudes needed for Δa-photometry, the same method as in Paunzen & Prišegen (2022) was applied to the Gaia BP/RP spectra.
First, the spectra, originally absolute flux calibrated (in $Wm^{-2}nm^{-1}$) were normalised to the flux at $\lambda = 4020$Å and truncated to the wavelength region between 4800 and 5800Å.
Next, a quality assessment was done, removing all spectra of poor quality, leaving those with an S/N≥100. This left 26,814 stars in the sample.
After that, a polynomial interpolation was used to get the spectra to a "resolution" of 1Å.

3.3.4. Filters used

The synthetic photometry was done using three filters first defined by Maitzen & Seggewiss (1980):

- g_1 with a central wavelength at 5019.5Å
- g_2 with a central wavelength at 5211Å
- y as the Strömgren y-band (Strömgren, 1956; Crawford, 1958; Strömgren, 1966) with a central wavelength at 5463.5Å

A study performed by Stigler et al. (2014) has found the filter curves in Fig. 3.3 to be the most effective ones when it comes to the photometric detection of mCP stars.

3.3.5. Synthetic photometry

In the AB system (defined by Oke & Gunn (1983)), a magnitude in a filter with response curve $f(\lambda)$ would be calculated via (Bessell & Murphy, 2012):

$$m_f = -2.5 log \frac{\int f(\lambda)s(\lambda)\lambda d\lambda}{\int f(\lambda)(c/\lambda)d\lambda} - 56.10 \tag{3.6}$$

Where $f(\lambda)$ describes the transmission function[5] of the used filter, $s(\lambda)$ is the spectrum of the observed object and the constant at the end is the magnitude zero-point.

[5] Also called "response function"

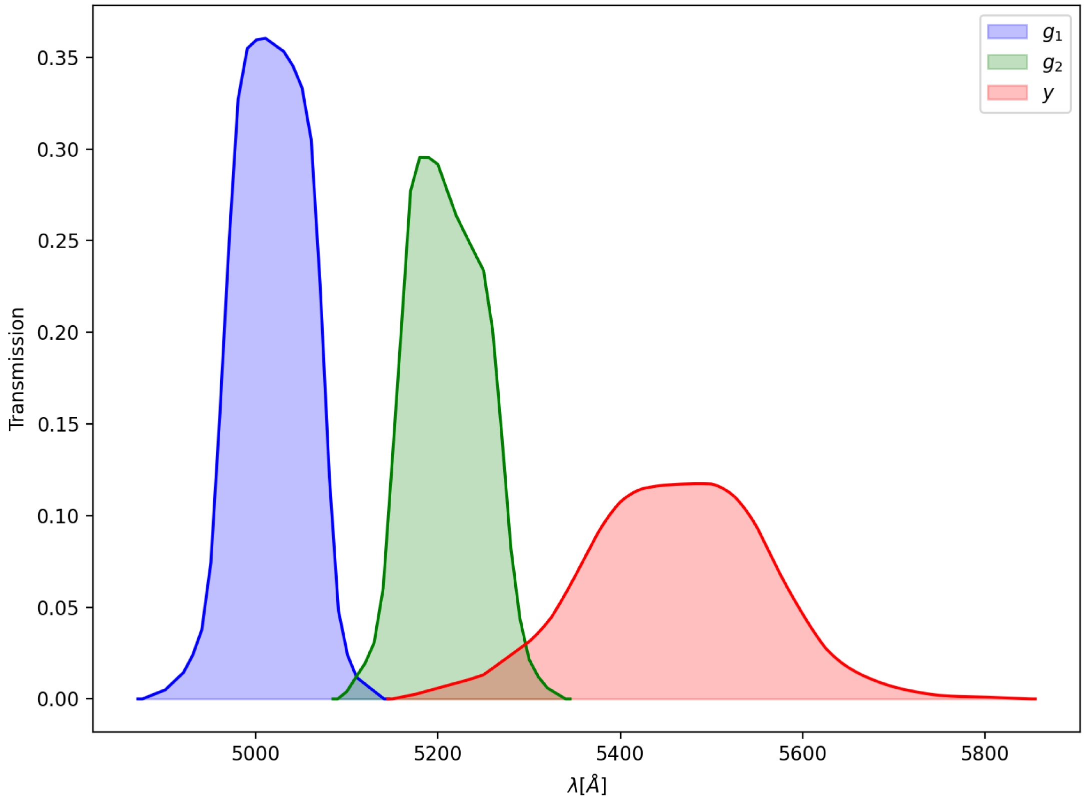

Figure 3.3.: The filter curves used for calculating the synthetic magnitudes.

This work uses a more numeric method of calculating the magnitudes by simply multiplying the filter curves with the spectra and summing up the results of the individual points:

$$m_f = \sum_i f(\lambda_i)s(\lambda_i) \tag{3.7}$$

Since the interest lies only in synthetic values and their differences (colour), their zero point can be neglected. Of course, if needed, the actual magnitudes can be calculated from the values obtained by this method. For the purpose of detecting the flux depression in the spectra, this is not necessary and one can be satisfied with the instrumental magnitudes resulting from Eq. 3.7

3.3.6. Finding the normality line

After calculating the magnitudes using Eq. 3.7, one can compute the a-index as follows:

$$a = g_2 - \frac{(g1 + y)}{2} \tag{3.8}$$

With this, it is still necessary to find the normality line a_0 that defines the apparent normal stars. This was done using a Bayesian linear regression model from the `python` module `PyMC` (Abril-Pla et al., 2023)[6]. This finds a best fit using Bayes theorem

$$P(\hat{\theta}|\hat{X},\hat{y}) = \frac{P(\hat{y}|\hat{X},\hat{\theta})P(\hat{\theta})}{P(\hat{y}|\hat{X})} \tag{3.9}$$

with the input vector $\hat{X}$ as our colour $(g_1 - y)$ measurements from above and $\hat{y}$ our a-values.
In short, a parameter vector $\hat{\theta}$ is drawn from a normal distribution $\hat{\theta} \sim \mathcal{N}(\mu_{\hat{\theta}}, \Sigma_{\hat{\theta}})$ via a Monte-Carlo process and finally the fit parameter vector $\hat{\theta}$ with the highest probability is chosen. This process resulted in the normality line.

$$a_0 = 0.454(3)(g_1 - y) - 2.815(29) \tag{3.10}$$

And then, the desired peculiarity index (the euclidean distance from the line) can be calculated:

$$\Delta a = a - a_0 \tag{3.11}$$

Per definition, stars that are on the normality line a_0 have a peculiarity index of $\Delta a = 0$. Stars that lie more than three standard deviations (≈ 1.298) above the normality line are considered to be mCP candidates. See Fig. 3.4 for the resulting diagrams. Note that there are also stars below the "normality region" defined by the grey area. These stars show emission in the probed part of their spectra. Those objects are candidate λ Böotis stars (Paunzen et al., 2005).

3.4. Spectral classification

Detecting or confirming CP stars is best done via spectroscopy. To get spectra of the sources in the sample, the list was matched to Data Release 9 of LAMOST. Out of the 105,270 sources in the final target list, 4,134 had a spectrum in this database. Only spectra with a Signal-to-Noise Ratio (S/N) greater than 50 in the g-band were considered for spectral classification which left 1440 stellar spectra to be classified.

3.4.1. MKCLASS

MKCLASS[7] (Gray & Corbally, 2014) is a software used to classify stellar spectra according to the MK system (Morgan et al., 1943). Multiple libraries of stellar spectra are available:

- `libr18`
  This library consists of stars of spectral types O9-K3 whose spectra have been rectified and have a resolution of 1.8Å

[6] `https://www.pymc.io/welcome.html`
[7] `http://www.appstate.edu/~grayro/mkclass/`

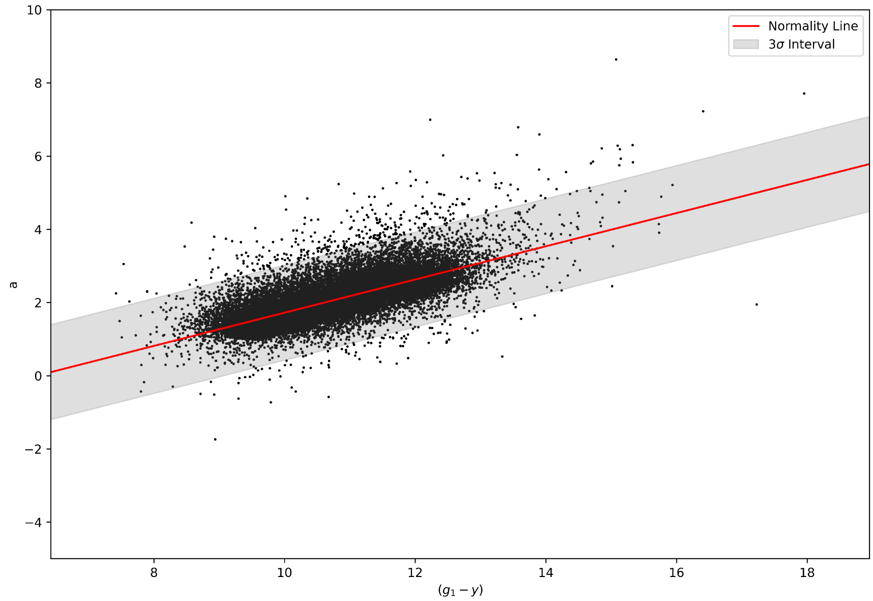

(a) Linear fit for the Δa-photometry.

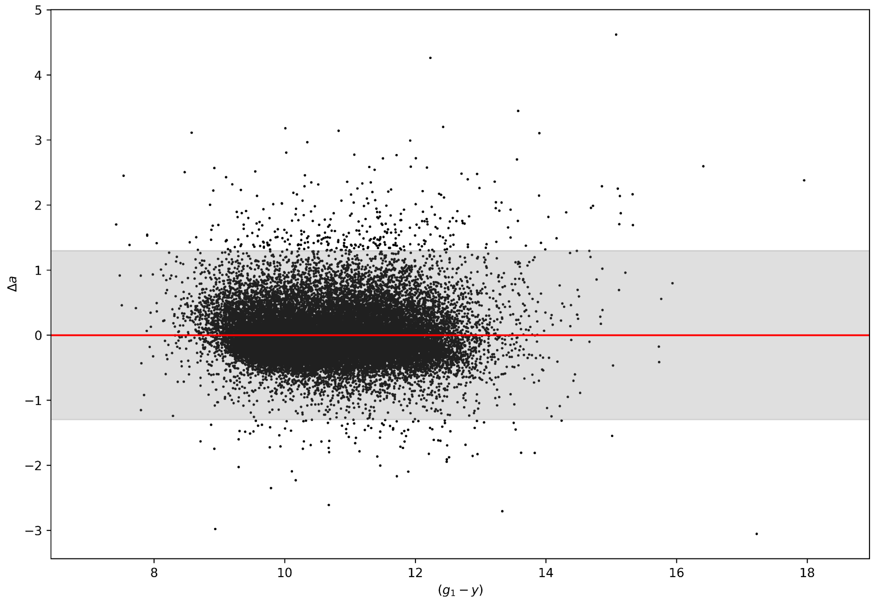

(b) Same as (a), but de-trended to see the Δa values more clearly.

Figure 3.4.: Result of the Δa-photometry. The normality line is seen in red and the 3σ region is shaded in grey.

- `libnor36`
  In this library, stars between spectral types O6-M5 are included. These spectra

have been normalised to the flux at ∼ 4500Åand have a resolution of 3.6Å

- `libr18_225`
  This was derived from the `libr18` library. However, the spectra were smoothed to a resolution of 2.25Å.

- `librlamost`
  This library gives spectra in the range of O9-K0 stars with roughly the same resolution as the LAMOST spectra.

Additionally, one can put together a custom library for special use cases.
The classification is done via a simple command line prompt:

```
mkclass spectrum library output log R NI
```

- `spectrum` is the path to the file in which the spectrum is saved
- `library` is the desired spectral library (see above)
- `output` is the created outfile that includes the determined spectral type(s)
- `log` is the log file containing more detailed information on the classification process
- `R` is the so-called "roughtype" (1 for rectified spectra and 2 for either rectified or flux-calibrated spectra)
- `NI` is the number of iterations to be used for the determination of a spectral type

After this, the code reads the spectrum, does some pre-processing (e.g. smoothing, normalising, etc.) if needed. At first, a initial spectral type is assigned, which gets then compared to the standards of the library. After `NI` iterations, a final spectral type is written to `out`. The output includes the name of the file the spectrum is stored in, the determined spectral type and a quality flag. The quality flag can take the values "poor", "fair", "good", "vgood" and "excellent" and is basically a measure of the S/N of the input spectrum. All together, a line in the output file looks like this:

```
J034406.47+314324.9 | F6 V Sr | good |
```

The results of this automatic classification are comparable to the classification done by the eyes of experienced astronomers. The results deviate by only about 0.1 sub-classes and approximately half a luminosity class for spectra with a high S/N(Gray & Corbally, 2014). Note that only spectra in the wavelength region from 3800-5600Å can be classified by the current version (v1.07). See Fig. 3.5 for an example of the classification output.
A few randomly selected spectra were checked for a quality assessment of the automatic classification. In general, MKCLASS provides good classification, with a scatter of a few subclasses and some ambiguity in the classification of the exact type of peculiarity, which is more true for spectra with poorer S/N.

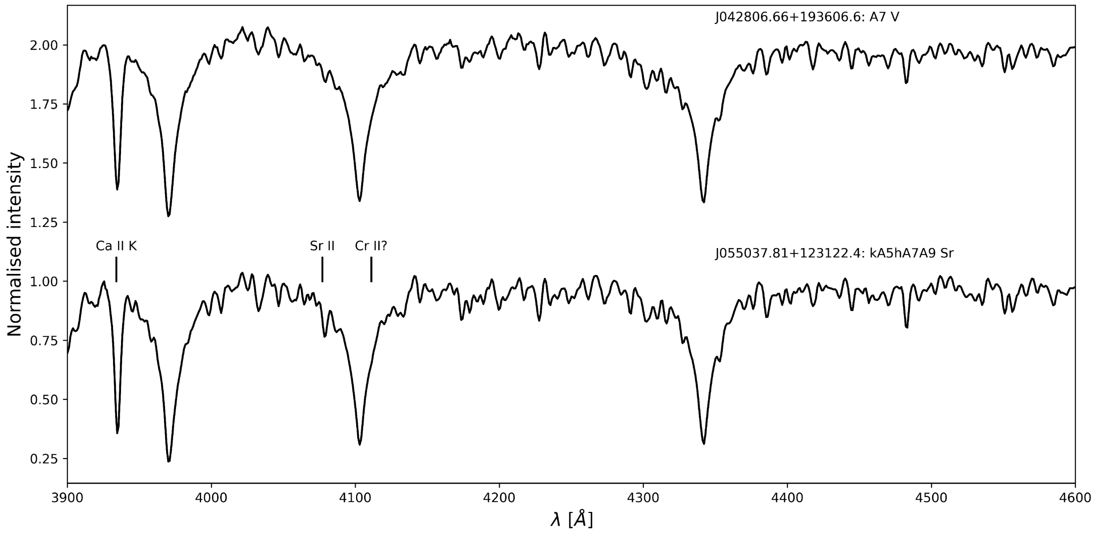

Figure 3.5.: Example plot of a non-CP spectrum of spectral type A7 V (upper) and a CP star of spectral type kA5hA7mA9 Sr (lower). A few spectral lines of interest have been noted: the $\lambda 4077$ line of Sr II and a possible (albeit unlikely) contribution of the Cr II line in the flank of the $H\delta$ line. Both spectral types have been determined using MKCLASS. The IDs are from LAMOST.

3.5. Photometric variability

3.5.1. Light curves and preparation

The stars in the sample were cross-matched to the TICv8.2 (Paegert et al., 2021) in order to check for variability. Using the python package `eleanor` (Feinstein et al., 2019), light curves from the subset of the associations in Kerr et al. (2021). This process used a clever method developed by Feinstein et al. (2019) who created a "postcard" for each source from the FFI where the source is in the centre. Then, each pixel can be read out separately, creating a light curve for each one. This is especially useful when one wants to minimise the effect of blending in denser regions. However, due to the large pixel scale of TESS ($21'' \times 21''$ fall on a pixel, Ricker et al. (2015)), some contamination by nearby and/or brighter stars is almost inevitable. An example of this process can be seen in Fig. 3.6.

For this work, a circular mask with a radius of 1 pixel was used. The light curves were extracted and normalised using `eleanor`, then saved into individual ascii files for each source. After a 3σ-cut to remove outliers, the flux values were transformed into

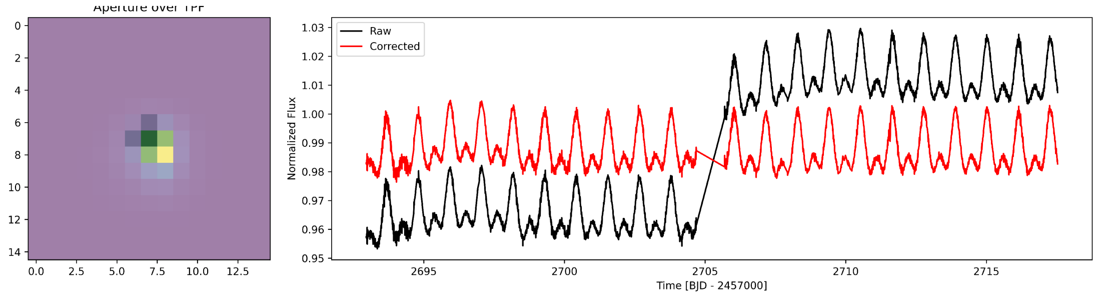

Figure 3.6.: Process of extracting the lightcurves for a circular mask (see text). *Left:* Target pixel file with aperture. *Right:* Raw (black) and corrected (red) normalised flux. The corrected flux values have been shifted down by 1.5 per cent for clarity.

magnitude differences using the relation known as Pogson's ratio[8]:

$$\Delta mag = -2.5 \cdot log_{10}\left(\frac{F}{F_0}\right) \tag{3.12}$$

where F_0 is the mean flux of the light curve and F are the flux values extracted by `eleanor`.
Similarly, the magnitude errors were calculated using standard error propagation

$$\sigma_y = \left|\frac{\partial y}{\partial x}\right| \sigma_x$$

resulting in

$$\sigma_{mag} = 2.5 \cdot log_{10}\left(1 + \frac{\sigma_F}{F_0}\right) \tag{3.13}$$

A total of 1,022 light curves were downloaded and stored in an ascii file for each source containing the three columns Barycentric Julian Date (BJD), normalised flux and flux error.

3.5.2. Frequency analysis

A periodogram that is commonly used for frequency analysis can be created in many ways. One of the most common methods is the Discrete Fourier Transform (DFT). The N measurements $X(t)$ of a time series are transformed to the frequency domain via

$$\mathcal{F}(\omega) = \sum_{k=1}^{N} X_k(t) e^{-i\omega t} \tag{3.14}$$

[8]Norman Robert Pogson introduced the mathematical definition of magnitude differences in the 19th century. He stated that a star of magnitude 0 is $\sqrt[5]{100} \approx 2.512$ times brighter than a star of magnitude 1.

where the power (amplitude) of a frequency ω is given as

$$P(\omega) = \frac{1}{N}|\mathcal{F}(\omega)|^2 = \frac{1}{N}\left[\left(\sum_k X_k \cos(\omega t_k)\right)^2 + \left(\sum_k X_k \sin(\omega t_k)\right)^2\right] \tag{3.15}$$

In reality, the formulation is slightly different since the DFT is very inefficient on larger data sets ($\mathcal{O}(N^2)$). To implement the algorithm on a large set of input values $X(t)$, it is better to use the Fast Fourier Transform (FFT) which makes use of the properties of the DFT in terms of symmetry and periodicity, reducing the complexity down to $\mathcal{O}(NlogN)$ and thus making it much more efficient.
This method, while it works relatively well and efficient, has some shortcomings when it comes to unevenly sampled datasets. For example, frequencies that are not included in the data but instead arise from the uneven sampling (e.g. day-night cycle for ground-based observations) can be included.
A better method to get accurate results is the Lomb-Scargle periodogram (Lomb, 1976; Scargle, 1982). In this case, the power spectrum is a measure of the significance of the frequency.

$$P(\omega) = \frac{1}{2}\left(\frac{\left[\sum_k X_k \cos(\omega(t_k - \tau))\right]^2}{\sum_k X_k \cos^2(\omega(t_k - \tau))} - \frac{\left[\sum_k X_k \sin(\omega(t_k - \tau))\right]^2}{\sum_k X_k \sin^2(\omega(t_k - \tau))}\right) \tag{3.16}$$

where τ is defined via

$$\tan(2\omega\tau) = \frac{\sum_k \sin(2\omega t_k)}{\sum_k \cos(2\omega t_k)} \tag{3.17}$$

A detailed description of this method can be found in VanderPlas (2018).

Luckily, there already is an implementation readily available: The `astropy` package (Astropy Collaboration et al., 2013, 2018, 2022) has an efficient implementation following the algorithm from Zechmeister & Kürster (2009). Another advantage is that the uncertainties in the measurements are taken into account when calculating the periodogram. Additionally, one does not need to specify the Nyquist frequency, it can be done automatically based on the input data. The periodogram gets created in just a single line of code from the measurements of time (`t`), magnitude (`mag`) and magnitude error (`mag_err`):

```
from astropy.timeseries import LombScargle

frequency, power = LombScargle(t,
                               mag,
                               mag_err).autopower(
                               minimum_frequency = 0.001,
                               nyquist_factor = 1)
```

This results in power spectra with frequencies up to around 70 c/d, which is enough to even get the signals from rapidly oscillating Ap (roAp) stars that pulsate with periods of around 5-25 minutes (e.g. Holdsworth (2021)). However, without additional information via spectroscopy, those are difficult to discriminate from another class of pulsating variable stars, the so called δ Scuti (DSCT) variables that generally have longer periods but can have similar properties than the roAp stars.
After the frequency analysis, the strongest period is calculated as the inverse of the frequency with the highest power. This was done in two frequency domains. Once below 5 c/d ($P = 0.2$d) and once above this threshold. The reason for doing this is that sometimes a stronger signal in one domain can overpower the signals in the other domain that may belong to the true variability of the star, making an accurate classification very difficult, if not impossible. Finally, the light curves were folded at this period. An example of this process can be seen in Fig. 3.7.
Additionally, the False Alarm Probability (FAP) of the strongest periods were estimated. The default method used by `astropy` to calculate the FAP is the one described by Baluev (2008). In short, if a period with a power P is known, its probability of being a false signal can be estimated via

$$FAP \approx e^{-P} \tag{3.18}$$

When dealing with an unknown frequency somewhere in the interval $[f_1, f_2]$, one has to take the number of independent frequencies N in this range into account. The FAP then becomes

$$FAP \approx 1 - (1 - e^{-P})^N \tag{3.19}$$

A frequency with a FAP smaller than 10^{-2} is likely to be real and below 10^{-3} one can be certain. Above those thresholds, it is very likely that the found frequency is not real an thus should not (or only with great caution) be considered.

3.5.3. Classification of variability types

The names of the variability classes were taken from the Variable Star Index (VSX)[9] (Watson et al., 2006).
Problems with the classification emerged due to several issues with the data. First, the large pixel size of the detector. For some sources, it is not clear if the signal comes from the star in question or some other source nearby that falls on the same pixel. So one has to keep blending effects in mind when working with those data products. Another difficulty stems from instrumental noise that can "overpower" the signal from the star and thus loosing the signal. This is a problem especially with fainter sources and/or for stars with low amplitudes. Those low amplitudes are the third problem when it comes to classifying stars. One has to be cautious with amplitudes lower than about 5 mmag and below 2 mmag a star gets almost impossible to classify unless there is a clear variability

[9] `https://www.aavso.org/vsx/index.php?view=about.vartypes`

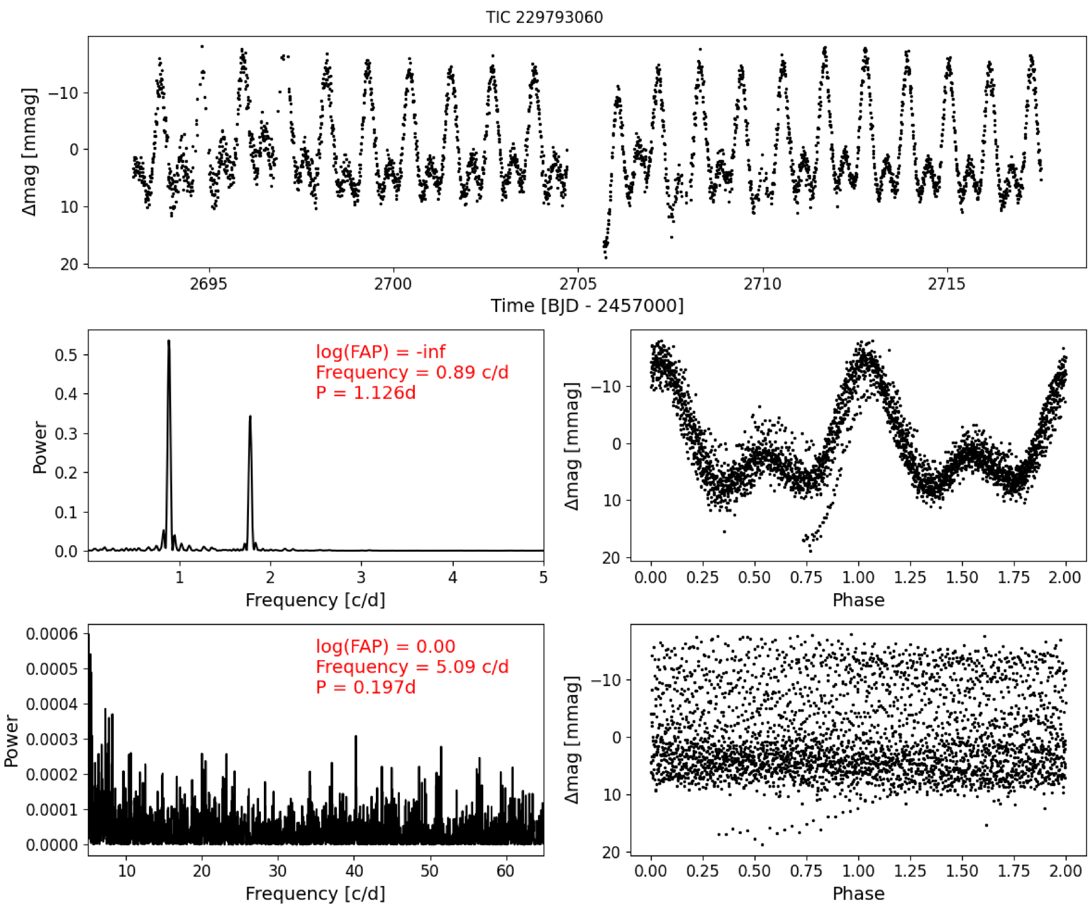

Figure 3.7.: *Upper:* Final light curve of the ACV variable TIC 229793060 (EE Dra/HD 177410, see also Fig.3.6) as observed with TESS *Middle-left:* Lomb-Scargle periodogram in the region up to 5 c/d. *Middle-right:* Phased light curve of this frequency region. The small bump in the minima (= the double wave) is clearly visible. *Lower-left:* Periodogram for frequencies above 5 c/d, note the comparatively small power of the peaks. *Lower-right:* Phase folded light curve at the highest peak above 5 c/d. No variability can be seen and thus the signal is most likely noise which is also indicated by $log(FAP) = 0$
In the periodograms, the frequency of the highest power, the corresponding period and the FAP are given in red.

pattern visible. Last, but not least, there may be some ambiguity with some classifications as pointed out in e.g. Skarka et al. (2022) who described similarities between that light curves of elliptic variables, binary stars the do not eclipse each other but are still in a close system (Morris, 1985) and rotationally modulated (ROTM), spotted stars that rotate. In extreme cases, they can only be discriminated using spectroscopic observations.

The most prominent variable types in the temperature region in question can be put in two major groups: pulsating variables and rotating variables.

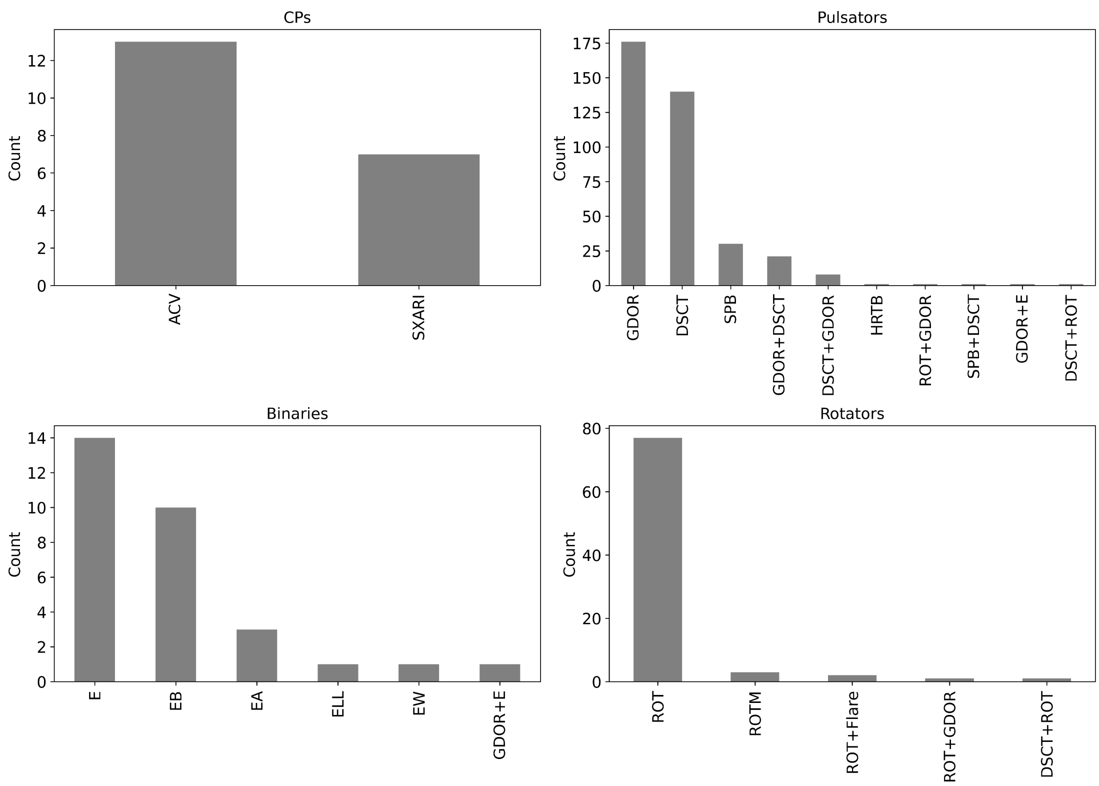

Figure 3.8.: Result of the classification of the light curves from TESS sorted divided into CP stars, pulsating stars, binary stars and rotating stars. Note that some classes show up in multiple categories due to them being hybrids.

Pulsating variables

The pulsational variables found here are mostly the γ Doradus (GDOR) and δ Scuti (DSCT) stars.
The GDOR variables pulsate in periods of hours to days (e.g. Balona et al. (1994)). The origin of the pulsations lie in the gravity waves in the interior of the stars Kaye et al. (1999); Guzik et al. (2000).
DSCT stars, on the other hand, are faster p-mode pulsators and have periods from minutes to hours. A subtype of those are the roAp stars.
Pulsating stars of this type are also subjects of studies using asteriseismic analysis trying to unravel the inner structure and workings of those stars.

Rotating variables

Here, we can use the distinction between three subgroups (see e.g. Skarka et al. (2022) for details): the rotationally modulated (ROTM), stars with spots due to abundance anomylies (e.g. the ACV or SXARI variables). Stars that show a basic periodic pattern associated with rotation where a pulsation pattern can also be seen (ROTS) and just stars that seem to rotate and have basic periodic forms in their light curve (ROT).
The variables of interest in this class of stars are the ACV and SXARI stars.
ACV variables tend to show a smaller maximum between two maxima, the so-called *double wave* (Figs. 3.6,3.7) with periods ranging from about half a day up tu usually less than ten days. How well one can see the double wave is determined by the angle at wich we look at the star and the obliquity angle of the magnetic axis. It is most prominent when we look directly at the magnetic pole that is not directly on the pole of the star. SXARI variables are just the hotter ($T_{\text{eff}} > 10,000$K) analogues of those stars.

Binaries

Another class of variables commonly seen are binary stars that eclipse each other. A prime example would be Algol (β Per, HD 19356, $P \approx 2.9$d (e.g. Richards et al. (2012))).

3.5.4. Issues with classifying variability

Of course, classifying stars based on their light curve and frequency spectrum alone is not always a straightforward affair. Sometimes, one needs additional information from spectra or other means to get a hold of the spectral type and thus an approximate estimation of the effective temperature that can influence the final classification. As already mentioned above, there is a cut-off between the SXARI and ACV variables, for example. If a classification based on temperature is not available, one still can make an educated guess on the type of variability.
A much more significant problem, however, can be the method of determining the frequency and thus the period of the variability itself. Taking the strongest peak as the most significant one is not always the best method, because there still can be some instrumental noise overpowering the variability of the star. Thus, one might need to tend to other methods to get the true variability. an example of this method is the so-called *pre-whitening* where the strongest frequency gets removed one after the other until only noise remains.
In this thesis, however, the interest primarily lies in the signals coming from ACV and SXARI variables, since these classes are the ones associated with peculiarity of mCP stars. roAp stars, while exhibiting similar pulsational variability as DSCT stars, can only be discriminated via spectroscopy. Accordingly, ambiguity in the frequency spectrum of those rotating stars is not a big concern, unless the amplitude is really low (below 2-3 mmag).

Because of these mentioned issues and the blending effect, there is a chance that a good fraction of the variables are classified incorrectly.

Out of the 1022 downloaded light curves, 512 show clear sign of variability. Those can be sorted into four main groups:

- CP stars (20)
- Pulsating stars (380)
- Binary or eclipsing stars (30)
- Rotating stars (84)

The distribution of those can be seen in Fig. 3.8.

Additionally, I also matched the list to the VSX (Watson et al., 2006). 73 Stars were also listed there with the classifications being generally similar to this work although differentiating in some cases. However, for the stars, the classifications and periods matched.

3.6. Spectral energy distribution

To look for possible PMS sources among the ∼970 stars that were determined to be CP stars via one or more of the methods above, the stars, or more accurately their coordinates, were put into the *Virtual Observatory SED Analyzer* (VOSA)[10] (Bayo et al., 2008). This online tool searches for the available photometric data[11] of each source and then makes a fit to determine a SED of the star in question. Additionally, it has incorporated fitting routines that detect IR excess, which is important when trying to look for PMS sources. For each star, the position from *Gaia* DR3 was submitted to VOSA in the format of Tab. 3.1.

The columns are mandatory and explained as such:

- `object`: Simply the identifier of the object that should be analysed. Can be a custom name or some catalogue name (HD, BD, 2MASS, TIC, KIC, ...) in the present case, the *Gaia* source IDs are used.
- `RA`: The right ascension (in degrees) of the object
- `DEC`: The declination (in degrees) of the object
- `dis`: The distance of the object
- `AV`: The interstellar extinction in the V-band
- `Filter`: The specified filter a magnitude or flux is given

[10] `http://svo2.cab.inta-csic.es/theory/vosa/`

[11] 2MASS, *Gaia*, WISE, SDSS, ...

- `flux`: The magnitude or flux of the filter given in the previous column. For each filter,a new row for the object must be created
- `error`: The error on the flux or magnitude from the previous column
- `PntOpts`: Options specific for this photometric point
- `ObjOpts`: Options specific for the object in question

A more detailed description of the columns and options can be found on the VOSA website[12].
The only real mandatory column is the object name. However, one should at least include coordinates to avoid confusion and be sure the right object gets found. VOSA can then look through available online catalogues to find photometry and extinction measurements. If one value is not available or not known, one must use the string `---` as entry.
I only submitted the source IDs along with the coordinates of the stars in order to get the best (and most consistent) estimate for the distance end extinction values (see Tab. 3.1). A drawback is that not for every source, extinction measurements can be found. This is especially a problem when one wants to fit models containing stellar parameters (T_{eff}, $L/L_{\odot}$, ...) to the obtained SED from the photometry found byVOSA. However, for the purpose at hand - finding the IR excess - it is not that big of a problem.
An example of the final SED as plotted by VOSA can be seen in Fig. 3.9 and a SED with infrared excess in Fig. 4.6.

object	RA	DEC	dis	AV	Filter	flux	error	PntOpts	ObjOpts
5436414262899903872	144.758026599	-36.8957462252	---	---	---	---	---	---	---
2930678291716664192	110.6468958454	-18.7128327504	---	---	---	---	---	---	---
461829660022360832	50.9858722868	59.2404583724	---	---	---	---	---	---	---
5960713736908382336	265.154749423	-40.215150668	---	---	---	---	---	---	---
5881393391868603264	226.2472773804	-55.642708724	---	---	---	---	---	---	---
5881395625251644288	226.3794959978	-55.5355250987	---	---	---	---	---	---	---
5881396037568526336	226.3932142099	-55.5146884818	---	---	---	---	---	---	---
5881345799292540288	226.3714392948	-55.6714580578	---	---	---	---	---	---	---
5881345837987362304	226.3868238292	-55.6688597168	---	---	---	---	---	---	---
...	...	...	...	...	...	...	...	...	...

Table 3.1.: Example VOSA input for a few sample stars. See text for details on the columns.

3.7. Hydrogen emission lines

In addition to the SED, another sign of stars still in their accretion phase and thus in their PMS phase is emission in at least one of the lines of the Balmer-sequence. This is mostly true for the Hα line, since it is the strongest one. In the spectral region associated with CP stars, the objects with emission lines are called Herbig Ae/Be stars. They have masses between $2 - 10\text{M}_{\odot}$ and also show circumstellar disks as a result of their evolutionary status. See Brittain et al. (2023) for an extensive review on that matter.

[12] `http://svo2.cab.inta-csic.es/theory/vosa/helpw4.php?otype=star&what=format`

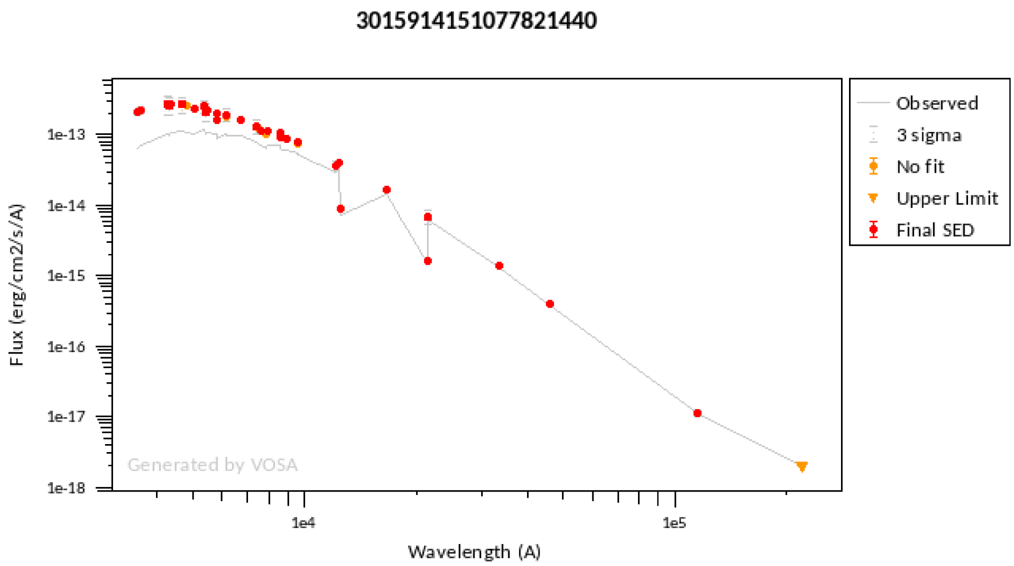

Figure 3.9.: Example SED as calculated by VOSA. The dots indicate the photometry used in the fit and the grey line is the SED before correcting for extinction. The title of the figure is the *Gaia* DR3 ID.

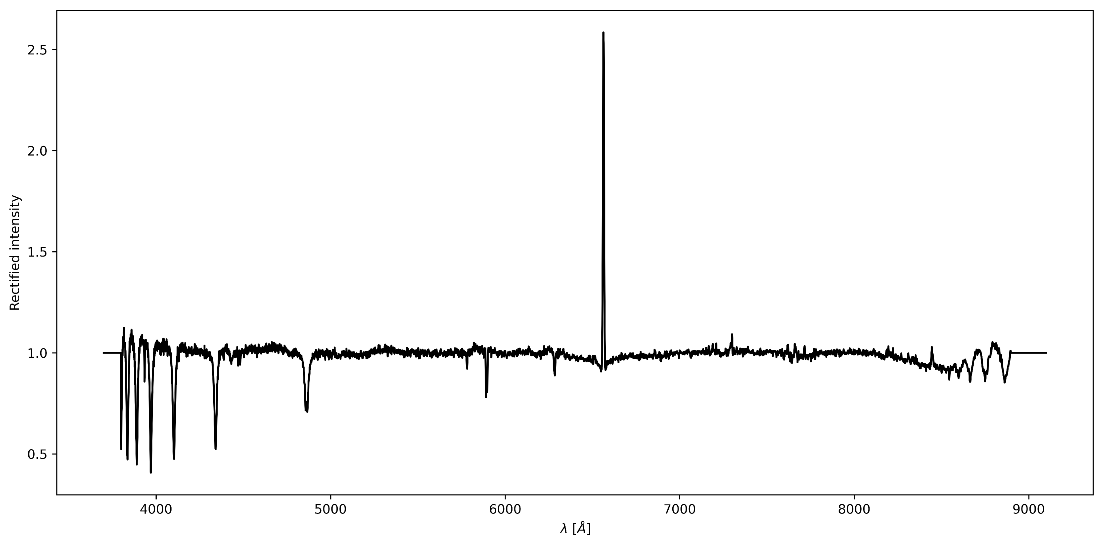

Figure 3.10.: Example LAMOST spectrum of an emission line star. The Hα line is clearly visible.

Paunzen et al. (2024) propose a new way of detecting Hα emission in the *Gaia* BP/RP spectra by using one narrow and one wide synthetic filter centred on the Hα line. They selected a variety of known emission line stars with available *Gaia* BP/RP spectra. Then they calculated an Hα index in the same way the Hβ index is calculated (Strömgren, 1966) using synthetic photometry via the two filters seen in Fig.3.11. Both filters are centred at $\lambda = 6555$Å with the wider one having a Full-Width-at-Half-Maximum (FWHM) of 125Å and the narrow one has a FWHM of 35Å. Then the Hα index is calculated as

$$H\alpha = \frac{H\alpha_{\text{wide}}}{H\alpha_{\text{narrow}}} \tag{3.20}$$

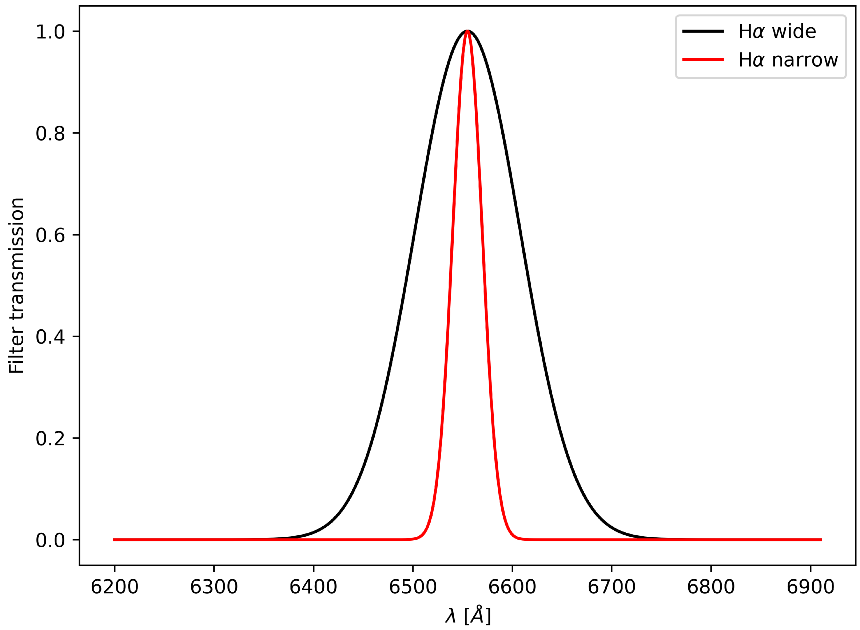

Figure 3.11.: Filter curves used in Hα photometry.

If this value is smaller than a certain threshold, one can assume the star in question to show emission lines.

I used a similar approach with the LAMOST spectra where some are suspected to be PMS sources.
The spectra from LAMOST were treated in the same way as the *Gaia* BP/RP spectra, meaning they were interpolated by a cubic polynomial in order to resample the resolution to 1Å. Then, they were normalised to unity at a common wavelength of $\lambda = 4020$Å. The synthetic magnitudes of the filters g_1, y (Fig. 3.3) and the two Hα filters were then computed in the same way as done in the Δa photometry. However, in contrast, the filter curves needed to be changed slightly in contrast to Paunzen et al. (2024), meaning the gaussian curves for the filters used here were centred at $\lambda = 6564$Å for the best result.. The result of the synthetic photometry can be see in Fig.3.12.

To check which stars have emission lines in this spectral region, I used the specutils[13] (Earl et al., 2024) library to search for emission line stars.
specutils has an easy to use routine for finding emission lines. One needs to create a Spectrum1D object from the spectrum in question. Then it is truncated to a region around the Hα line, i.e. to $\lambda 6550 - \lambda 6570$Å. The line is then detected via a short piece of code:

```
import numpy as np
from specutils import Spectrum1D, SpectralRegion
from specutils.fitting import find_lines_threshold
from specutils.manipulation import extract_region
import astropy.units as u

lam, flux = np.genfromtxt('J052805.13+342130.3', unpack = True)
spectrum = Spectrum1D(spectral_axis = lam * u.AA, flux = flux *
                u.dimensionless_unscaled)

region = SpectralRegion(6550 * u.AA, 6570 * u.AA)

truncated_spectrum = extract_region(spectrum, region)

lines = find_lines_threshold(truncated_spectrum, noise_factor = 3)
emission_lines = lines[lines['line_type'] == 'emission']
```

The result is a table of the form

```
  line_center    line_type line_center_index
    Angstrom
    float64         str8          int64
---------------- --------- -----------------
6562.96533203125  emission                15
```

While it is not perfectly certain, one can clearly see that most of the emission line stars lie below H$\alpha \approx 2$. This is not a strict criterion but can help in identifying emission line stars. The fact that not all of the stars below that threshold may suggest that either the filter curves are not perfectly chosen or that there is some issue with the spectra themselves.

Out of the detected CP stars, 12 also show emission lines.

[13] https://specutils.readthedocs.io/en/stable/

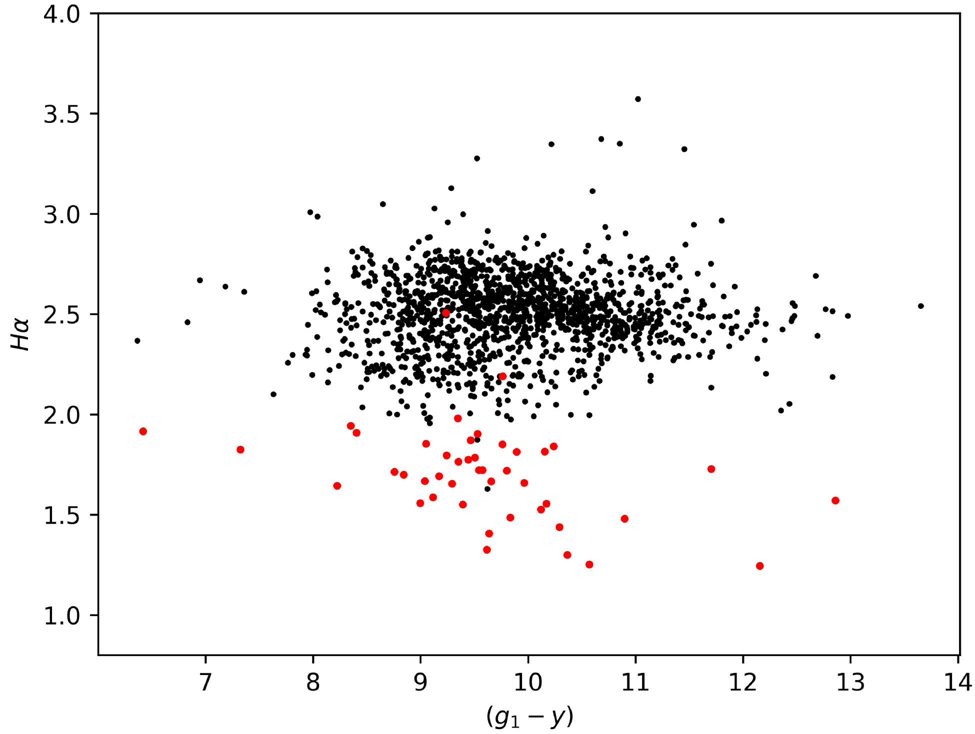

Figure 3.12.: Hα photometry of LAMOST spectra. The stars showing hydrogen emission are shown in red.

4. Results

In this chapter, I want to discuss the stars that were detected via the methodology in chapter 3.

4.1. Detected CP stars/candidates

4.1.1. Detection via Δa-photometry

From the Δa photometry using the *Gaia* BP/RP spectra (see Section 3.3), 341 stars with a flux depression at 5200Å were detected. Three of those stars also have a spectral type from the LAMOST spectra that confirms the CP nature of the stars (Tab. 4.1).

***Gaia* DR3**	**LAMOST**	α	δ	libnor36	libr18	libr18_225	Δa
253428535333057920	J042756.29+442830.8	66.985	44.475	kB9.5hA1mA2 Si	kB9.5hA2mA5 SrSi	kA0hF0mA6 SiEu	1.519
253436747311206528	J042906.36+442429.2	67.277	44.408	A0 II-III Si	A0 II-III Si	F1 V Fe-5.9	2.014
3344712726726459520	J061909.56+143120.1	94.790	14.522	kA1hA2mA5 Si	A0 III-IV SrSi	kA1hA8mA8 SiEu	1.357

Table 4.1.: Stars that have a positive Δa value and a spectral type from LAMOST

4.1.2. Spectroscopic detection

The classification coming from the LAMOST spectra using MKCLASS resulted in 608 CP stars or candidates. Especially interesting are a few stars of Lam Boo type. See e.g. Fig. 4.3 for an example. The whole list of the stars with a CP type in at least one spectral library can be seen in appendix B

4.1.3. Detection via photometric variability

20 light curves have characteristics commonly associated with CP stars. Out of those, 13 are ACV variables and 7 are SXARI stars. The periods of the variability range from roughly 0.4 to 4 days.

4.2. PMS CP stars

4.2.1. Infrared excess

Up to today, not much is known about the (very) early stages in the evolution of CP stars. As already mentioned in chapter 1, there are only a hand full of known CP stars or candidates in their PMS phase, almost all of them being mCP stars. Alltogether, 91 CP

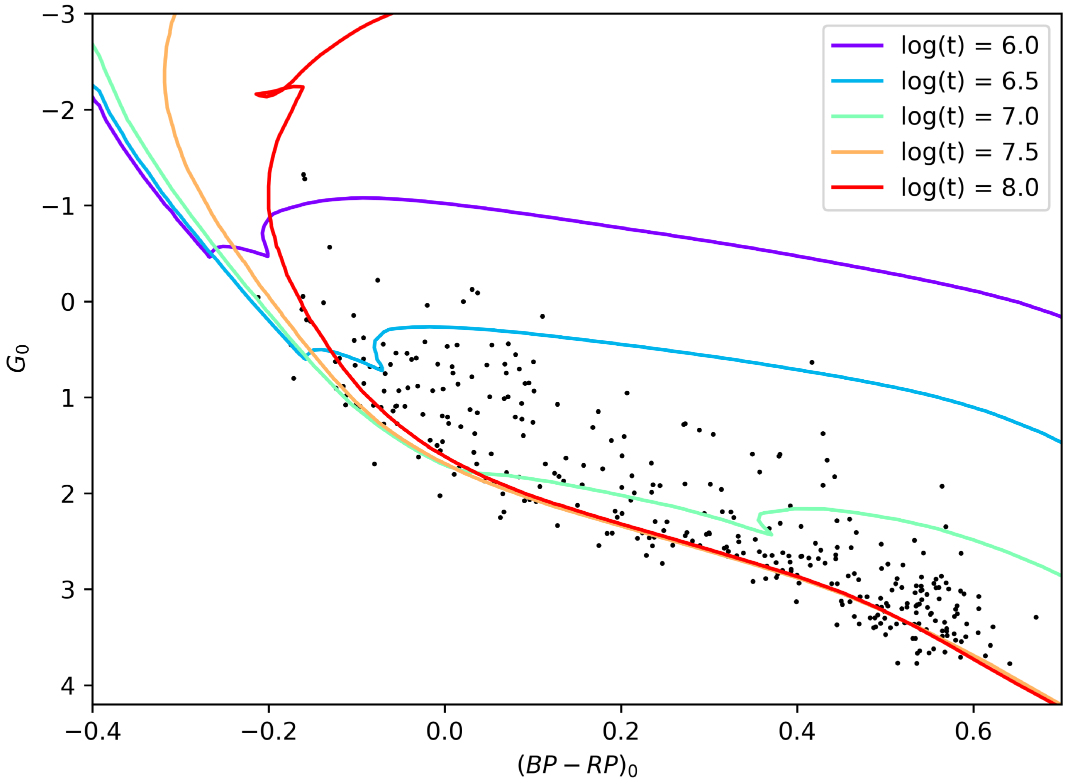

Figure 4.1.: CMD of CP candidates detected via the Δa-photometry. The corrected $(BP - RP)_0$ values are from Anders et al. (2022) and the isochrones are from Bressan et al. (2012) and were generated using solar metallicity values ($Z = 0.0152$).

stars and candidates have been found to show IR excess. An example of such a SED can be seen in Fig. 4.6.

The CP stars showing excess are distributed among the three methods used to find their CP nature as such:

- Light curves: 0/22
- Δa photometry: 59/341
- Spectral classification: 45/608

Put together, there are 104 CP candidates that show IR excess.

Looking at the excess data, i.e. the wavelength region where the excess stars, which is in the mid- to far infrared regions (see also Appendix B), one can deduce that the IR excess is relatively weak and the disks of debris around the stars in question either have dissolved or we are looking at them at some inclination.

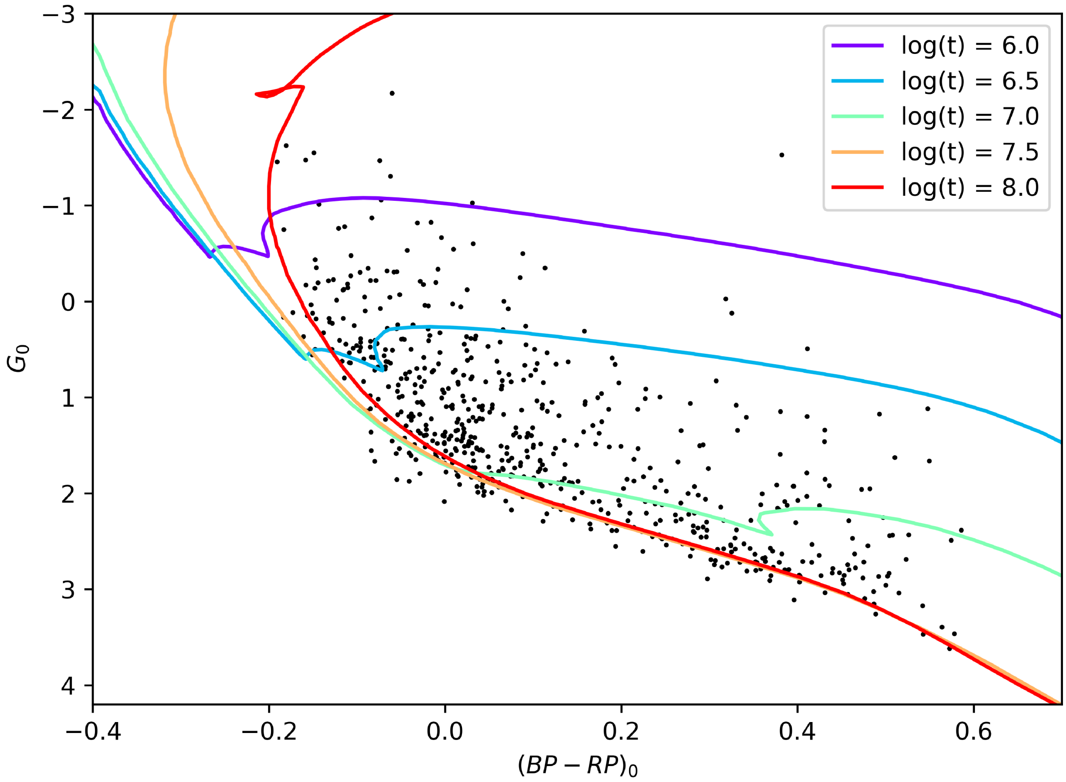

Figure 4.2.: Same as Fig. 4.1 but for the spectroscopically determined CP candidates.

4.2.2. Hydrogen emission

The second criterion for a star being in the early stages of evolution is the emission of hydrogen. I checked for emission on the Hα line of the LAMOST spectra. The result shows that 12 of those stars show emission line and thus are very likely PMS sources that still accrete material onto their surfaces.

4.3. Cross match with literature

To check, whether or not some stars in the sample have already been classified as CP stars, I matched them with various already published lists from the literature. Whenever possible, the cross-match was performed on the *Gaia* DR3 source ID. In other cases, a search cone with a radius of 1″ around the target was used in order to get the most likely match. The matching was performed using TOPCAT[1] (Taylor, 2005).

[1] https://www.star.bris.ac.uk/~mbt/topcat/

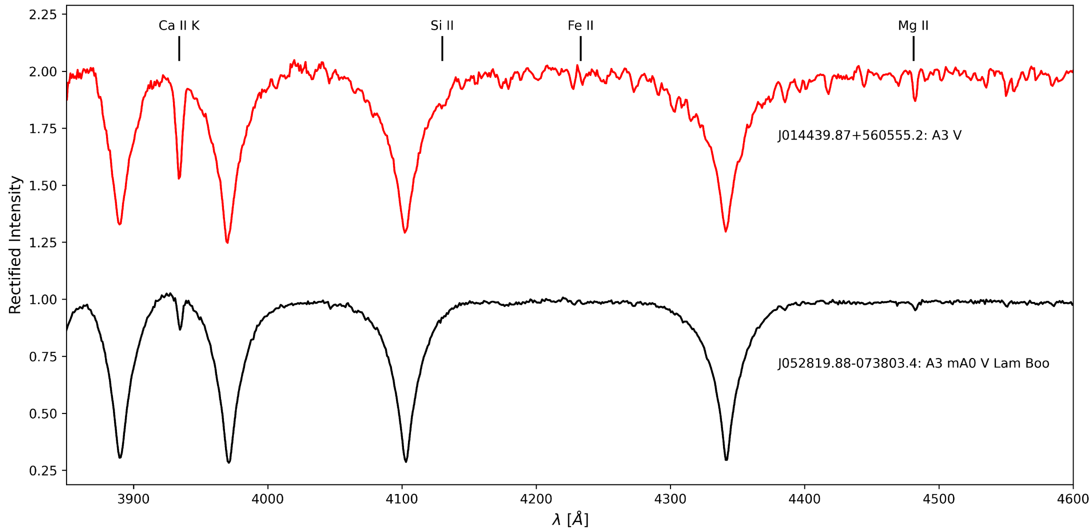

Figure 4.3.: Spectrum of the newly detected Lam Boo star *Gaia* DR3 3015083710562928640/LAMOST J052819.88-073803.4 classified as A3 mA0 V Lam Boo in all three libraries of MKCLASS in black. For comparison, an A3 V star is plotted above with a few spectral lines of interest marked. Note that apart from the weak Ca II K line and the (very) weak λ4481 Mg II line, no significant spectral lines can be seen in the Lam Boo star. Also the hydrogen lines are broader than the one in the apparently normal star.

4.3.1. Renson & Manfroid (2009)

This is an extensive catalogue containing 8,205 CP stars or CP candidates. It contains stars that have been previously mentioned/classified as CP stars in the literature. Although it is not a perfect selection and some stars in this catalogue have been misclassified before and since then proven to be "normal", it is still a a good starting point for an analysis of CP stars. From all the stars in the target list of this work, this catalogue contains 156 sources, out of which nine are also detected in this work.

4.3.2. Qin et al. (2019)

This is a publication dealing with CP stars in the LAMOST data, specifically DR 5. They searched 200,000 using a random forest classifier and additional manual classification. They arrived at a list of 9,372 CP1 and 1,132 CP2 stars. After the classification they also investigated trends in the spatial distribution, particularly the distance from the galactic plane. 27 stars of the target list are contained in this study. The same 27 stars could be detected via this work.

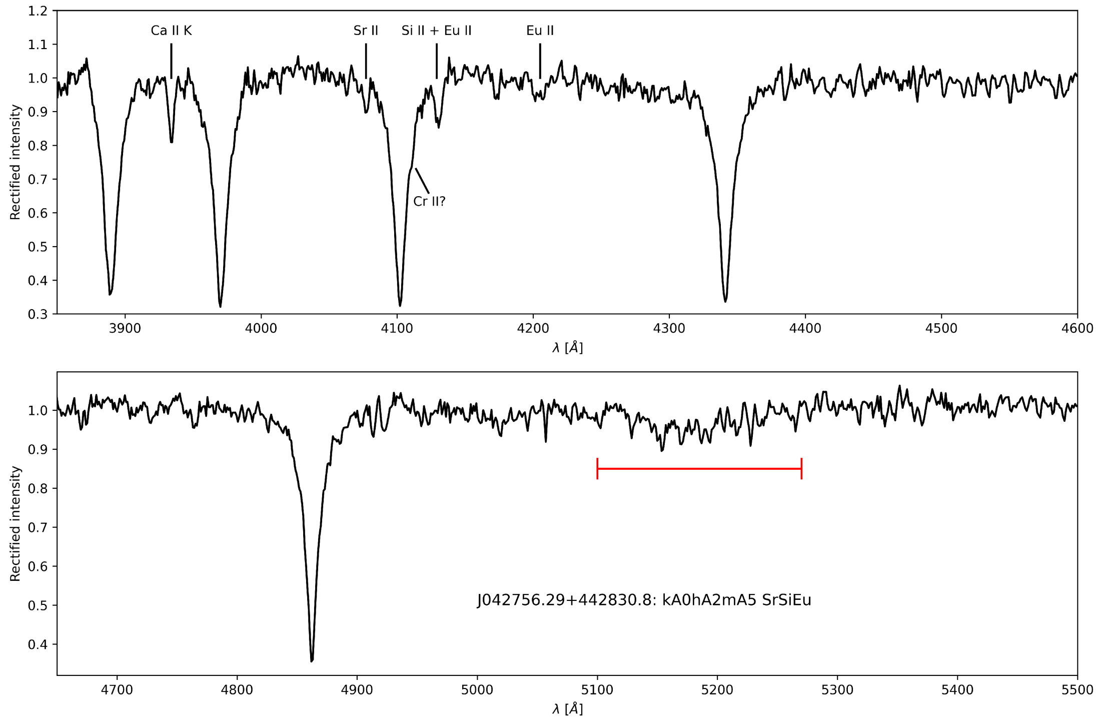

Figure 4.4.: Spectrum of the mCP star *Gaia* DR3 253428535333057920/LAMOST J042756.29+442830.8. It has been classified as kB9.5hA1mA2 Si (`libnor36`), kB9.5hA2mA5 SrSi (`libr18`) or kA0hF0mA6 SiEu (`libr18_225`). The spectral type in the figure corresponds to a manual check. The upper part of the figure shows the blue-violet part of the spectrum used for classification by MKCLASS. A few spectral lines of interest have been annotated. The lower part focuses on the region around the λ5200 flux depression. The red horizontal line shows the approximate extent of the depression.

4.3.3. Hümmerich et al. (2020)

The authors of this collection of 1,002 mCP stars utilised Data Release 4 DR of LAMOST where they searched the spectra using MKCLASS and δa-photometry. They also analysed the final list in regards of the evolutionary stage on the main sequence, mass and spatial distribution. Additionally, a few binary stars are described in the paper. Out of all the targets in this work, it contains four stars, half of those are also detected in my data.

4.3.4. Chojnowski et al. (2020)

The authors of this paper use the infrared Apache Point Observatory Galactic Evolution Experiment (APOGEE) spectra (Majewski et al., 2017) of the Sloan Digital Sky Survey (SDSS) (York et al., 2000) to search for HgMn stars. They detected 260 new ones, making

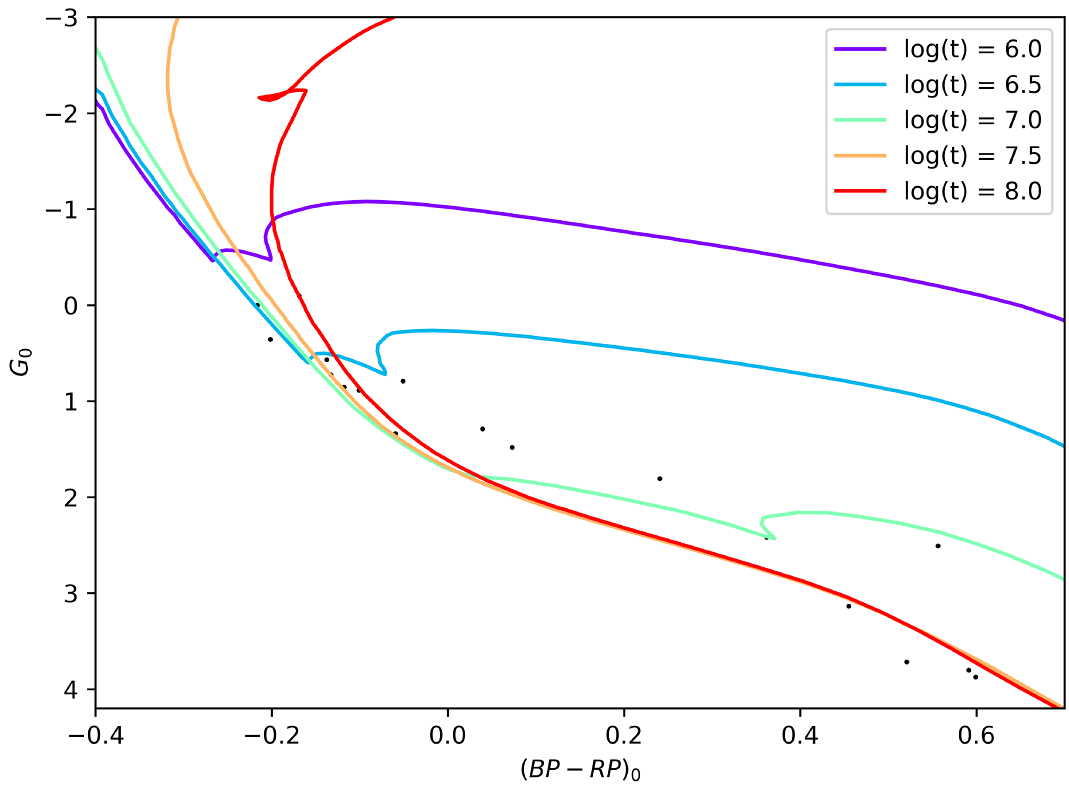

Figure 4.5.: Same as Fig. 4.1 but for the CP candidates found from the TESS light curves.

infrared spectra also relevant for the detection of those objects. In total, seven stars of the present thesis are also included in this catalogue.

4.3.5. Shang et al. (2022)

One of the latest publication on a data release from LAMOST, in this case DR8. Similar to Qin et al. (2019), they use a machine learning algorithm to extract features of CP1 and CP2 stars from the spectra. After the application of the XGBoost algorithm to the spectra, those were again classified manually. The final result is a catalogue of 20,694 stars (17,986 CP1 and 2,708 CP2) with numerous previously unknown CP stars. They also include the basic stellar parameters (T_{eff}, $\log g$, $[Fe/H]$) of the sample. 17 stars are included in the target list of this thesis, 15 could be detected via my methodology.

4.3.6. Yang et al. (2024)

A very recent catalogue of 27,543 CP stars and candidates. In addition to MKCLASS, the authors used an ensemble regression model to classify spectra of LAMOST DR10. Out of the 27,543 CP stars and candidates, they list $\sim 11,614$ new Am stars and candidates as

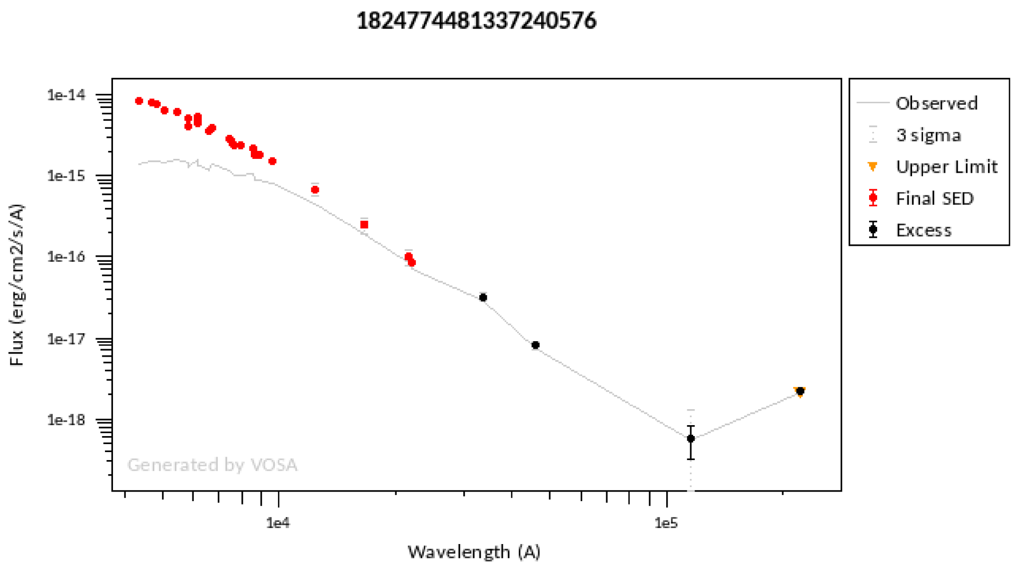

Figure 4.6.: Same as Fig. 3.9, but for a star with IR-excess

well as 4,978 new Ap stars and candidates. Similarly to Shang et al. (2022), they give stellar parameters (T_{eff}, $\log g$, $[Fe/H]$) for their sample.
59 stars in this catalogue could be retrieved in this thesis.

4.4. Colour-magnitude diagram

In total, there are 971 individual CP stars and candidates detected in this work. Most of them have not been named in the literature before.
Figures 4.1, 4.2, 4.5 show the CMD of the CP stars detected via Δa photometry, spectral classification and variabilty from light curves, respectively. Fig. 4.8 shows them all combined.
One can clearly see that there are stars below the ZAMS. This is likely due to the de-reddening and extinction correction performed by `starHorse`. Another explanation seems to be a systematic blueing effect, especially for mCP stars (Hauck & North, 1982; North et al., 1997). Hümmerich et al. (2020) mention inconsistent photometry and/or unresolved binaries as the source of this effect. However, the effect seen in the diagrams of this work is not very strong ($\lesssim 0.05$mag) and may well be an artefact of photometric and numerical errors. Nevertheless, around $(BP - RP)_0 \approx -0.1$ in Fig. 4.8 one can see a small "bump" where the deviation from the ZAMS gets slightly larger which can be a sign of the blueing effect mentioned by North et al. (1997).

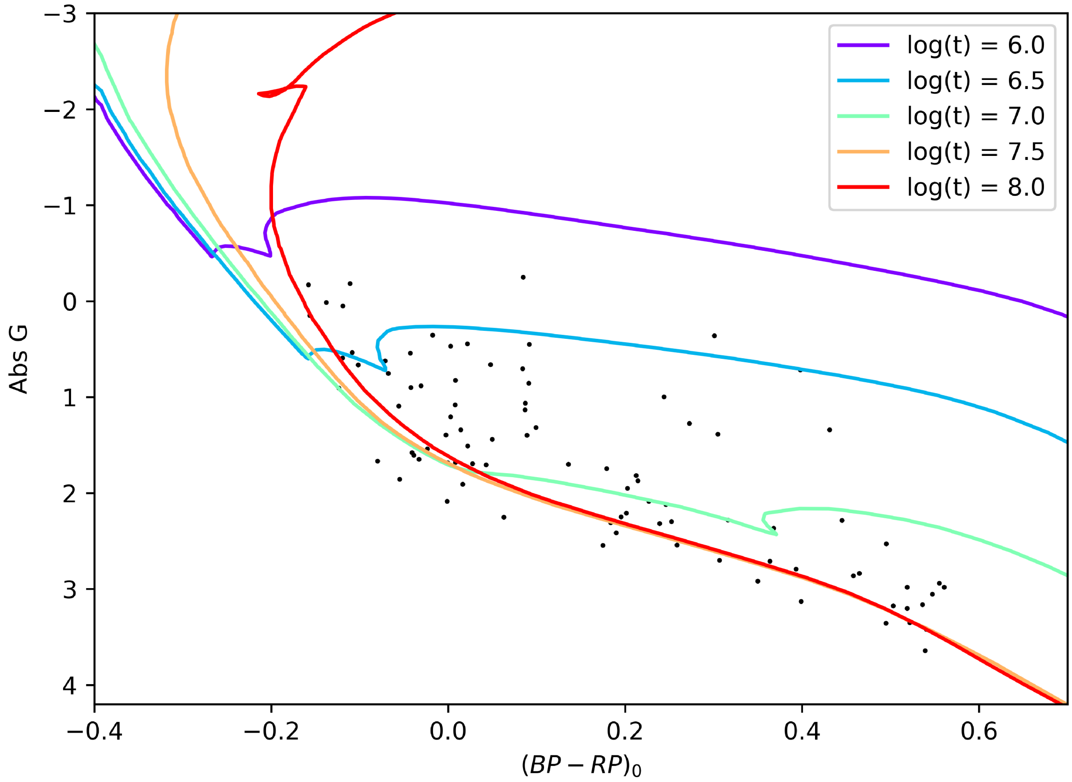

Figure 4.7.: In this CMD the detected CP stars showing infrared excess in their SED can be seen.

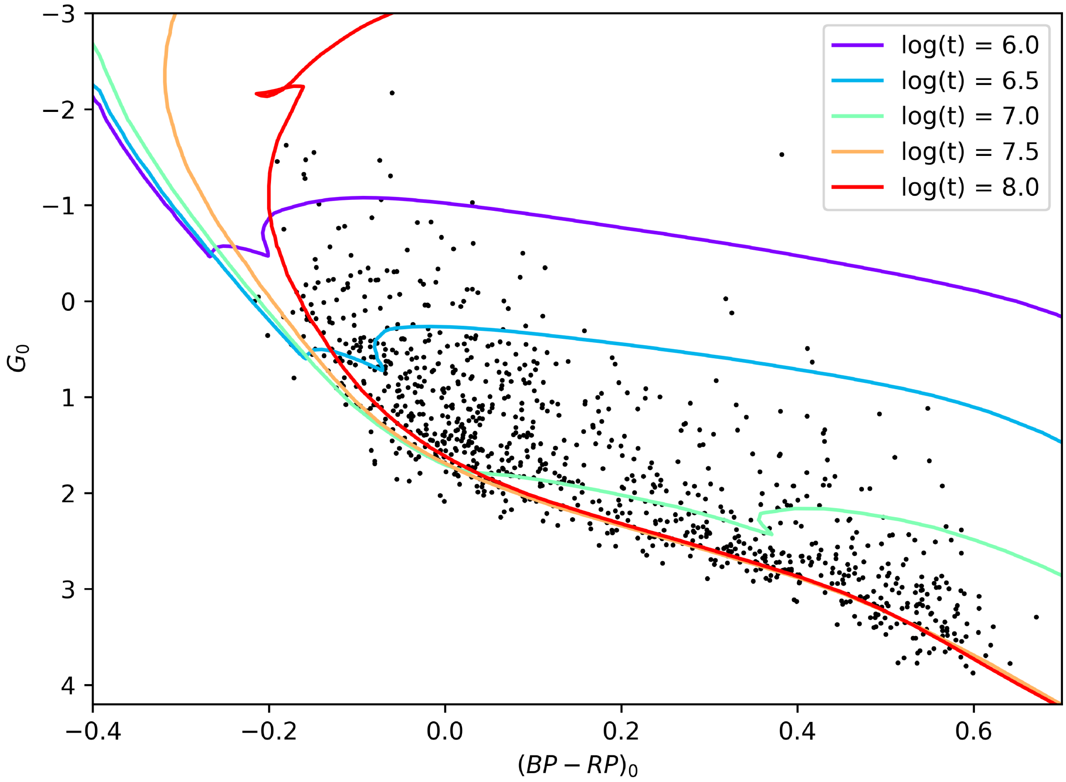

Figure 4.8.: Colour - absolute magnitude diagram of all the CP stars and candidates detected in this work. The isochrones used are from Bressan et al. (2012)

5. Summary and conclusion

This last chapter gives a summary of the work and the detected CP stars. I also give a conclusion of the findings.

5.1. Summary of the methodology

The goal of this work was to establish a study of CP stars in stellar associations. For this purpose, list of clusters and associations was compiled from the catalogues of Kerr et al. (2021); Hunt & Reffert (2023) and Ratzenböck et al. (2023a).
I downloaded the stars in the region of the clusters and associations in this catalogues and performed a membership analysis using HDBSCAN. After this, the photometry of the sources was corrected using the `starHorse2` catalogue (Anders et al., 2022) which left ~ 330 thousand stars with $T_{\rm eff} \gtrapprox 6500K$ to search for chemical peculiarities in them.

5.2. Detected stars

The analysis to find CP stars was done via three methods.

5.2.1. Δa photometry

By using synthetic photometry of three filters on the low-resolution *Gaia*BP/RP spectra the magnetic chemically peculiar (mCP) were identified. This gave me 341 single stars as CP candidates.

5.2.2. Spectroscopy

I used the spectroscopic data from LAMOST Data Release 9 to see which sources show peculiarities as described in Tab. 1.1 and Tab. 1.2. The automatic classification code MKCLASS detected 608 stars with peculiarities. Of special interest are several Lambda Boötis stars (see e.g. Fig. 4.3) and candidates that need special attention in further research.

5.2.3. Light curves

I also wanted to search for some stars that showed signs of photometric variability generally connected to CP stars. These stars are the ACV and SXARI variables and generally show double waves in their light curves (e.g. Fig. 3.7). From the downloaded TESS data, 20 stars showed signs of those variability types.

Alltogeter, 971 individual CP stars and candidates were detected in this work, most of them have not been named in the literature before. The lists of all the detected stars in the respective method can be seen in appendix B.

5.3. CP stars in the early stages of their evolution

A special interest was a poorly researched topic: When do the peculiarities form? So, I also looked at two signs that indicate that a star is still in their Pre-Main Sequence (PMS) phase.

5.3.1. IR excess

The IR excess was determined via the online-tool *Virtual Observatory SED Analyzer* (VOSA). Out of the 971 detected CP stars and candidates, 91 show excess in their SED. However, the excess is weak in most cases, suggesting the stars to either be in the late stages of PMS-evolution where the disk of debris around the star has almost dissolved entirely and thus is difficult to observe or that we are observing the star at an inclination angle where we look (almost) directly at the star's equator and thus on the thin edge of the disk.

5.3.2. Emission lines

The second clear sign of PMS-evolution is emission in at least one of the Balmer lines of hydrogen, mostly the Hα line. To detect this effect, I used two synthetic Hα filters, one narrow and one wide on the spectra from LAMOST. A quantity that compares the wide to the narrow synthetic magnitude together with a python routine that finds emission lines in spectra was used to discriminate between stars with and without hydrogen emission (Fig. 3.12. 12 stars that were classified as CP stars from those spectra also show emission lines.

Interestingly, the emission line stars with CP nature are almost all of the type magnetic chemically peculiar (mCP). This again strengthens the point made in Kueß et al. (2024) who propose the idea that the early evolution of CP stars is likely tied to the magnetic fields. However, this still is a small sample and much more follow-up investigation is needed to either confirm or disprove the CP nature of the candidates in this thesis, as well as to confirm the possible link of the magnetic field to the evolution of the peculiarities.

5.4. Caveats

While the analysis and classifications were performed carefully, one can still assume that a part of the data has been classified incorrectly. This is especially true for the clustering part that deviated from the papers the associations were taken from. While both Kerr et al. (2021) and Hunt & Reffert (2023) used an volume-limited all-sky approach for their respective clustering, I only used the clusters and associations bounded by their astrometric properties. This may lead to clusters not being detected in the surrounding field stars due to no significant difference in density compared to the surrounding region in the galaxy. I tried to overcome this issue with an iteration and scoring process to find the best hyper-parameters for HDBSCAN. While for nearby clusters and associations, this problem is likely negligible, it can become an issue for further away groups and/or for groups with extended tails. Nevertheless, I am confident to have identified at least the core of most of those aggregates. This is also accompanied by a cut in the membership probability, throwing out all the sources with low (less than 50 per cent) probabilities.
Another issue is simply the quality of data. For example, having spectra of low S/N may lead to incorrect estimations of the spectral type determined by MKCLASS. This was already pointed out in Kueß et al. (2024) who detected a new CP2 candidate with poor S/N in its spectrum, so the exact type has yet to be determined.
Last, but not least, the light curve data from TESS have a problem. As already mentioned above, the portion of the sky that falls on one picel of the instrument is relatively large. This means that one can never be entirely sure that the signal one receives from this pixel really comes from the star in question. Another issue may be ambiguity in the classification due to some classes showing similar light curve patterns although their origin is vastly different from each other.

Bibliography

Abril-Pla, O., Andreani, V., Carroll, C., et al. 2023, PeerJ Computer Science, 9, e1516, doi: 10.7717/peerj-cs.1516

Abt, H. A. 2009, Astronomical Journal, 138, 28, doi: 10.1088/0004-6256/138/1/28

Adelman, S. J., Adelman, A. S., & Pintado, O. I. 2003, Astronomy & Astrophysics, 397, 267, doi: 10.1051/0004-6361:20021475

Agarwal, M., Rao, K. K., Vaidya, K., & Bhattacharya, S. 2021, Monthly Notices of the Royal Astronomical Society, 502, 2582–2599, doi: 10.1093/mnras/stab118

Alacoria, J., Saffe, C., Jaque Arancibia, M., et al. 2022, Astronomy & Astrophysics, 660, A98, doi: 10.1051/0004-6361/202243058

Alfvén, H. 1943, Arkiv for Matematik, Astronomi och Fysik, 29B, 1

Alves, J., Zucker, C., Goodman, A. A., et al. 2020, Nature, 578, 237, doi: 10.1038/s41586-019-1874-z

Ambartsumian, V. A. 1947, The evolution of stars and astrophysics

Anders, F., Khalatyan, A., Queiroz, A. B. A., et al. 2022, Astronomy & Astrophysics, 658, A91, doi: 10.1051/0004-6361/202142369

Astropy Collaboration, Robitaille, T. P., Tollerud, E. J., et al. 2013, Astronomy & Astrophysics, 558, A33, doi: 10.1051/0004-6361/201322068

Astropy Collaboration, Price-Whelan, A. M., Sipőcz, B. M., et al. 2018, Astronomical Journal, 156, 123, doi: 10.3847/1538-3881/aabc4f

Astropy Collaboration, Price-Whelan, A. M., Lim, P. L., et al. 2022, Astrophysical Journal, 935, 167, doi: 10.3847/1538-4357/ac7c74

Babcock, H. W. 1947, Astrophysical Journal, 105, 105, doi: 10.1086/144887

Bagnulo, S., Landstreet, J. D., Lo Curto, G., Szeifert, T., & Wade, G. A. 2003, Astronomy & Astrophysics, 403, 645, doi: 10.1051/0004-6361:20030376

Balona, L. A. 2022, arXiv e-prints, arXiv:2212.10776, doi: 10.48550/arXiv.2212.10776

Balona, L. A., Krisciunas, K., & Cousins, A. W. J. 1994, Monthly Notices of the Royal Astronomical Society, 270, 905, doi: 10.1093/mnras/270.4.905

Balona, L. A., Cunha, M. S., Kurtz, D. W., et al. 2011, Monthly Notices of the Royal Astronomical Society, 410, 517, doi: `10.1111/j.1365-2966.2010.17461.x`

Baluev, R. V. 2008, Monthly Notices of the Royal Astronomical Society, 385, 1279, doi: `10.1111/j.1365-2966.2008.12689.x`

Bayo, A., Rodrigo, C., Barrado Y Navascués, D., et al. 2008, Astronomy & Astrophysics, 492, 277, doi: `10.1051/0004-6361:200810395`

Bessell, M., & Murphy, S. 2012, Publications of the Astronomical Society of the Pacific, 124, 140, doi: `10.1086/664083`

Blaauw, A. 1964, Annual Review of Astronomy and Astrophysics, 2, 213, doi: `10.1146/annurev.aa.02.090164.001241`

Braithwaite, J., & Spruit, H. C. 2004, Nature, 431, 819, doi: `10.1038/nature02934`

Bressan, A., Marigo, P., Girardi, L., et al. 2012, Monthly Notices of the Royal Astronomical Society, 427, 127, doi: `10.1111/j.1365-2966.2012.21948.x`

Brittain, S. D., Kamp, I., Meeus, G., Oudmaijer, R. D., & Waters, L. B. F. M. 2023, , 219, 7, doi: `10.1007/s11214-023-00949-z`

Burke, C. J., Pinsonneault, M. H., & Sills, A. 2004, Astrophysical Journal, 604, 272, doi: `10.1086/381242`

Bychkov, V. D., Bychkova, L. V., & Madej, J. 2021, Astronomy & Astrophysics, 652, A31, doi: `10.1051/0004-6361/202040215`

Campello, R., Moulavi, D., & Sander, J. 2013, in , 160–172, doi: `10.1007/978-3-642-37456-2_14`

Cantat-Gaudin, T., & Anders, F. 2020, Astronomy & Astrophysics, 633, A99, doi: `10.1051/0004-6361/201936691`

Cantat-Gaudin, T., & Casamiquela, L. 2024, arXiv e-prints, arXiv:2406.03308, doi: `10.48550/arXiv.2406.03308`

Cariddi, S., Azatyan, N. M., Kurfürst, P., et al. 2018, New Astronomy, 58, 1, doi: `10.1016/j.newast.2017.07.002`

Carraro, G. 2020, arXiv e-prints, arXiv:2007.11213, doi: `10.48550/arXiv.2007.11213`

Chambers, K. C., Magnier, E. A., Metcalfe, N., et al. 2016, arXiv e-prints, arXiv:1612.05560, doi: `10.48550/arXiv.1612.05560`

Chojnowski, S. D., Hubrig, S., Hasselquist, S., et al. 2020, Monthly Notices of the Royal Astronomical Society, 496, 832, doi: `10.1093/mnras/staa1527`

Crawford, D. L. 1958, Astrophysical Journal, 128, 185, doi: `10.1086/146536`

Cui, X.-Q., Zhao, Y.-H., Chu, Y.-Q., et al. 2012, Research in Astronomy and Astrophysics, 12, 1197, doi: 10.1088/1674-4527/12/9/003

Cutri, R. M., Wright, E. L., Conrow, T., et al. 2013, Explanatory Supplement to the AllWISE Data Release Products, Explanatory Supplement to the AllWISE Data Release Products, by R. M. Cutri et al.

De Angeli, F., Weiler, M., Montegriffo, P., et al. 2023, Astronomy & Astrophysics, 674, A2, doi: 10.1051/0004-6361/202243680

Deutsch, A. J. 1947, Astrophysical Journal, 105, 283, doi: 10.1086/144904

Dolk, L., Wahlgren, G. M., & Hubrig, S. 2003, Astronomy & Astrophysics, 402, 299, doi: 10.1051/0004-6361:20030213

Dotter, A. 2016, Astrophysical Journal, 222, 8, doi: 10.3847/0067-0049/222/1/8

Dotter, A., Chaboyer, B., Jevremović, D., et al. 2008, Astrophysical Journal, 178, 89, doi: 10.1086/589654

Earl, N., Tollerud, E., O'Steen, R., et al. 2024, astropy/specutils: v1.15.0, v1.15.0, Zenodo, doi: 10.5281/zenodo.11099077

Ester, M., Kriegel, H.-P., Sander, J., & Xu, X. 1996, in Second International Conference on Knowledge Discovery and Data Mining (KDD'96). Proceedings of a conference held August 2-4, 226–331

Feinstein, A. D., Montet, B. T., Foreman-Mackey, D., et al. 2019, Publications of the Astronomical Society of the Pacific, 131, 094502, doi: 10.1088/1538-3873/ab291c

Folsom, C. P., Bagnulo, S., Wade, G. A., et al. 2012, Monthly Notices of the Royal Astronomical Society, 422, 2072, doi: 10.1111/j.1365-2966.2012.20718.x

Gaia Collaboration, Prusti, T., de Bruijne, J. H. J., et al. 2016, Astronomy & Astrophysics, 595, A1, doi: 10.1051/0004-6361/201629272

Gaia Collaboration, Brown, A. G. A., Vallenari, A., et al. 2021, Astronomy & Astrophysics, 649, A1, doi: 10.1051/0004-6361/202039657

Gaia Collaboration, Vallenari, A., Brown, A. G. A., et al. 2022, arXiv e-prints, arXiv:2208.00211, doi: 10.48550/arXiv.2208.00211

Gaia Collaboration, Montegriffo, P., Bellazzini, M., et al. 2023, Astronomy & Astrophysics, 674, A33, doi: 10.1051/0004-6361/202243709

Galindo-Guil, F. J., Barrado, D., Bouy, H., et al. 2022, Astronomy & Astrophysics, 664, A70, doi: 10.1051/0004-6361/202141114

Gray, R. O., & Corbally, C. J. 2014, Astronomical Journal, 147, 80, doi: 10.1088/0004-6256/147/4/80

Gray, R. O., & Corbally, Christopher, J. 2009, Stellar Spectral Classification

Guzik, J. A., Kaye, A. B., Bradley, P. A., Cox, A. N., & Neuforge, C. 2000, Astrophysical Journall, 542, L57, doi: 10.1086/312908

Hauck, B., & North, P. 1982, Astronomy & Astrophysics, 114, 23

Holdsworth, D. L. 2021, Frontiers in Astronomy and Space Sciences, 8, 31, doi: 10.3389/fspas.2021.626398

Hümmerich, S., Paunzen, E., & Bernhard, K. 2020, Astronomy & Astrophysics, 640, A40, doi: 10.1051/0004-6361/202037750

Hunt, E. L., & Reffert, S. 2021, Astronomy & Astrophysics, 646, A104, doi: 10.1051/0004-6361/202039341

—. 2023, arXiv e-prints, arXiv:2303.13424, doi: 10.48550/arXiv.2303.13424

Kaye, A. B., Handler, G., Krisciunas, K., Poretti, E., & Zerbi, F. M. 1999, Publications of the Astronomical Society of the Pacific, 111, 840, doi: 10.1086/316399

Kerr, R. M. P., Rizzuto, A. C., Kraus, A. L., & Offner, S. S. R. 2021, Astrophysical Journal, 917, 23, doi: 10.3847/1538-4357/ac0251

Khan, S. A., & Shulyak, D. V. 2007, Astronomy & Astrophysics, 469, 1083, doi: 10.1051/0004-6361:20077192

Kodaira, K. 1969, Astrophysical Journall, 157, L59, doi: 10.1086/180385

Krone-Martins, A., & Moitinho, A. 2015, UPMASK: Unsupervised Photometric Membership Assignment in Stellar Clusters, Astrophysics Source Code Library, record ascl:1504.001

Kueß, L., Paunzen, E., Faltová, N., et al. 2024, Astronomy & Astrophysics, 687, A176, doi: 10.1051/0004-6361/202348926

Lada, C. J. 2005, Progress of Theoretical Physics Supplement, 158, 1, doi: 10.1143/PTPS.158.1

Lada, C. J., & Lada, E. A. 2003, Annual Review of Astronomy and Astrophysics, 41, 57, doi: 10.1146/annurev.astro.41.011802.094844

Lindegren, L. 2018. http://www.rssd.esa.int/doc_fetch.php?id=3757412

Lomb, N. R. 1976, Astrophysics and Space Science, 39, 447, doi: 10.1007/BF00648343

Luhman, K. L. 2007, Astrophysical Journal, 173, 104, doi: 10.1086/520114

Maitzen, H. M. 1976, Astronomy & Astrophysics, 51, 223

Maitzen, H. M., & Seggewiss, W. 1980, Astronomy & Astrophysics, 83, 328

Majewski, S. R., Schiavon, R. P., Frinchaboy, P. M., et al. 2017, Astronomical Journal, 154, 94, doi: 10.3847/1538-3881/aa784d

Mathys, G. 2017, Astronomy & Astrophysics, 601, A14, doi: 10.1051/0004-6361/201628429

Maury, A. C., & Pickering, E. C. 1897, Annals of Harvard College Observatory, 28, 1

McInnes, L., Healy, J., & Astels, S. 2017, The Journal of Open Source Software, 2, doi: 10.21105/joss.00205

Meingast, S., & Alves, J. 2019, Astronomy & Astrophysics, 621, L3, doi: 10.1051/0004-6361/201834622

Meingast, S., Alves, J., & Fürnkranz, V. 2019, Astronomy & Astrophysics, 622, L13, doi: 10.1051/0004-6361/201834950

Michaud, G., & Charland, Y. 1986, Astrophysical Journal, 311, 326, doi: 10.1086/164774

Michaud, G., Megessier, C., & Charland, Y. 1981, Astronomy & Astrophysics, 103, 244

Miret-Roig, N., Galli, P. A. B., Brandner, W., et al. 2020, Astronomy & Astrophysics, 642, A179, doi: 10.1051/0004-6361/202038765

Montegriffo, P., De Angeli, F., Andrae, R., et al. 2022, arXiv e-prints, arXiv:2206.06205, doi: 10.48550/arXiv.2206.06205

Morgan, W. W., Keenan, P. C., & Kellman, E. 1943, An atlas of stellar spectra, with an outline of spectral classification

Morris, S. L. 1985, Astrophysical Journal, 295, 143, doi: 10.1086/163359

Netopil, M., Fossati, L., Paunzen, E., et al. 2014, Monthly Notices of the Royal Astronomical Society, 442, 3761, doi: 10.1093/mnras/stu1130

North, P., Jaschek, C., Hauck, B., et al. 1997, in ESA Special Publication, Vol. 402, Hipparcos - Venice 1997, ed. R. M. Bonnet, E. Høg, P. L. Bernacca, L. Emiliani, A. Blaauw, C. Turon, J. Kovalevsky, L. Lindegren, H. Hassan, M. Bouffard, B. Strim, D. Heger, M. A. C. Perryman, & L. Woltjer, 239–244

Oke, J. B., & Gunn, J. E. 1983, Astrophysical Journal, 266, 713, doi: 10.1086/160817

Paegert, M., Stassun, K. G., Collins, K. A., et al. 2021, arXiv e-prints, arXiv:2108.04778, doi: 10.48550/arXiv.2108.04778

Palla, F., & Stahler, S. W. 1990, Astrophysical Journall, 360, L47, doi: 10.1086/185809

Paunzen, E. 2020, Contributions of the Astronomical Observatory Skalnate Pleso, 50, 570, doi: 10.31577/caosp.2020.50.2.570

Paunzen, E., Maitzen, H. M., Pintado, O. I., et al. 2006, Astronomy & Astrophysics, 459, 871, doi: 10.1051/0004-6361:20065333

Paunzen, E., Prišegen, M., Hümmerich, S., Bernhard, K., & Kueß, L. 2024, Contributions of the Astronomical Observatory Skalnaté Pleso

Paunzen, E., & Prišegen, M. 2022, Astronomy & Astrophysics, 667, L10, doi: 10.1051/0004-6361/202244839

Paunzen, E., Stütz, C., & Maitzen, H. M. 2005, Astronomy & Astrophysics, 441, 631, doi: 10.1051/0004-6361:20053001

Pedersen, H., & Thomsen, B. 1977, Astronomy & Astrophysicss, 30, 11

Potravnov, I., Mashonkina, L., & Ryabchikova, T. 2023a, Monthly Notices of the Royal Astronomical Society, 520, 1296, doi: 10.1093/mnras/stad193

Potravnov, I., Ryabchikova, T., Artemenko, S., & Eselevich, M. 2023b, Universe, 9, 210, doi: 10.3390/universe9050210

Preston, G. W. 1974, Annual Review of Astronomy and Astrophysics, 12, 257, doi: 10.1146/annurev.aa.12.090174.001353

Prim, R. C. 1957, The Bell System Technical Journal, 36, 1389, doi: 10.1002/j.1538-7305.1957.tb01515.x

Qin, L., Luo, A. L., Hou, W., et al. 2019, Astrophysical Journal, 242, 13, doi: 10.3847/1538-4365/ab17d8

Ratzenböck, S., Großschedl, J. E., Möller, T., et al. 2023a, Astronomy & Astrophysics, 677, A59, doi: 10.1051/0004-6361/202243690

Ratzenböck, S., Großschedl, J. E., Alves, J., et al. 2023b, Astronomy & Astrophysics, 678, A71, doi: 10.1051/0004-6361/202346901

Renson, P., & Manfroid, J. 2009, Astronomy & Astrophysics, 498, 961, doi: 10.1051/0004-6361/200810788

Richards, M. T., Agafonov, M. I., & Sharova, O. I. 2012, Astrophysical Journal, 760, 8, doi: 10.1088/0004-637X/760/1/8

Ricker, G. R., Winn, J. N., Vanderspek, R., et al. 2015, Journal of Astronomical Telescopes, Instruments, and Systems, 1, 014003, doi: 10.1117/1.JATIS.1.1.014003

Riello, M., De Angeli, F., Evans, D. W., et al. 2021, Astronomy & Astrophysics, 649, A3, doi: 10.1051/0004-6361/202039587

Sahoo, S. 2016, PhD thesis, doi: 10.13140/RG.2.2.32928.69124

Samus', N. N., Kazarovets, E. V., Durlevich, O. V., Kireeva, N. N., & Pastukhova, E. N. 2017, Astronomy Reports, 61, 80, doi: 10.1134/S1063772917010085

Scargle, J. D. 1982, Astrophysical Journal, 263, 835, doi: 10.1086/160554

Schleicher, D. R. G., Hidalgo, J. P., & Galli, D. 2023, arXiv e-prints, arXiv:2306.17131, doi: 10.48550/arXiv.2306.17131

Shang, L.-H., Luo, A. L., Wang, L., et al. 2022, Astrophysical Journal, 259, 63, doi: 10.3847/1538-4365/ac5831

Skarka, M., Žák, J., Fedurco, M., et al. 2022, Astronomy & Astrophysics, 666, A142, doi: 10.1051/0004-6361/202244037

Skrutskie, M. F., Cutri, R. M., Stiening, R., et al. 2006, Astronomical Journal, 131, 1163, doi: 10.1086/498708

Smith, K. C. 1996, Astrophysics and Space Science, 237, 77, doi: 10.1007/BF02424427

Stahler, S. W. 1983, Astrophysical Journal, 274, 822, doi: 10.1086/161495

Stibbs, D. W. N. 1950, Monthly Notices of the Royal Astronomical Society, 110, 395, doi: 10.1093/mnras/110.4.395

Stigler, C., Maitzen, H. M., Paunzen, E., & Netopil, M. 2014, Astronomy & Astrophysics, 562, A65, doi: 10.1051/0004-6361/201322300

Strömgren, B. 1956, Vistas in Astronomy, 2, 1336, doi: 10.1016/0083-6656(56)90060-5

—. 1966, Annual Review of Astronomy and Astrophysics, 4, 433, doi: 10.1146/annurev.aa.04.090166.002245

Taylor, M. B. 2005, in Astronomical Society of the Pacific Conference Series, Vol. 347, Astronomical Data Analysis Software and Systems XIV, ed. P. Shopbell, M. Britton, & R. Ebert, 29

van den Bergh, S. 1966, Astronomical Journal, 71, 990, doi: 10.1086/109995

VanderPlas, J. T. 2018, Astrophysical Journal, 236, 16, doi: 10.3847/1538-4365/aab766

Venn, K. A., & Lambert, D. L. 1990, Astrophysical Journal, 363, 234, doi: 10.1086/169334

Watson, C. L., Henden, A. A., & Price, A. 2006, Society for Astronomical Sciences Annual Symposium, 25, 47

Wright, N. J., Kounkel, M., Zari, E., Goodwin, S., & Jeffries, R. D. 2023, in Astronomical Society of the Pacific Conference Series, Vol. 534, Protostars and Planets VII, ed. S. Inutsuka, Y. Aikawa, T. Muto, K. Tomida, & M. Tamura, 129

Yang, H.-F., Wang, R., Cai, J.-H., et al. 2024, Astrophysical Journal, 272, 43, doi: 10.3847/1538-4365/ad4107

York, D. G., Adelman, J., Anderson, John E., J., et al. 2000, Astronomical Journal, 120, 1579, doi: 10.1086/301513

Zechmeister, M., & Kürster, M. 2009, Astronomy & Astrophysics, 496, 577, doi: 10.1051/0004-6361:200811296

Zhao, G., Zhao, Y.-H., Chu, Y.-Q., Jing, Y.-P., & Deng, L.-C. 2012, Research in Astronomy and Astrophysics, 12, 723, doi: 10.1088/1674-4527/12/7/002

Acronyms

G Gaia G Photometer. 11, 14

G_{BP} Gaia Blue Photometer. 11, 14, 15

G_{RP} Gaia Red Photometer. 11, 14, 15

***Gaia* EDR3** *Gaia* Early Data Release 3. 12

***Gaia* DR3** *Gaia* Data Release 3. xi, 11, 12

Hipparcos HIgh Precision Parallax COllecting Satellite. 6

2MASS *Two Micron All Sky Survey*. 25, 39

ACV α^2 Canum Venaticorum. xvii, 5, 36, 38, 45, 55

ADQL Astronomical Data Query Language. 23, 25

AllWISE *Wide-field Infrared Survey Explorer All Sky release*. 25

APOGEE Apache Point Observatory Galactic Evolution Experiment. 49

BJD Barycentric Julian Date. 33

CMD Colour-magnitude diagram. xvii, 7, 25, 46, 51, 52

CP chemically peculiar. vii, ix, xii, xiii, xv, xvii, 1–3, 8, 9, 13, 14, 29, 32, 37, 39, 40, 43, 45–48, 50, 51, 53, 55–57, 73, 86, 93–98

CVZ Continuous Viewing Zone. 12

DBSCAN Density-Based Spatial Clustering of Applications with Noise. 19

DFT Discrete Fourier Transform. 33, 34

DR data release. 48, 49

DSCT δ Scuti. 5, 35, 37, 38

FAP False Alarm Probability. 35, 36, 94

FFI Full-Frame Image. 12, 32

FFT Fast Fourier Transform. 34

FOV Field of View. 12

FWHM Full-Width-at-Half-Maximum. 42

GCVS General Catalog of Variable Stars. 5

GDOR γ Doradus. 5, 37

GMM Gaussian Mixture Models. 7

HDBSCAN *Hierarchical Density-Based Spatial Clustering of Applications with Noise*. ix, xi, 6, 19, 21, 23, 55, 57

HRD Hertzsprung-Russell diagram. vii, 5, 8

IAU International Astronomical Union. 6

ICRS International Celestial Reference System. 16

IR infrared. xiii, 46, 56, 95–97

ISM Interstellar Medium. 3, 4, 6

LAMOST *Large Sky Area Multi-Object Fiber Spectroscopic Telescope*. vii, ix, xi, xv, xvii, 11, 13, 29, 31, 41, 42, 44, 45, 47–50, 55, 56, 98

LC Long Cadence. 12

LDB Lithium Depletion Boundary. 7

LMC Large Magellanic Cloud. 4

MAST Mikulski Archive for Space Telescopes. 12, 13

MC molecular cloud. 8

mCP magnetic chemically peculiar. xvii, 1, 3–5, 9, 11, 27, 29, 38, 45, 49, 51, 55, 56

MHD magnetohydrodynamics. 71

MIST MESA Isochrones & Stellar Tracks. 7

MOS Multi-Object Spectroscopy. 13

Pan-STARRS1 *Panoramic Survey Telescope and Rapid Response System*. 25

PARSEC PAdova TRieste Stellar Evolution Code. 7

PMS Pre-Main Sequence. vii, xii, 8, 9, 39, 40, 42, 45, 47, 56

roAp rapidly oscillating Ap. 5, 35, 37, 38

ROTM rotationally modulated. 36, 38

S/N Signal-to-Noise Ratio. 26, 27, 29, 31, 57

SC Short Cadence. 12

SDSS Sloan Digital Sky Survey. 39, 49

SED Spectral Energy Distribution. vii, ix, xvii, 8, 39–41, 46, 52, 56

SF Star Formation. 6, 8

SigMA Significant Mode Analysis. 7

SPYGLASS *Stars with Photometrically Young Gaia Luminosities Around the Solar System*. 14

SXARI SX Arietis. 5, 38, 45, 55

TESS *Transiting Exoplanet Survey Telescope*. vii, ix, xi, 12, 32, 36, 37, 56, 57

TIC TESS Input Catalog. 11, 13, 32

UPMASK Unsupervised Photometric Membership Assignment in Stellar Clusters. 7

UV ultra-violet. 2

VOSA *Virtual Observatory SED Analyzer*. 39–41, 56

VSX Variable Star Index. 5, 35, 39, 94

WISE Wide-field Infrared Survey Explorer. 39

ZAMS Zero-Age main sequence. 8, 51

A. Frozen-in magnetic fields

A magnetic field is "frozen" into a star during its formation when the field lines get dragged along the collapsing gas. This is in accordance to the flux conservation that states that the number of field lines always stays constand and thus

$$\frac{d\Phi_M}{dt} = 0 \tag{A.1}$$

Which is known als *Alfvén's theorem* (Alfvén, 1943). However, the question as to why those magnetic fields can be sustained in stars without a convective envelope is still somewhat a mystery. An explanation comes from the equations of magnetohydrodynamics (MHD). In this framework, Ohm's law connecting the current $\vec{J}$ to the electric $\vec{E}$ and magnetic $\vec{B}$ field with conductivity λ

$$\vec{J} = \lambda \left(\vec{E} + \frac{1}{c} \vec{v} \times \vec{B} \right) \tag{A.2}$$

is combined with the law of Faraday

$$\vec{\nabla} \times \vec{E} = -\frac{\partial \vec{B}}{\partial t} \tag{A.3}$$

and Ampère's law

$$\vec{\nabla} \times \vec{B} = \frac{4\pi}{c} \vec{J} \tag{A.4}$$

to get the famous induction equation for particles mivong with a velocity $\vec{v}$ in a medium of conductivity λ:

$$\frac{\partial \vec{B}}{\partial t} = \frac{1}{c} \vec{\nabla} \times (\vec{v} \times \vec{B}) + \frac{c^2}{4\pi\lambda} \triangle \vec{B} \tag{A.5}$$

One can then use this equation with the following assumptions:

1. $\vec{v} = 0$
2. $\vec{B} = \begin{pmatrix} B_x(y,t) \\ 0 \\ 0 \end{pmatrix}$

The induction equation then simplifies to

$$\frac{\partial B_x}{\partial t} = \frac{c^2}{4\pi\lambda} \frac{\partial^2 B_x}{\partial y^2} \tag{A.6}$$

which always has solutions for the homogeneous case ($\vec{B} = 0$).
The introduction of a length scale L leads to an estimation of the time τ it takes to dissipate a magnetic field:

$$\frac{B}{\tau} \approx \frac{c^2}{4\pi\lambda} \frac{B}{L^2} \Rightarrow \tau \approx \frac{4\pi\lambda L^2}{c^2} \tag{A.7}$$

So, if the length scale L is large enough, τ becomes longer than the main-sequence lifetime of the star.
This, of course, is only a one-dimensional approach, however, the three-dimensional case is analogous.

B. List of CP stars detected in this work

B.1. CP stars Detected via spectroscopy

Table B.1.: Stars that were classified as peculiar in at least one library from MKCLASS. The columns are (1) Gaia DR3 ID, (2) right ascension α in degrees, (3) declination δ in degrees, (4) parallax ϖ and parallax error σ_{ϖ}, (5) open cluster/association the star is in, (6) classification from `libnor36`, (7) classification from `librl8` and (9) classification from `libr18_225`

Gaia DR3	LAMOST ID	α	δ	$\varpi \pm \sigma_{\varpi}$	System	libnor36	libr18	libr18_225
422486316486081280	J000940.81+575109.5	2.42	57.853	0.288 ± 0.021	UBC 1195	B9 V	B9 V	kA0hA3mG8
422850976388400896	J001115.46+575859.3	2.814	57.983	0.295 ± 0.013	UBC 1195	kB9hF0mG8 Eu	F0 mA3 IV-V metal-weak	kB9.5hF0mG8 Eu
419025466196922752	J002705.69+524904.1	6.774	52.818	0.566 ± 0.019	Theia 2936	kA8hA8mF4	kA7hA8mF5	kA7hA8mF4
423487627981131648	J010004.63+552553.8	15.019	55.432	0.767 ± 0.015	AT 21	A6 IV-V (Sr)	A7 V	A7 V
423486318006267008	J010036.07+552153.7	15.15	55.365	0.835 ± 0.012	AT 21	kA2hA3mA6 Si	A1 IV-V SrSi	kA2hA6mA7 SrSi
522537579650553856	J010816.40+613405.5	17.068	61.568	0.854 ± 0.023	NGC 381	F5 V (Sr)	F5 V (Sr)	F5 V (Sr)
426344193550526080	J011006.42+602835.7	17.527	60.477	0.361 ± 0.018	UBC 413	kB9.5hF0mA5 Eu	kB9.5hA9mA7 Eu	kA0hA9mA7 Eu
410923920922247168	J011920.73+551700.2	19.836	55.283	1.662 ± 0.015	Theia 714	A5 III Sr	kA6hA9mF0	A9 V
510674433300466816	J012534.95+610827.0	21.396	61.141	0.383 ± 0.016	COIN-Gaia 31	kB9.5hF0mK0 Eu	B9.5 III	kA0hF0mK0 Eu
506120805889910272	J015402.86+575513.7	28.512	57.92	0.419 ± 0.017	UBC 1577	kA1hF5mK2	A0 III-IV	A8 mA1 V metal-weak
504941442233879296	J015618.23+565650.4	29.076	56.947	0.455 ± 0.021	UBC 1577	B9 III-IV Si	B9.5 III-IV Si	F0 mA0 V metal-weak
504940239643050752	J015627.82+565457.6	29.116	56.916	0.41 ± 0.019	UBC 1577	kA2hF5mK0	A1 V	kA3hA3mK0
504942473026002432	J015707.89+565841.0	29.283	56.978	0.447 ± 0.017	UBC 1577	A2 V	A2 V	A2 V Eu
504868904521760768	J015803.44+563443.4	29.514	56.579	0.452 ± 0.014	UBC 1577	A1 V	kA1hA2mA4	kA2hA3mG2
504535791156850176	J015815.54+553501.6	29.565	55.584	0.763 ± 0.017	NGC 744	A1 V	A0 V	kA1hA3mK0
504523765248458624	J015831.44+553159.6	29.631	55.533	0.725 ± 0.02	NGC 744	kA6hA8mF0	kA6hA8mF1	kA6hA8mF0
505262671425427712	J015954.67+570441.4	29.978	57.078	0.448 ± 0.023	UBC 1577	A1 V	DZ	kA2hA3mK0
505103272298128896	J020240.75+571130.1	30.67	57.192	0.406 ± 0.019	UBC 1577	kB9.5hF4mK2	kB9.5hA1mA2	kB9.5hF1mK0
505086371610011904	J020337.90+570205.8	30.908	57.035	0.427 ± 0.016	UBC 1577	A3 mA0 V Lam Boo	A0 IV-V	A3 mA0 V Lam Boo
505036412548787072	J020523.60+565926.4	31.348	56.991	0.412 ± 0.015	UBC 1577	F0 mB8 V Lam Boo	F0 mA3 IV-V metal-weak	kB9hF0mG2 Eu
458378499188409856	J021851.84+571255.0	34.716	57.215	0.38 ± 0.014	NGC 869	kB9hF0mA1 Eu	F0 V Fe-0.9	F0 mA2 V metal-weak
458455121404670720	J022212.78+571021.1	35.553	57.173	0.404 ± 0.02	NGC 884	A0 IV	A0 IV-V	kA0hA3mK1
458406742891002496	J022246.66+570448.8	35.694	57.08	0.383 ± 0.019	NGC 884	kB9hA8mK0 Eu	B9.5 IV	kA0hA8mK0 Eu
450639616650222720	J023611.58+502045.3	39.048	50.346	1.377 ± 0.019	COIN-Gaia 8	A1 V	A3 mA0 metal weak	kA2hA3mK0
450567632995957888	J023759.19+495427.9	39.497	49.908	1.385 ± 0.02	COIN-Gaia 8	kA2hF5mK0	A2 V	kA3hF5mK0
436028657602103168	J030153.84+474751.2	45.474	47.798	0.414 ± 0.019	UBC 1246	kB9.5hF1mG2 Eu	B9 III	kA0hF1mG2 Eu
435058750911681280	J031436.47+471151.0	48.652	47.197	0.292 ± 0.018	NGC 1245	F0 V Eu	A9 V (Sr)	A9 V Eu
435065038743702528	J031439.44+471619.9	48.664	47.272	0.316 ± 0.02	NGC 1245	?	A9 V	F0 V Eu
435064660786649088	J031445.87+471246.9	48.691	47.213	0.292 ± 0.017	NGC 1245	A8 IV-Vn	kA7hA9mF1	kA7hA8mF0
435064798225554688	J031449.77+471438.3	48.707	47.244	0.316 ± 0.016	NGC 1245	A4 IV Eu	A7 V Eu	A6 IV Eu
435064111030776960	J031510.27+471343.4	48.793	47.229	0.287 ± 0.028	NGC 1245	A3 III-IV (Sr)	A7 IV-V	A9 Vn
242254404817419008	J032301.85+445302.4	50.758	44.885	0.92 ± 0.018	Teutsch 175	kB9hF1mK0 Eu	F2 mA1 IV-V metal-weak	kB9.5hF1mK0 Eu
236353566425278720	J032326.08+405730.5	50.859	40.958	0.876 ± 0.016	CWNU 405	A5 III (Sr)	kA5hA7mA9	F0 mA6 V Lam Boo
237904599374669312	J032551.88+415025.8	51.466	41.84	0.855 ± 0.024	CWNU 405	F4 V	kA8hF5mF5	F4 V
237648619323758080	J032713.83+405743.8	51.808	40.962	0.914 ± 0.016	CWNU 405	kA3hF2mF9	A3 V	kA3hA3mG2
237645733105734144	J032729.92+405625.7	51.875	40.94	0.8 ± 0.022	CWNU 405	A0 Vn	A0 V (Sr)	A0 Vn
462235620332140416	J032730.46+593619.7	51.877	59.605	0.988 ± 0.013	Theia 1722	kA2hF5mK0	A2 V	kA2hA3mK0
237676343335060736	J032734.56+411329.2	51.894	41.225	0.899 ± 0.018	CWNU 405	A1 V	A1 V	kA1hA3mK0
462223044667930752	J032737.50+593111.2	51.906	59.52	0.916 ± 0.018	Theia 1722	kA2hF1mF9	A2 V (Sr)	kA2hA3mG2 Sr
450203458427858944	J032924.79+591513.2	52.353	59.254	0.887 ± 0.019	Theia 1722	A4 III-IV	kA5hA8mA9	A7 V
237620543119968512	J032926.31+405929.0	52.36	40.991	0.901 ± 0.025	CWNU 405	A3 mA0 V Lam Boo	A0 IV-V	A3 mA0 IV-V metal-weak
237779358131374720	J032939.29+413443.2	52.414	41.579	0.852 ± 0.014	CWNU 405	kA3hF5mG9	A3 IV-Vn	kA3hF6mK0
450214178666053248	J033054.27+593107.3	52.726	59.519	1 ± 0.017	Theia 1722	B9.5 IV-V	A0 IV-V	kA0hA3mK1
222762365754292608	J033130.21+372726.4	52.876	37.457	1.468 ± 0.02	NGC 1342	A8 mA3 V Lam Boo	kA3hA5mA7	?
241670147525959424	J033143.49+443909.3	52.931	44.653	1.137 ± 0.019	ASCC 11	kA2hF5mK0	A1 IV-V	A1 IV-Vn
222859088418077440	J033218.11+373740.9	53.076	37.628	1.524 ± 0.02	NGC 1342	?	A2 IV-V	kA2hF5mG9
241679085357081984	J033226.56+445141.2	53.11	44.861	1.181 ± 0.02	ASCC 11	B9 III-IV	B9 III-IV	kB9.5hF0mK0 Eu
241681005202960512	J033257.53+445553.5	53.24	44.932	1.217 ± 0.014	ASCC 11	A3 IV	A3 III-IV (Sr)	A3 IV

Continued on next page

Table B.1.: (continued)

Gaia DR3	LAMOST ID	α	δ	$\varpi \pm \sigma_{\varpi}$	System	libnor36	libr18	libr18_225
222692439389927552	J033301.26+370630.6	53.255	37.109	1.589 ± 0.019	NGC 1342	A4 II-III Sr	A6 V Sr	F0 V
241676508376692480	J033313.78+444828.1	53.307	44.808	1.187 ± 0.019	ASCC 11	B9.5 IV-V	A0 IV	kA0hA3mK0
450299803136387840	J033332.60+593503.5	53.386	59.584	0.878 ± 0.013	Theia 1722	A0 V	A0 V Si	A1 Vn
445262321891690624	J033911.19+552122.1	54.797	55.356	1.136 ± 0.012	UPK 307	B9.5 V	A0 V	A3 mA0 V Lam Boo
248667100227222272	J034105.20+482733.9	55.272	48.459	0.358 ± 0.018	HSC 1189	F0 mA1 metal weak	B9 IV	kB9.5hF0mA2 Eu
216590390373910912	J034223.33+315742.6	55.597	31.962	3.245 ± 0.015	per	A0 V	A0 V	A3 mA0 V Lam Boo
216617641943232000	J034406.47+314324.9	56.027	31.724	3.139 ± 0.022	per	F6 V Sr	F6 V Sr	F6 V Sr
218287456510352384	J034508.62+342455.9	56.286	34.415	3.597 ± 0.023	HSC 1142	A9 V Eu	A8 V	A8 V
218025768444775936	J034631.66+335155.9	56.632	33.866	3.133 ± 0.021	per	kA3hF3mG2	A3 V	kA3hA3mG2
473271620397519744	J034735.15+590758.8	56.896	59.133	0.584 ± 0.012	Tombaugh 5	kA0hF0mA2 Eu	A0 II-III	kA0hF0mA4 Eu
473267192293775360	J034752.03+590134.2	56.967	59.026	0.555 ± 0.02	Tombaugh 5	kA2hF5mK0	A2 V	kA3hA3mK0 Eu
473220153810648704	J034816.80+590129.7	57.07	59.025	0.628 ± 0.014	Tombaugh 5	kA1hF2mG5	A1 III	kA1hF0mG9 Eu
246658979678062080	J035559.54+472529.4	58.998	47.425	0.358 ± 0.018	UBC 1259	kB9hF0mG2 Eu	F0 mA3 IV-V metal-weak	F0 mB9.5 IV-V metal-weak
468733768414112512	J035652.43+554710.8	59.219	55.786	0.214 ± 0.024	HSC 1181	kB9hF1mK0 Eu	B5 V	kB9hF2mK0 Eu
251771536947325440	J035724.30+523121.5	59.351	52.523	0.905 ± 0.015	UBC 51	A5 V Si	A5 V Si	A5 V Si
251761469543936512	J035817.76+523448.6	59.574	52.58	0.897 ± 0.015	UBC 51	kA3hF3mG2	A5 V	kA4hF6mK0
251870699153617920	J035839.53+524635.2	59.665	52.776	0.892 ± 0.012	UBC 51	A1 V	A3 mA0 V Lam Boo	A1 Vn
468711022266719360	J040010.72+554945.9	60.045	55.829	0.204 ± 0.019	HSC 1181	kA0hA9mA2 Eu	A0 III	kA1hA9mA4 Eu
247304045105027712	J040942.50+492758.6	62.427	49.466	0.732 ± 0.015	NGC 1513	B9.5 III	A0 III	kA0hF0mA4
247304874033861504	J041002.92+492950.0	62.512	49.497	0.745 ± 0.022	NGC 1513	kA0hF3mG7	A0 II-III	kA0hF0mK0 Eu
247304564803489280	J041005.22+492809.0	62.522	49.469	0.685 ± 0.018	NGC 1513	kA0hF0mA5 Eu	A1 II-III	kA1hF0mA5 Eu
271667474733308288	J041507.49+510621.7	63.781	51.106	0.991 ± 0.015	NGC 1528	B9 V Si	B9.5 V Si	B9.5 IV-Vn Si
271482000862614656	J041542.20+511054.9	63.926	51.182	0.989 ± 0.013	NGC 1528	kA3hF5mG8	kA3hF5mG8	kA4hA7mK0 Eu
234156536036476928	J041544.76+472918.1	63.937	47.488	3.808 ± 0.019	HSC 1142	A4 III-IV Sr	kA4hA7mA9 Sr	kA4hA9mA8
271670464030463360	J041551.56+511631.2	63.964	51.275	1.007 ± 0.022	NGC 1528	A2 III	kA2hA5mA5	A9 mA5 metal weak
3304135250100217600	J041658.70+115233.8	64.245	11.876	3.145 ± 0.021	taur ori 1	F0 V	kA7hF0mF1	A9 V
233807715973839616	J041912.07+462917.3	64.8	46.488	0.917 ± 0.016	UBC 54	kA2hF5mK0	A1 V	A1 Vn
233051419472603520	J041913.64+461450.8	64.807	46.247	0.883 ± 0.019	UBC 54	F0 V (Sr)Eu	F0 V (Sr)	F0 V (Sr)
270664548327712256	J042013.48+501629.2	65.056	50.275	1.423 ± 0.023	NGC 1545	B8 IV-V	B8 V	kB9hF0mA3
270663036500726912	J042017.42+501037.7	65.073	50.177	1.414 ± 0.026	NGC 1545	A9 mA0 V Lam Boo	B8 V	kB8hA9mK0 Eu
270718974153188864	J042017.93+502444.5	65.074	50.412	1.432 ± 0.018	NGC 1545	A8 mA0 V Lam Boo	B9 IV-V	A8 mB9.5 V metal-weak
270665059424816000	J042050.03+500935.0	65.208	50.16	1.425 ± 0.015	NGC 1545	kA6hF0mF1	kA7hF1mF2	kA6hF0mF1
270671759571697920	J042132.23+502137.0	65.384	50.36	1.395 ± 0.025	NGC 1545	A0 V	A0 V	kA1hA3mK0
3300745657614098048	J042209.63+103907.0	65.539	10.652	3.282 ± 0.02	taur ori 1	A3 mA0 V Lam Boo	A3 mA0 V Lam Boo	A3 mA0 V Lam Boo
172747089338840960	J042556.94+333435.4	66.487	33.576	1.654 ± 0.019	HSC 1326	kA2hF5mK0	A2 V	kA2hA3mK0
253688741629946624	J042608.25+445142.3	66.534	44.862	0.37 ± 0.035	UBC 428	A3 IV-V Eu	A4 IV-Vn	A4 IV-V Eu
253428535333057920	J042756.29+442830.8	66.985	44.475	0.302 ± 0.025	UBC 1264	kB9.5hA1mA2 Si	kB9.5hA2mA6 SrSi	kA0hF0mA6 SiEu
253361911799240576	J042802.09+440629.1	67.009	44.108	0.405 ± 0.027	UBC 1264	A0 IV-V	A0 IV-V	kA1hA3mK1
48058592395097856	J042806.66+193606.6	67.027	19.602	4.683 ± 0.022	taur ori 4	A6 V	kA6hA7mA9	A7 V
253455576447809280	J042816.70+443353.2	67.07	44.565	0.365 ± 0.029	UBC 1264	A0 V Si	A0 V Si	A1 Vn
253435613439960576	J042905.34+442149.9	67.272	44.364	0.261 ± 0.045	UBC 1264	A2 Vn	kA2hA3mA6	A3 V
253436747311206528	J042906.36+442429.2	67.277	44.408	0.35 ± 0.021	UBC 1264	A0 II-III Si	A0 II-III Si	F1 V Fe-5.9
178451463039306496	J042959.11+382916.8	67.496	38.488	0.574 ± 0.029	FSR 0728	A4 IV-V Sr	A5 IV-V Sr	A5 IV-V Sr
256885606046127360	J043037.81+461844.3	67.658	46.312	0.835 ± 0.025	FoF 2139	F0 V Fe-0.5	kA4hA9mF0 Sr	kA4hF0mF0 SrEu
256887152234319744	J043045.56+462300.7	67.69	46.384	0.909 ± 0.019	FoF 2139	A1 V	kA1hA2mA4	kA2hA3mG0
256882960346245120	J043105.63+461921.7	67.773	46.323	0.881 ± 0.023	FoF 2139	A5 II-III (Sr)	kA5hA7mA9	F1 mA6 IV-V metal-weak
253763645859881856	J043121.49+452310.0	67.84	45.386	0.357 ± 0.031	CWNU 1508	kA0hA2mA4	A0 IV	kA0hA3mA5
252600426975748736	J043152.87+434736.4	67.97	43.793	1.025 ± 0.017	NGC 1582	A1 V	kA1hA2mA3	kA1hA3mG2
252642109637707776	J043301.65+434222.8	68.257	43.706	1.027 ± 0.018	NGC 1582	A9 mB8 V Lam Boo	A9 mA4 V metal-weak	kB9hA9mG9 Eu
3293360242308046336	J043355.15+091111.0	68.479	9.186	3.329 ± 0.027	taur ori 1	F0 IV-V (Sr)	F0 IV-V SrSi	F0 IV-V SrSi
253967845783620992	J043554.41+453942.6	68.977	45.662	0.964 ± 0.019	HSC 1255	kB9.5hA9mG2 Eu	A0 III-IV	A9 mB9.5 V metal-weak
254108686349565824	J044046.33+462636.3	70.193	46.443	0.988 ± 0.014	HSC 1255	B9 IV-V	B9 V	kB9hA9mK0 Eu
203520431235145088	J044429.58+412357.1	71.123	41.399	0.304 ± 0.02	FSR 0723	kB9hF0mG1 Eu	B9 III	kB9.5hF1mG8 Eu
203559871917801088	J044502.66+414201.3	71.261	41.7	0.294 ± 0.024	FSR 0723	kB9.5hF0mK0 Eu	B9.5 III	kA0hF0mK0 Eu

Continued on next page

Table B.1.: (continued)

Gaia DR3	LAMOST ID	α	δ	$\varpi \pm \sigma_{\varpi}$	System	libnor36	libr18	libr18_225
203543074302648832	J044512.98+413146.4	71.304	41.53	0.356 ± 0.015	FSR 0723	kA2hA4mA8	kA2hA7mF1	kA2hA3mA9
203544105094762112	J044547.46+413335.0	71.448	41.56	0.91 ± 0.015	HSC 1284	A4 III-IV (Sr)	A8 Vn	A7 Vn
203356054246421248	J044553.53+413009.1	71.473	41.503	0.296 ± 0.021	FSR 0723	B8 IV Si	B8 IV Si	F1 V Fe-6.4
154335633988977280	J044557.03+264323.7	71.488	26.723	1.625 ± 0.018	HSC 1326	A5 III-IV (Sr)	kA5hA8mA9	A8 V
154303370194530688	J044754.06+263338.4	71.975	26.561	1.633 ± 0.016	HSC 1326	B6 V	B8 IV	kB9hF1mG8 Eu
153508212833673856	J044830.98+261257.8	72.129	26.216	1.656 ± 0.018	HSC 1326	kA2hA3mA5	kA1hA7mA7	kA2hA7mA5
161907042857052544	J045003.61+341605.8	72.515	34.268	1.602 ± 0.016	HSC 1326	A6 V (Sr)	kA6hA8mF1	kA6hA7mF0 Sr
153251412444365568	J045111.08+253720.9	72.796	25.622	1.638 ± 0.019	HSC 1326	B8 IV	B8 IV	kB9hF1mK0 Eu
206043638623627520	J045111.19+433831.8	72.797	43.642	0.759 ± 0.016	NGC 1664	A3 III-IV	kA3hA5mA7	A3 III-IV
200294769060243840	J045139.72+404156.4	72.916	40.699	0.876 ± 0.019	HSC 1284	A1 V	A1 V	kA2hA3mK0
206535189040348288	J045438.19+453508.0	73.659	45.586	0.322 ± 0.026	UBC 1607	kB9.5hF0mK0 Eu	B9.5 III-IV	kB9.5hF0mK0 Eu
200099468307337600	J045448.78+402634.5	73.703	40.443	0.912 ± 0.015	HSC 1284	kA2hF4mG8	A2 V	kA2hA3mG2
155085019883125760	J045508.39+290119.8	73.785	29.022	1.51 ± 0.017	HSC 1326	A2 V (Sr)Si	A1 V SrSi	kA2hA4mA5 Si
202029802706537984	J045738.60+421703.5	74.411	42.284	1.034 ± 0.021	CWNU 518	B8 IV	Unclassifiable	kB9hF1mG2 Eu
266844153439335168	J050216.02+530017.6	75.567	53.005	1.068 ± 0.015	NGC 1708	A0 V	A0 V (Sr)	kA1hA3mA5 Eu
3418726519450952832	J050230.93+234554.7	75.629	23.765	1.405 ± 0.019	Theia 754	B9 V	B9 V	kB9hA3mF9
266844638772744192	J050240.79+530235.0	75.67	53.043	1.079 ± 0.014	NGC 1708	kA2hF4mG9	kA1hA3mA4	kA2hA3mG9
3418577810501958784	J050244.44+232744.9	75.685	23.462	1.406 ± 0.019	Theia 754	F0 V Eu	F1 V	F0 V Si
3232081882311276800	J050246.46+021919.1	75.694	2.322	3.601 ± 0.018	taur ori 4	F0 V	kA7hA5mF0 Sr	F0 IV-V
3418678798070596736	J050256.84+234026.0	75.737	23.674	1.399 ± 0.023	Theia 754	B9.5 V	A0 IV-V	kA0hA3mK2
200852157034186496	J050302.72+403642.9	75.761	40.612	0.533 ± 0.023	Theia 5736	A4 IV (Sr)	kA5hA7mA9	kA4hA7mA8
3418672024905934720	J050302.98+233045.2	75.762	23.513	1.354 ± 0.019	Theia 754	F0 V Fe-0.5	kA6hF0mF0 Eu	kA6hF1mF0 Eu
3418674022066969984	J050304.58+233737.1	75.769	23.627	1.379 ± 0.019	Theia 754	A3 II-III (Sr)	A5 II-III	F0 V Fe-0.7
266840996640466816	J050322.92+525845.2	75.846	52.979	1.054 ± 0.02	NGC 1708	kB9hA9mK0 Eu	B9.5 III-IV	kB9.5hA9mG2 Eu
200840131126097280	J050335.03+402950.2	75.896	40.497	0.563 ± 0.025	Theia 5736	F5 V (Sr)	F5 V Sr	F5 V Sr
3418682813863743872	J050347.91+234738.6	75.95	23.794	1.393 ± 0.014	Theia 754	A2 V (Sr)Si	A0 V SrSi	A2 Vn Si
3418681718648535808	J050359.76+234444.2	75.999	23.746	1.419 ± 0.018	Theia 754	B9 III-IV	B9.5 III-IV	kB9.5hF0mA3 Eu
3418658281010587136	J050405.72+233059.2	76.024	23.516	1.388 ± 0.015	Theia 754	F1 V Fe-0.8	A6 II Sr	F1 V Fe-0.6 (Sr)
3418669310486586752	J050412.42+234006.5	76.052	23.668	1.403 ± 0.015	Theia 754	A1 V	A1 V Si	kA1hA3mG0
3418712264455591424	J050420.27+235815.8	76.085	23.971	1.438 ± 0.014	Theia 754	A2 V SrSi	A1 V SrSi	kA2hA5mA5 Si
3418671651245179008	J050421.38+234526.3	76.089	23.757	1.381 ± 0.021	Theia 754	B9.5 IV	A0 IV	kA0hA3mK2
3418670753595584512	J050434.33+234500.7	76.143	23.75	1.377 ± 0.016	Theia 754	kA3hF5mK0	A3 V	kA3hA3mK0
3418691098857073280	J050455.99+234511.9	76.233	23.753	1.427 ± 0.017	Theia 754	F0 mB5 V Lam Boo	F0 mB9 V Lam Boo	kB9hF0mG2 Eu
280808019831595008	J050629.28+575340.6	76.622	57.895	4.423 ± 0.016	HSC 1142	kA4hA9mA8 Eu	kA5hA7mF0 Sr	kA5hA9mF0
205757903037762304	J051109.90+454445.2	77.791	45.746	0.249 ± 0.03	FSR 0716	kA2hA3mA5 Sr	A1 IV-V Sr	kA2hA6mA6
188192208350840320	J051119.65+382641.7	77.832	38.445	0.953 ± 0.023	CWNU 154	F0 mB5 V Lam Boo	B8 IV-V	F0 V Fe-6.8
3394749576758590208	J051154.99+163742.8	77.979	16.629	0.599 ± 0.022	NGC 1817	F0 V	kA7hF0mF1	F0 V
3394737688289099904	J051206.77+163741.6	78.028	16.628	0.527 ± 0.016	NGC 1817	F1 V Fe-0.7	A9 V Eu	F0 V
3394755486633539584	J051216.61+164103.0	78.069	16.684	0.581 ± 0.018	NGC 1817	kA3hA6mA7 Sr	kA4hA7mF0	kA3hA7mA8
3394758922607329664	J051217.63+164738.6	78.073	16.794	0.583 ± 0.022	NGC 1817	F1 V (Sr)	kA8hF0mF5 Si	kA9hF1mF2 Sr
3394759094406004480	J051223.55+164856.5	78.098	16.816	0.543 ± 0.018	NGC 1817	kA2hA3mA5	A2 IV SrSi	kA2hA7mA7 Sr
3394744216639326208	J051233.07+164150.2	78.138	16.697	0.643 ± 0.019	NGC 1817	A4 II-III	F1 mA7 V Lam Boo	F0 V Fe-0.7
187001261160527872	J051331.57+363619.2	78.382	36.605	1.888 ± 0.015	Theia 943	F1 V	kA7hA9mF2	F2 V
187374652737209984	J051538.73+374601.2	78.911	37.767	0.626 ± 0.018	HSC 1323	A3 mA0 V Lam Boo	A0 V	A3 mA0 V Lam Boo
187370009872414592	J051648.19+375116.0	79.201	37.854	0.673 ± 0.016	HSC 1323	B9.5 V	A0 IV-V	kA0hA3mK0
187763772474021632	J051733.49+381506.8	79.39	38.252	0.654 ± 0.027	HSC 1323	B5 IV-V	B6 IV	kB7hF1mG2
187557206026094592	J051827.25+375749.9	79.614	37.964	0.65 ± 0.021	HSC 1323	A8 mA3 V Lam Boo	kA3hA5mA7	A8 mA3 V metal-weak
187537105579670272	J051851.20+373909.6	79.713	37.653	0.641 ± 0.026	HSC 1323	F0 mA3 V Lam Boo	kA2hA8mA6	F0 mA3 V metal-weak
3207628434471651328	J051942.18-064056.2	79.926	-6.682	1.539 ± 0.019	Theia 6046	kA4hF0mF1 Eu	kA5hF0mF2 Eu	kA5hF0mF1 Eu
187964609445409536	J051956.20+392118.6	79.984	39.355	0.322 ± 0.02	NGC 1857	B8 IV-V Si	B9 IV-V Si	kB9hF0mA5 Eu
187964540726357632	J051958.83+392044.4	79.995	39.346	0.309 ± 0.021	NGC 1857	kB9hA9mA2 Eu	B9.5 IV	kB9.5hA9mA3 Eu
187965502798572928	J052001.82+392327.6	80.008	39.391	0.312 ± 0.026	NGC 1857	A0 IV-V	A0 IV-V	kA1hA3mK0
3414738732512136192	J052002.54+222604.4	80.011	22.435	0.779 ± 0.022	CWNU 2136	A2 V Eu	A2 V	A2 V
187964502068579456	J052012.56+392205.8	80.052	39.368	0.355 ± 0.017	NGC 1857	kB9hA1mA4	B9.5 III-IV	kB9.5hF0mA7

Continued on next page

Table B.1.: (continued)

Gaia DR3	LAMOST ID	α	δ	$\varpi \pm \sigma_{\varpi}$	System	libnor36	libr18	libr18_225
3209945174191272960	J052022.99-055224.8	80.096	-5.874	1.38 ± 0.014	Theia 6046	A9 V SrSiEu	A9 V SrSiEu	A7 V SrSiEu
181248272728408320	J052053.21+334956.6	80.222	33.832	0.981 ± 0.024	HXWHB 8	A8 mA0 V Lam Boo	Unclassifiable	kB9hA8mG2 Eu
183576114939066752	J052117.64+345221.5	80.324	34.873	0.325 ± 0.03	UBC 1281	kB9hF0mK0 Eu	B9.5 III	kB9.5hF0mG2 Eu
3209981728655497984	J052129.64-053052.1	80.373	-5.515	0.848 ± 0.026	Theia 6046	B9.5 V	A0 V	kA0hA3mK0
3207584380990287744	J052152.07-065020.8	80.467	-6.839	1.048 ± 0.021	Theia 6046	kA4hF2mF2 Eu	kA5hA9mF3	kA5hF2mF2 Eu
3209200461221312128	J052205.49-054535.7	80.523	-5.76	1.432 ± 0.026	Theia 6046	A3 IV-V (Sr)	A2 IV-V SrSi	A4 IV-V (Sr)
3210104942677201920	J052208.90-050327.0	80.537	-5.058	1.251 ± 0.019	Theia 6046	A7 IV-V SiEu	A7 III Si	A7 IV-V Si
181197935711703168	J052211.82+334530.5	80.549	33.758	0.92 ± 0.016	HXWHB 8	A1 Vn	A4 mA1 V Lam Boo	A2 IV-Vn
187684268339361152	J052240.13+383901.1	80.667	38.65	0.725 ± 0.021	Theia 1424	A2 V	A1 V (Sr)Si	kA2hA3mA5
182807762470322560	J052256.56+344038.6	80.736	34.677	0.325 ± 0.016	UBC 1281	B4 V	B4 V	kB8hF2mK0
195239425050798208	J052323.41+421928.3	80.848	42.325	0.181 ± 0.03	SAI 47	kB9hF0mF9 Eu	F0 mA3 V Lam Boo	kB9.5hF0mG2 Eu
3447228235962784896	J052339.82+305448.4	80.916	30.913	1.124 ± 0.02	Theia 780	A9 mA4 V Lam Boo	A7 V	A7 Vn
182707943131604224	J052351.17+340638.1	80.963	34.111	0.375 ± 0.016	Gulliver 53	B9 II-III Si	B9.5 III Si	F0 V Fe-6.6
3414446056260128640	J052357.94+214153.2	80.991	21.698	0.719 ± 0.021	CWNU 2136	kA3hA6mA8 SiEu	kA4hA5mF0 SrSi	kA4hA7mF0 SiEu
182694650212152320	J052400.88+335938.9	81.004	33.994	0.38 ± 0.016	Gulliver 53	kA0hF4mK1	A0 III	F0 mA1 V metal-weak
182694783351830912	J052405.96+340124.2	81.025	34.023	0.411 ± 0.016	Gulliver 53	B9 III	B9.5 II-III	kA0hF1mG2
3207277170569274752	J052406.38-073138.5	81.027	-7.527	0.922 ± 0.015	Theia 6046	A4 II-III	kA5hA9mA9	kA5hF0mA9
194168363286342272	J052418.89+405942.4	81.079	40.995	0.224 ± 0.03	HSC 1309	A0 III (Sr)	A0 III	A9 mA0 V metal-weak
3209214097740534272	J052423.76-054019.9	81.099	-5.672	1.224 ± 0.014	Theia 6046	F5 V	F6 V (Sr)	F6 V
3210579420602206592	J052439.53-041818.6	81.165	-4.305	1.481 ± 0.012	Theia 6046	F4 V	F5 V (Sr)	F4 V (Sr)
194148159760231552	J052505.23+404400.8	81.272	40.734	0.189 ± 0.023	HSC 1309	B7 II-III	Unclassifiable	kB9.5hF2mF9 Eu
3208944309372058112	J052505.56-061407.6	81.273	-6.235	1.412 ± 0.022	Theia 6046	F1 V (Sr)	kA9hF0mF3	F1 V (Sr)
184532380818623488	J052527.01+373833.0	81.363	37.643	0.725 ± 0.022	Theia 1424	F0 V Fe-0.6	kA4hA7mA9	kA4hF0mA9 Sr
209193086599072896	J052557.27+462913.5	81.489	46.487	0.223 ± 0.028	NGC 1883	kA0hA8mF9 Eu	A0 III-IV	kA1hA8mG1 Eu
195368170990468224	J052641.19+421544.2	81.672	42.262	0.197 ± 0.023	HSC 1300	kB9hF0mG2 Eu	F0 mA3 IV-V metal-weak	kB9.5hF0mG2 Eu
3210561587897894528	J052642.08-041134.6	81.676	-4.192	3.007 ± 0.023	greater ori	kA2hF3mG2	A2 V	kA2hA3mG2
3210622881373361280	J052647.82-035453.1	81.699	-3.915	0.891 ± 0.022	Theia 6046	F2 V	F3 V	kA8hF2mF3
3446192839605007872	J052702.72+300209.5	81.761	30.036	1.086 ± 0.029	Theia 780	A9 mB9 V Lam Boo	A9 mB7 V Lam Boo	kB9hA9mK0 Eu
195365387851621888	J052709.65+421554.3	81.79	42.265	0.257 ± 0.025	HSC 1300	kB9.5hA9mF8 Eu	B9.5 IV	kA0hA8mG0 Eu
3210516473561593216	J052724.09-042557.6	81.85	-4.433	0.301 ± 0.015	Theia 6046	A2 IV-V	kA1hA5mA7	kA2hA3mA5
3208827623700834944	J052724.28-065002.0	81.851	-6.834	1.521 ± 0.02	Theia 6046	kA2hA4mA7 Si	A1 IV-V SrSi	kA2hA7mA9 Si
3015075223705487104	J052726.49-074542.1	81.86	-7.762	1.243 ± 0.025	Theia 6046	F1 IV	kA8hF1mF1 Sr	F1 IV
182439185558627200	J052728.53+332655.3	81.869	33.449	0.375 ± 0.025	HXWHB 10	A1 V	kA1hA2mA4	kA2hA3mG9
3210620789727012992	J052728.58-035351.9	81.869	-3.898	1.002 ± 0.015	Theia 6046	A5 II (Sr)	kA7hF3mF1	F1 V
3210559320155312768	J052731.99-041046.5	81.883	-4.18	0.6 ± 0.017	Theia 6046	A3 IV	A3 IV (Sr)	kA2hA6mA6
3208826524189207552	J052734.80-065224.2	81.895	-6.873	1.569 ± 0.017	Theia 6046	kA2hA8mA8 Eu	kA2hA8mF2 Sr	kA2hA8mF0 Eu
183337177320364928	J052741.67+354343.8	81.924	35.729	0.488 ± 0.024	UBC 198	kA2hF5mK0	A1 V	A1 Vn
3209032476461217024	J052742.72-060700.8	81.928	-6.117	0.548 ± 0.019	Theia 6046	A6 III-IV (Sr)	A8 V	A7 IV
3208878132516164224	J052748.14-062755.0	81.951	-6.465	0.804 ± 0.019	Theia 6046	A5 III Sr	kA5hA7mA9	kA5hA9mA8 SrEu
183340265399482496	J052750.53+354933.8	81.961	35.826	0.882 ± 0.014	NGC 1912	A1 IV-V	A0 IV-V	kA1hA3mK0
183263441322427648	J052756.27+351837.7	81.984	35.31	0.631 ± 0.031	NGC 1907	kA6hF1mF4 Eu	kA7hF2mF5	kA6hF1mF5 Eu
183337761435870464	J052756.95+354720.7	81.987	35.789	0.904 ± 0.017	NGC 1912	kA2hA6mA6	A2 IV	kA3hA7mA7
183262612388074496	J052800.13+351644.0	82.001	35.279	0.604 ± 0.02	NGC 1907	kA2hA7mF1 SiEu	A1 IV SrSi	kA2hA3mF3 SiEu
3209039447191403392	J052800.98-060040.7	82.004	-6.011	1.113 ± 0.016	Theia 6046	A4 II-III Sr	kA4hA5mA9	F0 V
183262410530287104	J052802.02+351603.2	82.008	35.268	0.65 ± 0.024	NGC 1907	?	F0 V Sr	A9 V SrSi
182635620182511744	J052805.13+342130.3	82.021	34.358	0.461 ± 0.015	Stock 8	B6 V	B7 V	kB9hF1mK0 Eu
182621906350208384	J052809.16+341653.2	82.038	34.281	0.476 ± 0.014	Stock 8	kB9hF0mK0 Eu	B9 III	kB9.5hF0mK0 Eu
3220111877176803584	J052813.56-015651.6	82.056	-1.947	2.812 ± 0.025	ASCC 19	A1 V	A1 V	kA2hA3mK0
182636268718056576	J052815.47+342525.6	82.064	34.424	0.489 ± 0.02	Stock 8	B4 IV-V	B4 V	kB7hF2mF9
183327895890995840	J052815.63+354905.5	82.065	35.818	0.81 ± 0.023	NGC 1912	B9.5 IV	A0 III-IV	kA0hA3mK2
3209746162586852352	J052815.71-044306.9	82.065	-4.719	0.808 ± 0.012	Theia 6046	F0 V Fe-0.6	kA7hF1mF0	F0 V
183363733100785024	J052815.96+355600.5	82.067	35.934	0.877 ± 0.016	NGC 1912	A1 V	kA1hA2mA3	kA1hA3mG9
183324459917174272	J052816.72+354059.8	82.07	35.683	0.851 ± 0.022	NGC 1912	kB9.5hA9mG2 Eu	A0 III-IV	A8 mA2 V metal-weak
183264472114526080	J052818.04+352025.1	82.075	35.34	0.626 ± 0.027	NGC 1907	A4 III (Sr)	kA5hA7mA9	A8 Vn

Continued on next page

Table B.1.: (continued)

Gaia DR3	LAMOST ID	α	δ	$\varpi \pm \sigma_{\varpi}$	System	libnor36	libr18	libr18_225
182659976937528320	J052819.83+342720.1	82.083	34.456	0.803 ± 0.016	COIN-Gaia 19	kA2hF5mK0	A2 V	kA2hA3mK0 Eu
3015083710562928640	J052819.88-073803.4	82.083	-7.634	1.34 ± 0.022	Theia 6046	A3 mA0 V Lam Boo	A3 mA0 V Lam Boo	A3 mA0 V Lam Boo
183351333532453760	J052829.60+355055.0	82.123	35.849	0.855 ± 0.016	NGC 1912	A3 III (Sr)	A7 V	A9 mA6 metal weak
3209038351976178048	J052831.10-055818.3	82.13	-5.972	0.363 ± 0.015	Theia 6046	kA2hF5mK0	A2 IV-V Eu	kA2hF5mK0
3209770313185631744	J052831.76-043845.6	82.132	-4.646	1.033 ± 0.011	Theia 6046	F1 V	kA7hF2mF2	F1 V
183363904896795136	J052832.47+355605.2	82.135	35.935	0.867 ± 0.02	NGC 1912	kA2hF5mK0	A2 IV-V	kA2hA3mK0
3221909265153557120	J052834.33+004557.5	82.142	0.766	2.748 ± 0.024	ASCC 20	kA3hF5mK0	A3 V	kA3hA3mK0
183322814949673216	J052836.34+354048.9	82.151	35.68	0.918 ± 0.023	NGC 1912	kA3hA5mA7	kA5hA8mF0	kA6hA9mF0
183364145417644160	J052837.05+355837.0	82.154	35.977	0.873 ± 0.018	NGC 1912	kA4hF0mA9	kA5hA7mF0	kA5hF0mF0
3015067316671384960	J052837.54-074530.9	82.156	-7.759	1.5 ± 0.021	Theia 6046	F0 V	kA6hA8mF0 Sr	kA7hF1mF0 Sr
183321951657541888	J052838.12+353901.8	82.159	35.651	0.514 ± 0.028	UBC 198	kA2hF5mK0	A2 V	kA2hA3mK0
183323227266520704	J052841.03+354132.9	82.171	35.693	0.824 ± 0.02	NGC 1912	kA2hF5mK0	A2 V	kA2hA3mK0
183350161001462656	J052841.61+354717.6	82.173	35.788	0.891 ± 0.02	NGC 1912	A2 IV-V (Sr)	A1 IV-V SrSi	A2 IV-V (Sr)
183347210363857792	J052846.36+354647.8	82.193	35.78	0.515 ± 0.023	UBC 198	A3 mA0 V Lam Boo	A0 V	A3 mA0 IV-V metal-weak
3210678681589101440	J052848.45-034010.4	82.202	-3.67	1.624 ± 0.014	Theia 6046	A3 IV Si	kA3hA6mA7	A5 IV Si
183350337100021888	J052850.59+354909.7	82.211	35.819	0.508 ± 0.031	UBC 198	A2 V (Sr)	A3 V SrSi	A3 V (Sr)
183346931186059776	J052850.69+354524.3	82.211	35.757	0.869 ± 0.021	NGC 1912	A1 V (Sr)Si	A0 V SrSi	kA1hA3mA5
183351024294768384	J052851.20+355201.1	82.213	35.867	0.888 ± 0.025	NGC 1912	kB9.5hA1mA2	A0 IV	A3 mA1 metal weak
183347691400163456	J052856.49+354843.5	82.235	35.812	0.875 ± 0.017	NGC 1912	A3 III-IV Sr	A7 V	A7 V
182618646471746176	J052856.71+341332.8	82.236	34.226	0.778 ± 0.017	COIN-Gaia 19	A0 IV-V SrSiEu	A0 IV-V SrSi	kA1hA3mA4 Eu
183322363973132672	J052900.07+354143.9	82.25	35.696	0.858 ± 0.019	NGC 1912	A1 V (Sr)	A0 V (Sr)	A2 V
183348271215846912	J052921.27+354928.8	82.339	35.825	0.87 ± 0.024	NGC 1912	A1 IV-V	A0 IV-V	kA1hA3mK0
3209071302965221504	J052929.31-054435.0	82.372	-5.743	1.986 ± 0.026	Theia 6046	F5 V	F6 V (Sr)	F5 V
3016701607563276672	J052931.81-064646.2	82.383	-6.78	0.426 ± 0.015	Theia 6046	A2 IV-V	A2 IV-V	kA2hA3mF9
3210661849614262528	J052943.33-034528.6	82.431	-3.758	1.34 ± 0.015	Theia 6046	F1 V	kA7hA8mF0	F1 V
3016683530043334016	J052947.51-065515.1	82.448	-6.921	1.819 ± 0.024	Theia 6046	F5 V (Sr)	F5 V Sr	F5 V (Sr)
3209453589413875456	J052958.17-053308.8	82.492	-5.552	0.929 ± 0.015	Theia 6046	F5 IV-V Fe-0.6 (Sr)	F6 IV (Sr)	F5 V Sr
3016633884518966528	J053021.07-070246.7	82.588	-7.046	1.211 ± 0.016	Theia 6046	kA7hF1mF1	kA6hF1mF1 Sr	kA7hF2mF2
3210681537744333440	J053022.58-034544.8	82.594	-3.762	1.724 ± 0.022	Theia 6046	A0 IV-V	A0 IV-V	kA1hA3mG8
190600929089387008	J053040.79+383328.5	82.67	38.558	0.235 ± 0.035	HSC 1329	kB9.5hA0mA1	B9.5 II	F2 V Fe-1.1
3209400744136460672	J053059.62-053916.1	82.748	-5.654	1.46 ± 0.013	Theia 6046	F1 IV-V Sr Sr	F2 IV-V Sr Sr	F1 IV-V Sr Sr
3209504544905800576	J053121.65-050351.8	82.84	-5.064	1.435 ± 0.017	Theia 6046	F3 V (Sr)	F4 V Sr	F3 V (Sr)
3016614436907212288	J053135.99-071012.5	82.9	-7.17	1.032 ± 0.015	Theia 6046	F2 V Fe-0.6 (Sr)	F0 IV-V SrSi	F1 IV-V Sr
3445922565903077504	J053144.53+292101.0	82.936	29.35	0.533 ± 0.02	CWNU 195	kB9hA9mG2 Eu	A9 mA4 V Lam Boo	kB9.5hA9mK0 Eu
3016813757749621248	J053156.20-063302.0	82.984	-6.551	1.018 ± 0.013	Theia 6046	F1 V Fe-0.6	A7 III (Sr)	F0 IV-V
3209829691110274688	J053203.50-042045.8	83.015	-4.346	0.519 ± 0.031	Theia 6046	A2 Vn	A1 V Si	A3 Vn
3404048142299274112	J053207.90+223153.8	83.033	22.532	0.749 ± 0.026	CWNU 2136	B9.5 III-IV	A0 III-IV	kA0hA3mK2
3016737062520757760	J053213.78-064530.2	83.057	-6.758	1.355 ± 0.016	Theia 6046	A5 III Sr	A8 V (Sr)	A8 Vn
195557660649524096	J053228.51+431240.2	83.119	43.211	0.799 ± 0.014	HSC 1303	A3 III-IV Sr	kA3hA5mA8	A9 mA7 metal weak
3017219992936576768	J053235.61-060139.7	83.148	-6.028	0.379 ± 0.015	Theia 6046	A0 III	A0 III	kA0hA9mF6 Eu
3215949675909917056	J053308.55-033049.0	83.286	-3.514	0.928 ± 0.019	Theia 6046	kA4hA8mA8 Eu	kA5hA8mF0	kA5hA7mA9
194674035554966912	J053339.65+422818.4	83.415	42.472	0.779 ± 0.018	HSC 1303	A8 V	kA6hA8mF0	kA7hA9mF0
183430257850893184	J053344.18+362631.3	83.434	36.442	0.915 ± 0.019	HSC 1350	A5 III (Sr)	kA6hA9mF0 Eu	F0 V Eu
3016551657368347520	J053354.61-065543.6	83.478	-6.929	1.016 ± 0.014	Theia 6046	kA9hF2mF4 Eu	kA8hF2mF6 Eu	kA8hF3mF5 Eu
194768073861273728	J053436.23+425846.6	83.651	42.98	0.783 ± 0.019	HSC 1303	A0 IV	A0 IV	kA1hA3mK0
3220898092414023680	J053455.47+001929.9	83.731	0.325	3.011 ± 0.02	greater ori	F5 V	F5 V (Sr)	F5 V (Sr)
3449524565999149056	J053618.57+341046.0	84.077	34.179	0.831 ± 0.025	NGC 1960	kA2hF3mG2	A2 V	A2 Vn
190969467344302592	J053632.47+395422.8	84.135	39.906	0.736 ± 0.029	Theia 7082	B9.5 V	A0 V	kA0hA3mK0
3017409624342379520	J053727.74-045428.2	84.366	-4.908	1.241 ± 0.021	Theia 6046	kA3hF2mF9	A3 IV (Sr)	A2 IV-V (Sr)
3222438405125088128	J053746.55+004912.0	84.444	0.82	1.444 ± 0.016	HSC 1608	F1 V Fe-0.6	kA8hF2mF1	F1 V
3023399317003378304	J053840.34-045326.7	84.668	-4.891	1.64 ± 0.018	Theia 6046	F1 V (Sr)	kA7hA8mF1	kA7hF1mF1 Eu
3023427285830158336	J053844.60-043415.1	84.686	-4.571	1.063 ± 0.025	Theia 6046	A4 II-III (Sr)	kA5hA7mA9	F0 V
3447997138187192704	J053849.83+322056.9	84.708	32.349	0.594 ± 0.021	HSC 1379	A3 mA0 V Lam Boo	A0 V	A3 mA0 V Lam Boo
3444537623633326848	J053931.33+302145.4	84.881	30.363	0.473 ± 0.023	Theia 1798	kB9hF1mF6 Eu	B9 III	kB9.5hF1mF8

Continued on next page

Table B.1.: (continued)

Gaia DR3	LAMOST ID	α	δ	$\varpi \pm \sigma_{\varpi}$	System	libnor36	libr18	libr18_225
3023355851934210176	J054026.06-045400.2	85.109	-4.9	0.685 ± 0.023	Theia 6046	kA2hA3mA5 Eu	A4 mA0 metal weak	kA2hA3mA6
3340278774287597696	J054034.50+114632.1	85.145	11.776	3.427 ± 0.019	taur ori 4	kA4hA8mA8	kA5hA9mF2	A9 mA5 V Lam Boo
3215713963807357696	J054041.17-040207.3	85.172	-4.035	1.484 ± 0.014	Theia 6046	A4 IV-V	kA5hA4mA9	A5 IV-V
3455880567838460544	J054129.40+360754.2	85.373	36.132	0.566 ± 0.016	OC 0292	B9 V	B9.5 IV	kB9.5hA3mA2
3455887611584791296	J054132.66+362148.9	85.386	36.364	0.612 ± 0.018	OC 0292	B5 V	B5 V	kB9hF1mG2 Eu
3340482798115881600	J054133.65+123436.2	85.389	12.577	3.407 ± 0.02	taur ori 4	A7 IV	kA6hA7mF1	kA6hA7mA9
3441644469239015168	J054156.16+271801.5	85.484	27.3	0.773 ± 0.018	Theia 1806	B9 III-IV Si	B9 III Si	kB9hF0mA6
3455831880089411072	J054212.83+360304.8	85.554	36.051	0.533 ± 0.017	OC 0292	A9 mA0 V Lam Boo	B9 V	kB9hA9mK0 Eu
3444662212044370944	J054309.05+305252.4	85.788	30.881	0.531 ± 0.024	Theia 1798	B9.5 V	A0 IV-V	kA0hA3mK1
3022320657439396224	J054529.21-054554.5	86.372	-5.765	1.371 ± 0.014	Theia 6046	A2 IV-V	A5 mA0 metal weak	kA2hA6mA6
3022003968028180352	J054649.85-063934.5	86.708	-6.66	0.784 ± 0.016	Theia 6046	A5 III-IV	A7 V	A7 V Eu
3445205168927696512	J054655.64+320853.8	86.732	32.148	0.395 ± 0.025	UBC 1285	kA2hA7mF1	kA2hA7mF3 SrSi	kA2hA7mF2 Si
3444694166601774080	J054855.77+300913.8	87.232	30.154	0.325 ± 0.012	Basel 4	kB9hA1mA2 Eu	B9.5 III	kB9.5hF0mA5 Eu
3429171025217951360	J054956.95+260720.3	87.487	26.122	0.927 ± 0.015	CWNU 15	B9.5 V	A0 V	A3 mA0 V Lam Boo
3346213731895890816	J055037.81+123122.4	87.658	12.523	3.603 ± 0.023	taur ori 4	A5 IV Sr	kA5hA7mF0	kA5hA7mA9 Sr
3429076913894849664	J055121.21+253127.2	87.838	25.524	0.943 ± 0.031	CWNU 15	B8 IV Si	B7 V Si	?
3451180082612344192	J055216.51+322728.4	88.069	32.458	0.659 ± 0.015	NGC 2099	kA2hF2mG0	kA1hA2mA4	kA2hA3mG0
3218833106497814144	J055345.91+002435.6	88.441	0.41	0.807 ± 0.029	NGC 2112	A1 III-IV	A1 III-IV	kA1hA3mG8
3342878432093211392	J055408.30+112307.6	88.535	11.385	0.555 ± 0.017	Theia 2999	A1 V	A0 V	kA1hA3mK0
3349994986744757504	J055415.47+171631.5	88.564	17.275	0.568 ± 0.027	UBC 76	B9.5 IV	B9 IV	kB9.5hA9mA2 Eu
3349789579929483520	J055504.49+170520.7	88.769	17.089	0.57 ± 0.016	UBC 76	A0 IV-V Eu	A0 IV-V	kA1hA3mK0
3343027622077611392	J055508.01+115959.2	88.783	12	0.639 ± 0.025	Theia 2999	F0 mB8 V Lam Boo	B9 IV	F0 mA1 V metal-weak
3343275596309771264	J055512.12+123940.8	88.8	12.661	0.598 ± 0.021	Theia 2999	A0 V	A0 V	kA1hA3mK0
3343035284299136384	J055559.50+120632.1	88.998	12.109	0.522 ± 0.023	Theia 2999	B9 V	A0 IV-V	kA0hA3mG2
3343012022756326912	J055614.31+115454.1	89.06	11.915	0.628 ± 0.019	Theia 2999	kB9.5hA9mK0 Eu	A0 III-IV	A8 mA0 V metal-weak
3398995130455135488	J055625.10+195750.4	89.105	19.964	0.324 ± 0.015	UBC 1304	B2 V	Unclassifiable	kB7hF4mK0
3349818790006231424	J055648.59+171449.6	89.202	17.247	0.59 ± 0.018	UBC 76	B9 V	Unclassifiable	kB9hA9mK0
3342843007203203968	J055649.52+112053.4	89.206	11.348	0.571 ± 0.02	Theia 2999	A4 III (Sr)	A7 V	F0 mA7 metal weak
3343051738316555008	J055706.56+121829.6	89.277	12.308	0.691 ± 0.019	Theia 2999	kA2hF1mF9	A2 V	A2 V
3424037096190044416	J055710.01+215831.0	89.292	21.975	0.528 ± 0.028	UBC 437	A1 V	A0 V	kA1hA3mK0 Eu
3424060014135510400	J055729.08+215955.5	89.371	21.999	0.504 ± 0.018	UBC 437	kB9hA9mG2 Eu	B9.5 III-IV	kB9.5hA9mK0 Eu
3342011364095009792	J055737.72+104940.1	89.407	10.828	0.58 ± 0.014	Theia 2999	kA2hA3mA5	A1 V	kA2hA4mA6
3343448906829672576	J055742.50+123225.7	89.427	12.54	0.569 ± 0.016	Theia 2999	kA1hA3mA5	A1 V SrSi	kA2hA4mA6
3424060220293913088	J055748.81+220040.8	89.453	22.011	0.521 ± 0.028	UBC 437	kA2hF5mK0	A1 V	A1 Vn
3342955019950652928	J055752.23+115029.6	89.468	11.842	0.607 ± 0.029	Theia 2999	A3 III-IV	kA3hA5mA8	A5 III-IV
3424062384957373056	J055804.97+220549.4	89.521	22.097	0.504 ± 0.025	UBC 437	A0 V	A0 V	kA1hA3mG2 Eu
3350666238592192768	J055847.68+190932.5	89.699	19.159	0.533 ± 0.015	COIN-Gaia 41	A1 IV-V Eu	kA1hA3mA3 Eu	A1 IV Eu
3341768264649521408	J055848.71+101515.5	89.703	10.254	0.619 ± 0.019	Theia 2999	kA0hF2mG5	B9.5 III	kA0hF0mG2 Eu
3350660947192649600	J055917.86+190309.2	89.824	19.053	0.52 ± 0.04	COIN-Gaia 41	A9 V	F0 mA6 V Lam Boo	F0 mA6 V Lam Boo
3342111660171749888	J055921.45+110230.5	89.839	11.042	0.626 ± 0.018	Theia 2999	?	A2 V (Sr)	kA3hA3mK0
3350648852565082240	J055927.37+190043.4	89.864	19.012	0.533 ± 0.016	COIN-Gaia 41	A2 V	A2 IV-V	kA2hA3mG9
3430432813592099712	J060124.95+272136.9	90.354	27.36	0.496 ± 0.017	HSC 1445	B9 V	B9 V	kA0hA3mG9
3424651856331150848	J060222.12+232414.7	90.592	23.404	0.997 ± 0.021	COIN-Gaia 24	kA3hF5mK0	A3 V	kA3hA3mK0
970354371980023936	J060227.45+495042.7	90.614	49.845	0.744 ± 0.014	NGC 2126	F1 V Fe-0.6	kA7hF2mF1	F1 V
970353444267073408	J060235.16+495351.2	90.647	49.898	0.741 ± 0.014	NGC 2126	F1 V	kA7hF2mF3	kA7hF1mF2
961316691341626496	J060236.70+431654.6	90.653	43.282	1.801 ± 0.026	Theia 390	F0 V Eu	F1 V	F0 V (Sr)SiEu
3424595510658249344	J060258.67+231112.2	90.745	23.187	0.985 ± 0.024	COIN-Gaia 24	B7 V	Unclassifiable	kB9hF0mK0 Eu
3424592452641562240	J060300.93+230423.8	90.754	23.073	0.99 ± 0.015	COIN-Gaia 24	A0 IV-V	A0 IV-V	kA0hA3mK1
970352443537765888	J060307.27+495157.5	90.78	49.866	0.771 ± 0.013	NGC 2126	F2 IV-V	F3 IV-V (Sr)	F2 IV-V (Sr)
960485499207637888	J060308.69+405948.2	90.786	40.997	1.756 ± 0.038	Theia 390	A0 V	A0 V	A3 mA0 V Lam Boo
961303329700390272	J060326.10+433332.5	90.858	43.559	1.783 ± 0.037	Theia 390	A9 mB8 V Lam Boo	B9 V	A9 mA2 V metal-weak
3345398130490334720	J060351.64+144051.6	90.965	14.681	1.157 ± 0.016	Theia 282	A9 mA4 V Lam Boo	kA5hA8mF0	kA6hF0mF0
3423635980604037760	J060359.34+220128.7	90.997	22.025	0.296 ± 0.032	FSR 0883	kB9.5hA1mA2	B9.5 IV-V	A3 mA2 metal weak
3423641753040056064	J060416.72+220226.5	91.07	22.041	0.32 ± 0.02	FSR 0883	B9 III Si	B9 III Si	kB9.5hF0mK0

Continued on next page

Table B.1.: (continued)

Gaia DR3	LAMOST ID	α	δ	$\varpi \pm \sigma_{\varpi}$	System	libnor36	libr18	libr18_225
3374855494403311104	J060509.33+201552.7	91.289	20.265	0.54 ± 0.031	Theia 6999	A4 IV	kA5hA7mA9	A6 IV
3423833338644274688	J060534.83+225227.8	91.395	22.874	0.209 ± 0.026	HSC 1493	B8 IV Si	Unclassifiable	F0 V Fe-6.0
3345064261208988160	J060623.68+133608.0	91.599	13.602	1.044 ± 0.023	Theia 282	B8 V	B8 V	kB8hF1mK0 Eu
3374391397417855872	J060652.54+190343.0	91.719	19.062	0.447 ± 0.03	FSR 0904	A2 V	kA1hA3mA4	A1 V
3344222237162906624	J060747.37+125040.8	91.947	12.845	1.268 ± 0.018	Theia 282	A1 V	A0 V	kA1hA3mK0
3374545049869390336	J060809.70+192853.9	92.04	19.482	0.419 ± 0.018	CWNU 2717	kB9hF0mA2 Eu	F0 mA0 V metal-weak	kB9.5hF0mA3 Eu
3426262335927800576	J060814.37+241415.3	92.06	24.238	1.141 ± 0.016	NGC 2168	F0 mA7 metal weak	kA6hA9mF0	A9 V
3426285941067612416	J060817.55+242910.8	92.073	24.486	1.209 ± 0.02	NGC 2168	B9.5 V	B9.5 V	kA0hA3mK1
3426281886618521728	J060823.24+242317.8	92.097	24.388	1.13 ± 0.014	NGC 2168	A6 V SrEu	kA5hA7mF1	kA5hA7mA9
3426280752747529344	J060827.16+242007.4	92.113	24.335	1.203 ± 0.021	NGC 2168	kB9hA9mF7 Eu	A0 III-IV	A8 mA2 V metal-weak
3426280576649857920	J060828.79+241840.9	92.12	24.311	1.138 ± 0.016	NGC 2168	kA2hF5mK0	A2 V	kA2hA3mK0
3426268520677780096	J060833.82+241658.1	92.141	24.283	1.085 ± 0.022	NGC 2168	A1 V	A1 V	kA2hA3mK0
3426262576445945344	J060835.71+241513.6	92.149	24.254	1.108 ± 0.015	NGC 2168	kA2hA4mA7	kA3hA7mA9	kA2hA7mA8
3425272706742206848	J060836.93+225005.2	92.154	22.835	0.209 ± 0.015	HSC 1493	F0 V Eu	kA8hF1mF2 Eu	A9 V
3374491693493469440	J060837.67+191632.4	92.157	19.276	0.481 ± 0.02	CWNU 2717	B8 III	B7 III-IV Si	F1 V Fe-6.0
3426282814331796096	J060843.06+242342.9	92.179	24.395	1.249 ± 0.017	NGC 2168	B9 IV-Vn	B9.5 IV-V	kB9.5hA8mK0 Eu
3426284394879346304	J060846.54+242820.6	92.194	24.472	1.1 ± 0.021	NGC 2168	B9 V	A0 V Si	A3 mA0 V Lam Boo
3426256765350856960	J060846.93+240551.9	92.195	24.097	1.174 ± 0.025	NGC 2168	B6 V	B7 V	kB9hF0mG2 Eu
3426269414033839616	J060848.01+242108.9	92.2	24.352	1.141 ± 0.017	NGC 2168	A0 IV-V	A0 V	kA1hA3mK0
3426267863546664192	J060848.38+241726.4	92.202	24.291	1.154 ± 0.014	NGC 2168	kA2hF5mK0	kA2hA3mK0	kA2hF5mK0
3426270925862316800	J060854.16+242209.4	92.226	24.369	1.188 ± 0.024	NGC 2168	B9 V	B8 V	kB9hA9mK0 Eu
3426268211443003264	J060855.25+241807.2	92.23	24.302	1.156 ± 0.017	NGC 2168	kA2hF5mK0	A2 V	kA2hA3mK0
3426257212027455360	J060856.20+240759.7	92.234	24.133	1.183 ± 0.019	NGC 2168	F2 V	F3 V (Sr)	F2 V
3426271509977845504	J060905.32+242535.3	92.272	24.426	1.165 ± 0.015	NGC 2168	F2 V	kA8hF2mF3 Sr	F2 V
3426264221414080384	J060905.47+241308.8	92.273	24.219	1.139 ± 0.021	NGC 2168	A9 Vn	kA7hA9mF1	A9 Vn
3426269547173842560	J060907.87+241819.1	92.283	24.305	1.159 ± 0.019	NGC 2168	A0 V	A0 V	kA1hA3mK0
3426264736810476928	J060914.94+241502.0	92.312	24.251	1.075 ± 0.022	NGC 2168	kA2hF5mK0	A3 mA1 metal weak	kA2hA3mK0
3425512846952824960	J060925.68+241007.4	92.357	24.169	1.186 ± 0.025	NGC 2168	A0 IV-V	A0 IV-V	kA0hA3mK1
3425511777503426432	J060930.86+240809.7	92.379	24.136	1.191 ± 0.021	NGC 2168	A0 V	A0 V	kA1hA3mK0
3426266214279218816	J060940.60+241926.4	92.419	24.324	1.113 ± 0.02	NGC 2168	A1 V	A1 V	kA2hA3mK0
3426266149858654336	J060942.91+241844.3	92.429	24.312	1.148 ± 0.018	NGC 2168	F1 V	kA7hF1mF1	F2 V
3426290236035226112	J060953.75+242225.2	92.474	24.374	1.202 ± 0.027	NGC 2168	F0 mB5 V Lam Boo	B9 IV-V	kB9hF0mK0 Eu
3425510677991795968	J061004.99+241038.5	92.521	24.177	1.08 ± 0.017	NGC 2168	A2 V	A1 V	kA2hA3mK0
3318608804556596864	J061026.94+045944.1	92.612	4.996	1.143 ± 0.02	NGC 2202	A2 IV-Vn	A1 IV-V (Sr)Si	A1 IV-Vn Si
3344053328986631168	J061040.86+130050.7	92.67	13.014	0.253 ± 0.024	CWNU 2471	F0 mB5 V Lam Boo	F0 mB8 V Lam Boo	kB9hF0mF9 Eu
3019790754200699136	J061056.36-061425.9	92.735	-6.241	1.232 ± 0.016	NGC 2183	B2 V	Unclassifiable	kB8hF2mK0 Eu
3343957087359610496	J061057.61+123312.1	92.74	12.553	0.295 ± 0.019	CWNU 2471	kB9.5hA9mK0 Eu	A0 III	kA0hA9mK0 Eu
3344032816222902528	J061058.39+124449.6	92.743	12.747	0.359 ± 0.029	CWNU 2471	B9.5 V	A0 IV-V	kA0hA3mK0
3019746705016600704	J061058.88-063320.2	92.745	-6.556	1.194 ± 0.015	NGC 2183	kA2hF5mK0	A3 mA0 metal weak	kA2hA3mK0
962831066747265792	J061120.29+445551.0	92.835	44.931	1.824 ± 0.028	Theia 390	kA2hF3mG2	A2 IV	kA2hF5mG9
960239792718089088	J061138.07+421022.9	92.909	42.173	1.732 ± 0.026	Theia 390	A1 V	A1 V	kA1hA3mK0
3344057791455498112	J061140.77+130612.8	92.92	13.104	1.212 ± 0.016	Theia 282	A6 II-III	kA7hF0mF1	F0 V
3344156678784346368	J061145.95+131450.1	92.941	13.247	1.031 ± 0.014	Theia 282	A4 II-III (Sr)	A6 III (Sr)	F0 V Fe-0.7
3344460560605443968	J061154.81+140515.2	92.978	14.088	1.079 ± 0.026	Theia 282	B9 V	B9 V	kB9hA3mK2
3344412250813299072	J061213.10+140103.0	93.055	14.017	3.23 ± 0.021	Theia 379	A5 II-III	kA6hF0mF1	kA6hF0mF0
3019780721157319424	J061225.08-061744.3	93.104	-6.296	1.204 ± 0.014	NGC 2183	kA2hF4mG9	A2 V	kA2hA3mF9
3019875485316186752	J061245.12-061227.7	93.188	-6.208	1.189 ± 0.015	NGC 2183	A1 V Eu	kA1hA2mA3	A2 V Eu
3330075306382878464	J061256.23+105118.9	93.234	10.855	1.274 ± 0.021	Theia 282	A3 mA0 V Lam Boo	A3 mA0 V Lam Boo	kB9hA3mK0
3344847760498238592	J061301.26+142411.7	93.255	14.403	0.188 ± 0.018	CWNU 2595	B3 V	O6 ?	kB9hF5mG9
3344194684951035136	J061305.06+133853.3	93.271	13.648	1.089 ± 0.021	Theia 282	kA2hF2mG2	A2 V	?
3330089217780816384	J061310.71+105552.0	93.295	10.931	1.241 ± 0.017	Theia 282	F0 V Fe-0.6	kA7hF0mF1	A9 V
3345851923851446912	J061311.40+155125.5	93.298	15.857	0.545 ± 0.018	FSR 0931	B9 Vn	B9.5 IV-V	kB9.5hA3mA2 Eu
3325088608834382976	J061321.37+065703.5	93.339	6.951	0.442 ± 0.022	Czernik 25	A0 V	A0 V	A3 mA0 V Lam Boo
3345877521855998080	J061322.13+155923.4	93.342	15.99	0.6 ± 0.021	FSR 0931	A2 V	kA1hA2mA3	A2 Vn

Continued on next page

Table B.1.: (continued)

Gaia DR3	LAMOST ID	α	δ	$\varpi \pm \sigma_\varpi$	System	libnor36	libr18	libr18_225
3344068859589942144	J061354.62+124819.5	93.478	12.805	0.226 ± 0.028	NGC 2194	kA2hF5mK0	A1 V	A2 Vn
3344070405777981056	J061356.05+124926.3	93.484	12.824	0.339 ± 0.03	NGC 2194	A1 V	kA1hA2mA3	A1 Vn
3374044398419804160	J061426.30+190030.1	93.61	19.008	0.497 ± 0.024	IRAS 06117+1901	B9 V	B9 V	kB9.5hA3mK2
3373847895076962688	J061454.79+184527.0	93.728	18.758	0.511 ± 0.037	IRAS 06117+1901	A2 V Eu	A1 V	A1 V
3373860500801601408	J061501.43+185715.2	93.756	18.954	0.495 ± 0.03	IRAS 06117+1901	B8 IV-V	B8 V	kB9hF0mK0 Eu
3373851365410096896	J061505.03+185331.9	93.771	18.892	0.422 ± 0.038	IRAS 06117+1901	A8 mA0 V Lam Boo	A8 mA0 V Lam Boo	kB9hA8mG2 Eu
3373850025380669184	J061522.34+185106.7	93.843	18.852	0.479 ± 0.032	IRAS 06117+1901	A1 V	A0 V	kA1hA3mK0
3373862905984241536	J061525.45+190324.5	93.856	19.057	0.474 ± 0.029	IRAS 06117+1901	A2 V Eu	A2 V	A2 V
3328836603456137856	J061638.25+091235.6	94.159	9.21	1.239 ± 0.026	Theia 282	A8 mB9.5 V Lam Boo	Unclassifiable	kB7hA8mG2 Eu
969184315512856960	J061651.19+481501.0	94.213	48.25	3.503 ± 0.021	HSC 1142	F1 V Fe-0.6	kA7hF2mF1	F0 V
3344922870886351488	J061717.43+144840.5	94.323	14.811	0.449 ± 0.024	Theia 2249	A0 V	A0 V	kA1hA3mK0
3344916922352996480	J061739.67+144052.8	94.415	14.681	0.375 ± 0.018	Theia 2249	B8 IV	B8 IV	kB9.5hF0mK0
960105373124005248	J061815.32+422356.1	94.563	42.399	1.849 ± 0.03	Theia 390	kA2hF5mK0	A2 V	kA2hA3mK0
3344725027512539392	J061819.59+143541.3	94.582	14.595	0.442 ± 0.015	Theia 2249	kB9hA9mA2 Eu	B9.5 IV	A3 mA1 metal weak
3377441369657126528	J061828.41+225820.8	94.618	22.972	0.728 ± 0.019	HSC 1500	kA0hA2mA5 Si	A0 IV-V Si	kA0hA3mA6 Si
3377541841828979456	J061901.54+233247.8	94.756	23.547	0.733 ± 0.019	HSC 1500	kA2hA4mA7	kA2hA5mA9 Si	kA2hA8mA9 Eu
3344712726726459520	J061909.56+143120.1	94.79	14.522	0.25 ± 0.024	UBC 1316	kA1hA2mA5 Si	A0 III-IV SrSi	kA1hA8mA8 SiEu
3373901015233220480	J061930.64+185403.5	94.878	18.901	0.233 ± 0.023	HSC 1520	A0 II Eu	A0 II-III Eu	F0 V Fe-0.9
3377448142822741120	J061954.33+230858.0	94.976	23.149	0.77 ± 0.022	HSC 1500	kA1hA3mA6 Sr	A1 IV-V SrSi	kA2hA6mA7
3377428347316647296	J062016.13+225436.6	95.067	22.91	0.766 ± 0.018	HSC 1500	A2 V (Sr)Si	A1 V SrSi	kA2hA3mA5 Si
3432091465539890176	J062032.62+260456.2	95.136	26.082	0.223 ± 0.028	HSC 1478	F0 mA1 metal weak	B9 III-IV	kB9.5hF0mF6 Eu
961585148273949056	J062041.58+424727.8	95.174	42.791	1.735 ± 0.025	Theia 390	A0 V	A0 V	kA0hA3mK0
3116838392113655936	J062044.22-033017.5	95.184	-3.505	0.662 ± 0.017	FoF 658	A3 IV Sr	kA3hA7mA7	A5 IV (Sr)
3116838422174509568	J062047.02-032911.4	95.196	-3.487	0.663 ± 0.016	FoF 658	kA2hA3mA6 Si	A1 IV SrSi	kA2hA7mA7 Si
3370703257462440320	J062049.87+180227.3	95.208	18.041	0.317 ± 0.016	HSC 1532	kB9hF0mF6 Eu	B9 III	kB9.5hF0mG0 Eu
3370901891109976704	J062058.52+185622.5	95.244	18.94	1.065 ± 0.018	CWNU 10	A3 IV-V SrEu	A3 IV-V SrSi	A5 IV-V SrEu
3116835913913608832	J062059.68-032914.5	95.249	-3.487	0.667 ± 0.017	FoF 658	A4 III-IVn	A6 V Si	A7 V Eu
3432237215253122304	J062102.11+262244.7	95.259	26.379	0.184 ± 0.021	HSC 1478	B4 IV	B4 IV-V	kB9hF2mF9 Eu
3370882409138878976	J062107.80+184745.7	95.282	18.796	0.999 ± 0.021	CWNU 10	B7 V	B8 IV-V	kB9hF1mG9 Eu
3377215523096613248	J062109.56+223725.5	95.29	22.624	0.735 ± 0.018	HSC 1500	A1 IV-V	A2 IV-V	kA2hA3mG1
3370888319013858688	J062111.30+184913.0	95.297	18.82	1.04 ± 0.027	CWNU 10	B6 V	B8 IV-V	kB9hF1mK0 Eu
3370888250294380032	J062116.03+184818.6	95.317	18.805	1.065 ± 0.023	CWNU 10	A3 mA0 V Lam Boo	A0 V	A3 mA0 V Lam Boo
3370888692672075264	J062118.88+185105.9	95.329	18.852	1.024 ± 0.023	CWNU 10	kA2hA3mA6 Eu	A1 IV	kA2hA3mA7 Eu
3370510774206899200	J062128.13+175601.0	95.367	17.934	0.287 ± 0.021	HSC 1532	A9 mB9.5 V Lam Boo	A9 mB9 V Lam Boo	A9 mB9 V metal-weak
3370726622084340096	J062128.16+181747.1	95.367	18.296	0.284 ± 0.026	HSC 1532	B9.5 IV	A0 III-IV	kA0hA3mK1
3123796995047342976	J062129.12+020535.1	95.371	2.093	0.44 ± 0.02	CWNU 1313	kB9hA2mA5 SrSiEu	B9.5 IV-V Si	kA0hA3mA5 SiEu
3370708239624841344	J062135.65+180741.4	95.399	18.128	0.286 ± 0.024	HSC 1532	F0 mB8 V Lam Boo	B8 IV-V	kB9hF0mK0
3377260401211784448	J062144.59+225356.7	95.436	22.899	0.705 ± 0.015	HSC 1500	A2 V	A1 V Si	kA2hA3mA5
3370884814320482176	J062148.92+184832.1	95.454	18.809	0.99 ± 0.022	CWNU 10	A9 mB8 V Lam Boo	B9.5 III-IV	kB9hA9mG2 Eu
3370513213748279808	J062149.81+180218.9	95.458	18.039	0.252 ± 0.029	HSC 1532	A1 IV (Sr)	A1 IV (Sr)	A3 mA1 metal weak
3377158043551681792	J062152.93+222056.2	95.471	22.349	0.36 ± 0.021	FoF 1973	kA1hA3mA6	A0 IV	kA1hA3mA7
3377167561199167744	J062208.77+222635.2	95.537	22.443	0.382 ± 0.033	FoF 1973	kA2hF2mG1	A2 V	kA3hF3mG2
3370508369025181824	J062209.33+175446.7	95.539	17.913	0.282 ± 0.025	HSC 1532	B9 V	A0 IV	kA1hA3mF9
3368697576454232320	J062217.42+143726.6	95.573	14.624	0.546 ± 0.018	FSR 0951	kA2hA3mA6 Sr	A1 IV-V SrSi	kA2hA6mA7
3377164262664284160	J062220.64+222353.3	95.586	22.398	0.715 ± 0.02	HSC 1500	kA3hA5mA7	kA4hA8mF0 Sr	kA4hA9mF1 Sr
3432198530484903168	J062231.17+262932.4	95.63	26.492	0.203 ± 0.027	HSC 1478	kB9hF1mG1 Eu	F1 mA3 IV-V metal-weak	F1 mB9.5 IV-V metal-weak
3370515172253334272	J062231.44+180055.6	95.631	18.015	0.277 ± 0.03	HSC 1532	kA2hF5mK0	A1 V	kA2hA3mK0
3440748813937995904	J062231.66+353544.6	95.632	35.596	4.112 ± 0.018	HSC 1142	F0 V Fe-0.5	kA7hF1mF1	F0 V
3431883314245170176	J062233.43+255427.4	95.639	25.908	0.212 ± 0.033	HSC 1478	B9 IV	B9.5 III-IV	kB9.5hF0mA5
3370833824468687104	J062251.68+184136.1	95.715	18.693	0.997 ± 0.019	CWNU 10	A1 V	A1 V	kA1hA3mK0
3432273774016768000	J062253.01+264619.6	95.721	26.772	0.19 ± 0.023	HSC 1478	kB9.5hF1mG8 Eu	kB9.5hF1mG3	F2 mA0 IV-V metal-weak
3432220172824250624	J062332.92+263247.4	95.887	26.547	0.197 ± 0.021	HSC 1478	kB9hF1mG9 Eu	B9 III	F1 mB9.5 IV-V metal-weak
3330884473923251968	J062413.02+112734.2	96.054	11.46	0.448 ± 0.022	UBC 1319	A3 mA0 V Lam Boo	A0 V	A3 mA0 V Lam Boo
3372437530897057920	J062433.25+192938.0	96.139	19.494	0.253 ± 0.027	Bochum 1	kB9hA9mA1 Eu	A0 III	kB9.5hA9mF9 Eu

Continued on next page

Table B.1.: (continued)

Gaia DR3	LAMOST ID	α	δ	$\varpi \pm \sigma_{\varpi}$	System	libnor36	libr18	libr18_225
3372486042550712960	J062543.41+195416.1	96.431	19.904	0.24 ± 0.026	Bochum 1	kB9.5hF1mK0 Eu	kB9.5hF2mG8	kA0hF1mK0 Eu
3131411452368344320	J062545.62+041649.9	96.44	4.281	0.417 ± 0.035	HSC 1631	kA2hA7mA6 SiEu	A7 mA0 metal weak	kA2hA7mA7 SiEu
3372486390444686080	J062550.50+195452.9	96.46	19.915	0.26 ± 0.028	Bochum 1	kA2hF2mG1	A2 IV-V	A2 IV-V
3372466255638764928	J062601.84+194004.7	96.508	19.668	0.275 ± 0.018	Bochum 1	kB9hF0mK0 Eu	B9 III	kB9.5hF0mK0 Eu
3372466874113370240	J062606.00+194209.7	96.525	19.703	0.221 ± 0.025	Bochum 1	F1 V Fe-13.5	F1 mA3 V Lam Boo	F1 V Fe-6.4
3372473260726120832	J062609.31+195026.8	96.539	19.841	0.266 ± 0.022	Bochum 1	B2 V	B2 V	kB9hF2mK0
3372175194293140736	J062631.40+190602.3	96.631	19.101	0.244 ± 0.029	Theia 2725	F0 mB5 V Lam Boo	B8 V	kB9hF0mA3 Eu
3383775213765153024	J062711.33+245853.7	96.797	24.982	0.317 ± 0.053	HSC 1494	kA2hF3mG2	A2 V	A2 Vn
3383663201017803136	J062720.97+244425.1	96.837	24.74	0.285 ± 0.034	HSC 1494	A3 IV-V Eu	A3 IV-Vn	A3 IV-V Eu
3383663231079236736	J062722.28+244447.8	96.843	24.747	0.356 ± 0.038	HSC 1494	kA2hF5mK0	A2 V Eu	kA2hA3mK0 Eu
3383777309709400448	J062726.26+250321.8	96.859	25.056	0.303 ± 0.047	HSC 1494	kA2hA3mA5 Si	A1 V SrSi	kA2hA5mA6
3131147608236858752	J062752.75+035054.6	96.97	3.848	0.386 ± 0.018	HSC 1631	A9 mA2 V Lam Boo	A9 mA0 V metal-weak	kB9hA9mA3 Eu
3383462333987418240	J062754.22+242134.1	96.976	24.359	0.312 ± 0.016	HSC 1494	A0 II-III	B9.5 III	kA0hF0mA7
3131209657625634816	J062755.67+041026.5	96.982	4.174	0.443 ± 0.016	HSC 1631	B9 III-IV	B8 IV	kB9hF0mK0 Eu
3383771812150964096	J062759.04+245624.5	96.996	24.94	0.275 ± 0.039	HSC 1494	A2 Vn	A2 IV-V	kA2hF5mK0
3383464807888499200	J062811.35+242746.9	97.047	24.463	0.319 ± 0.023	HSC 1494	B9.5 IV-V	A0 V	kA0hA3mK1
3383753223532595200	J062812.77+244444.7	97.053	24.746	0.326 ± 0.029	HSC 1494	A1 V Eu	A1 V	kA1hA3mK0 Eu
3383870493318523520	J062826.13+253355.7	97.109	25.565	0.328 ± 0.018	HSC 1494	kB9.5hA1mA2	A0 III-IV	A3 mA1 metal weak
3372303837153591296	J062827.04+192728.7	97.113	19.458	0.242 ± 0.035	Theia 2725	kB9.5hA8mK0 Eu	A0 IV	A8 mA0 V Lam Boo
3372128361970147328	J062841.09+185059.0	97.171	18.85	0.206 ± 0.029	Theia 2725	kB9.5hF0mG2 Eu	A0 III	kA0hF0mK0 Eu
3372304008952260608	J062845.44+192720.4	97.189	19.456	0.212 ± 0.027	Theia 2725	kB9.5hA1mA2 SrSi	B9.5 II-III Si	F1 V Fe-1.0
3131357610660104704	J062846.26+044210.8	97.193	4.703	1.021 ± 0.018	Theia 189	kA2hA7mA6 SiEu	A1 IV SrSi	kA2hA7mA7 SiEu
3371314001812134912	J062855.99+180628.1	97.233	18.108	0.275 ± 0.03	Theia 2725	kB9hF0mK0 Eu	F0 mA1 V metal-weak	F0 mA0 V metal-weak
3383565585001209728	J062901.56+244417.5	97.257	24.738	0.31 ± 0.035	HSC 1494	A0 V	A0 V	A3 mA0 V Lam Boo
3372286794724082304	J062922.99+192036.8	97.346	19.344	0.21 ± 0.022	Theia 2725	kB9.5hF0mA2 Eu	B9.5 III	kA0hF0mA2 Eu
3383542254738940544	J062926.06+242410.2	97.359	24.403	0.345 ± 0.025	HSC 1494	kA2hF3mG2	A2 IV	kA3hF5mG8
3372107501312472448	J062933.75+183954.1	97.391	18.665	0.196 ± 0.027	Theia 2725	kA1hF5mK2	A0 III-IV	A8 mA1 V metal-weak
3372282087439938048	J062944.75+191433.8	97.436	19.243	0.259 ± 0.026	Theia 2725	B7 V	Unclassifiable	kB9hF1mK0
3371313623853637120	J063014.01+182037.1	97.558	18.344	0.287 ± 0.024	Theia 2725	A0 IV	A3 mA0 IV metal-weak	kA1hA3mK0 Eu
3371307954497279232	J063053.13+181309.3	97.721	18.219	0.22 ± 0.042	Theia 2725	kA3hF5mK0	A3 V	kA3hF5mK0
3356587589744958080	J063110.37+150037.5	97.793	15.01	0.38 ± 0.022	UBC 203	?	kA2hA4mA6	A2 IVn
3356584394289284224	J063121.45+145920.3	97.839	14.989	0.368 ± 0.024	UBC 203	kA1hF5mK0	A1 IV	kA2hF5mK0
3132033608451774976	J063138.24+060645.3	97.909	6.113	1.123 ± 0.019	Theia 189	A2 V Eu	A1 V Si	A3 V Eu
3131329435679682176	J063141.93+045232.9	97.925	4.876	0.692 ± 0.017	NGC 2244	kA1hF3mG7	A0 III	kA1hA9mK0 Eu
3371278748719631744	J063146.28+180513.0	97.943	18.087	0.181 ± 0.02	Theia 2725	A0 II	kA0hA1mA2	?
3371344410179393664	J063159.85+183411.6	97.999	18.57	0.175 ± 0.049	Theia 2725	kA3hF3mG2	A3 IV-V	A2 V
3131334967590689536	J063207.38+045455.8	98.031	4.916	0.649 ± 0.017	NGC 2244	F0 mB5 V Lam Boo	B7 V	kB8hF0mK0 Eu
3131335040608985216	J063213.98+045514.2	98.058	4.921	0.671 ± 0.017	NGC 2244	B8 IV Si	emission-line?	F1 V Fe-0.8
3371388729943246848	J063243.89+182928.7	98.183	18.491	0.234 ± 0.022	Theia 2725	B9 III Si	B9.5 III Si	F1 V Fe-6.5
3355207045519718656	J063255.85+122326.7	98.233	12.391	0.486 ± 0.025	Theia 2133	A1 V	A3 mA0 metal weak	kA2hA3mK0
3355201449181755904	J063300.71+121818.9	98.253	12.305	0.438 ± 0.028	Theia 2133	A2 Vn	A1 Vn (Sr)	kA2hA3mK0
3371388287565087360	J063319.64+183348.6	98.332	18.563	0.22 ± 0.02	Theia 2725	kB9.5hF1mG5	B9 III-IV	kB9.5hF0mG2 Eu
3131724778822809984	J063334.66+051742.8	98.394	5.295	1.155 ± 0.019	Theia 189	B8 IV	B8 IV-V	kB8hF0mG1
3382229781453343104	J063341.21+222215.3	98.422	22.371	0.695 ± 0.016	FSR 0905	kA2hF1mF9 Eu	A2 IV-V	kA2hA3mF7
3382223837218612992	J063342.48+222037.1	98.427	22.344	0.692 ± 0.021	FSR 0905	A6 III-IV (Sr)	kA7hA8mF0	A8 IV-V
3355210245274640768	J063343.16+122746.5	98.43	12.463	0.476 ± 0.024	Theia 2133	A0 V	A0 V	kA0hA3mK0
3382211742590705536	J063351.77+221841.6	98.466	22.312	0.688 ± 0.019	FSR 0905	A4 II-III (Sr)	kA5hA9mA9	F0 mA8 metal weak
3355212371279602304	J063406.61+123209.4	98.528	12.536	0.218 ± 0.027	HSC 1593	kB9hF0mA3 Eu	B9.5 III-IV	kB9.5hF0mA4 Eu
3355241409558154368	J063425.49+124043.5	98.606	12.679	0.182 ± 0.03	HSC 1593	kA2hF4mG8	kA1hA3mK1	kA2hF5mK0
3355247869187859456	J063454.56+124450.4	98.727	12.747	0.149 ± 0.032	HSC 1593	A0 IV	A0 IV-V	kA0hA3mK0
3370979509758190080	J063509.20+171629.0	98.788	17.275	0.199 ± 0.032	HSC 1552	F0 mB5 V Lam Boo	F0 mB7 V Lam Boo	kB9hF0mA3 Eu
3355247663029304576	J063531.24+125137.3	98.88	12.86	0.193 ± 0.026	HSC 1593	kB9hF1mG8 Eu	B9.5 II-III	kB9.5hF1mF9 Eu
3352186553938779520	J063532.55+121410.8	98.886	12.236	0.296 ± 0.024	HSC 1593	kB9.5hF0mA4 Eu	F0 V Fe-0.7	kA0hF0mA5 Eu
3370989572863316352	J063548.33+173005.9	98.951	17.502	0.238 ± 0.028	HSC 1552	A1 V Eu	A1 V Eu	kA1hA3mG0 Eu

Continued on next page

Table B.1.: (continued)

Gaia DR3	LAMOST ID	α	δ	$\varpi \pm \sigma_\varpi$	System	libnor36	libr18	libr18_225
3355226737949262336	J063557.46+123449.9	98.989	12.581	0.178 ± 0.021	HSC 1593	F2 mB9.5 IV-V metal-weak	kB9.5hF2mG8	F2 mA0 IV-V metal-weak
3352223043980727680	J063601.82+122755.4	99.008	12.465	0.23 ± 0.02	HSC 1593	A0 II-III	kA0hA1mA2	kA0hF0mA4 Eu
3352225208644149632	J063619.10+123222.2	99.08	12.54	0.216 ± 0.03	HSC 1593	A0 III	A0 III Sr	A9 mA0 V metal-weak
3358875948321626880	J063634.00+165547.2	99.142	16.93	0.219 ± 0.023	HSC 1552	F0 mA1 metal weak	B9 IV	kB9.5hA9mA3 Eu
3358947004260524160	J063645.84+170026.9	99.191	17.007	0.217 ± 0.032	HSC 1552	B9.5 IV-Vn	A0 IV Eu	kA0hA3mA3 Eu
3131891973309856640	J063711.47+060325.4	99.298	6.057	0.668 ± 0.025	Collinder 106	B5 IV	B7 III-IV	kB9hF2mG2 Eu
3352202393777860096	J063729.40+121736.4	99.373	12.293	0.258 ± 0.019	HSC 1593	F0 mA1 metal weak	B9 III-IV	kA0hF0mA2 Eu
3352147761794598784	J063813.71+120508.9	99.557	12.086	0.19 ± 0.023	HSC 1593	kB9hF1mG2 Eu	B9 II-III	F1 mB9.5 IV-V metal-weak
3352306194547889664	J063854.06+123408.1	99.725	12.569	0.174 ± 0.043	HSC 1593	F1 mA2 V Lam Boo	A0 II	F1 mA0 V Lam Boo
3106360080662828544	J063944.72-032916.0	99.936	-3.488	0.467 ± 0.025	UBC 441	kA2hF5mK0	A1 V	kA2hA3mK0
3352236409920005376	J063949.64+121425.6	99.957	12.24	0.245 ± 0.017	HSC 1593	kB9.5hF0mA2 Eu	B9.5 III	kB9.5hF0mA3 Eu
3100546206773591936	J064102.71-055121.6	100.261	-5.856	0.905 ± 0.027	Teutsch 177	A0 V	A0 V	kA1hA3mA3
3127258837469863296	J064320.92+024602.6	100.837	2.768	3.341 ± 0.018	Theia 379	A3 IV-V (Sr)	A2 IV Sr	A4 IV-V
3351199433012489088	J064403.00+113128.5	101.012	11.525	0.225 ± 0.029	HSC 1600	kB9hF0mA2 Eu	B9.5 III-IV	kB9.5hA9mA3 Eu
3134495449344921216	J064407.44+092033.3	101.031	9.343	3.069 ± 0.031	Theia 379	A2 V	A1 V (Sr)Si	kA2hA3mA5
3125830610523466240	J064416.29+011424.8	101.068	1.24	0.691 ± 0.023	CWNU 2558	kA2hF1mF9	A2 V	A2 Vn
3127617901036740096	J064502.13+035214.8	101.259	3.871	0.685 ± 0.018	Theia 1734	A8 mA0 V Lam Boo	A8 mA0 V Lam Boo	kB9hA8mA5 Eu
3133969225652806784	J064504.50+073214.3	101.269	7.537	0.669 ± 0.016	Theia 2118	A0 V	A0 V	kA1hA3mK0
3133998607529569152	J064600.03+074626.1	101.5	7.774	0.671 ± 0.015	Theia 2118	kA2hF5mK0	A1 V	A2 Vn
3125739694655670912	J064648.40+012235.9	101.702	1.377	0.567 ± 0.019	vdBergh 85	A3 mB9 V Lam Boo	A0 V	A3 mA0 V Lam Boo
3351603194298799872	J064651.47+115729.7	101.714	11.958	0.172 ± 0.032	UBC 1322	B9.5 V	A0 IV-V	kA0hA3mG0
3133197991264920448	J064656.43+072137.9	101.735	7.361	0.652 ± 0.021	Theia 2118	B9 V	A0 IV	kA0hA3mG9
3133209634916378880	J064724.15+072113.0	101.851	7.354	0.655 ± 0.017	Theia 2118	A9 mB5 V Lam Boo	B9 IV-V Si	kB9hA9mG2 Eu
3113575900599414656	J065148.85+002655.8	102.954	0.449	1.112 ± 0.016	NGC 2301	F1 V	kA7hF1mF1	F1 V
3113579405293192064	J065200.60+003527.8	103.003	0.591	1.226 ± 0.024	NGC 2301	A1 IV-V	A1 IV-V	kA1hA3mK0
3381339932946897024	J065415.14+250127.3	103.562	25.024	3.373 ± 0.017	HSC 1447	F1 V Fe-0.6	A7 IV-V	kA7hF1mF0
3114552709299879808	J070412.72+010246.1	106.053	1.046	0.239 ± 0.017	NGC 2324	A9 mA5 metal weak	kA2hA4mA6	kA3hA9mA6 Eu
3114552537501192192	J070413.85+010131.1	106.058	1.025	0.247 ± 0.026	NGC 2324	A1 IV-V Eu	A0 IV-V	A1 IV-V Eu
3161355071002841984	J070506.56+132616.1	106.277	13.438	3.244 ± 0.023	Theia 379	F2 V	kA8hF3mF3	F2 IV-V
3114284535841554304	J070925.03+003117.3	107.354	0.521	0.3 ± 0.025	UBC 1344	A1 V	A0 V	kA1hA3mA5
3114284295323395072	J070925.04+003018.5	107.354	0.505	0.31 ± 0.021	UBC 1344	kB9hF0mA4 Eu	F0 mA0 V metal-weak	kB9.5hF0mA5 Eu
3114288143614045312	J070925.08+003450.7	107.355	0.581	0.271 ± 0.022	UBC 1344	A1 IV-V	kA1hA3mA4	A2 IV-V
3111387460140111616	J071143.56+004809.6	107.932	0.803	0.467 ± 0.023	Gulliver 47	kB9.5hA9mG1 Eu	B9.5 IV	kA0hA8mG2 Eu
3160328818634694400	J071422.20+124939.8	108.592	12.828	2.931 ± 0.026	Theia 379	A0 IV-V SrSiEu	A0 IV SrSiEu	kA1hA7mA8 Eu
3110130988929059328	J071603.49-005608.2	109.015	-0.936	1.187 ± 0.019	UPK 429	kA3hA8mA8	kA5hA8mF1	kA5hA9mF1 SrEu
3166529480099331584	J071656.17+134441.2	109.234	13.745	0.553 ± 0.019	NGC 2355	kA7hF0mF0 SiEu	kA6hA9mF1 SiEu	kA7hF0mF1 SiEu
3166528518026640768	J071712.37+134353.8	109.302	13.732	0.525 ± 0.02	NGC 2355	A5 II-III	kA6hA5mA9	kA6hF0mF0
3149216020253057920	J073421.78+085012.1	113.59	8.836	3.055 ± 0.018	Theia 379	kA3hF0mF0 Eu	kA4hA7mF1	kA4hF0mF1
865401619125252608	J073829.36+213430.9	114.622	21.575	0.409 ± 0.018	NGC 2420	A4 IV (Sr)Si	kA5hA6mA9 Si	kA4hA6mA8 Si
3088092072922203392	J075530.08+021509.6	118.875	2.253	1.493 ± 0.027	Alessi 145	B9.5 V	A0 V	A3 mA0 V Lam Boo
3087869078220356992	J075608.84+014206.0	119.037	1.702	1.364 ± 0.028	Alessi 145	A2 V	A1 V Si	A3 V
3089084691404228480	J075712.99+032340.7	119.304	3.395	1.483 ± 0.027	Alessi 145	B9 V	B9 V	A3 mB9.5 V Lam Boo
3087905740057334272	J075729.21+020428.2	119.372	2.074	1.425 ± 0.02	Alessi 145	A8 Vn	kA6hA9mA9	A9 V
3087960646923284096	J080235.14+021718.5	120.646	2.288	1.601 ± 0.02	Alessi 145	kA3hA9mA8 Eu	kA4hA8mF0	kA4hA9mF0 Eu
3094423644990242432	J080349.05+040054.0	120.954	4.015	1.647 ± 0.033	Alessi 145	B9 V	B9 V	kB9hA9mG2 Eu
3094422201881243008	J080356.48+035633.1	120.986	3.943	1.635 ± 0.031	Alessi 145	A0 V	A0 V	kA1hA3mK0
3094637981037666688	J080742.26+042041.6	121.926	4.345	1.693 ± 0.026	Alessi 145	kA3hA6mA7	kA5hA8mF1	kA5hF0mF0
3097598690973199616	J081211.64+071641.4	123.048	7.278	1.712 ± 0.028	Alessi 145	A1 V	A0 V	kA1hA3mK0
3089777315008435968	J081212.28+005533.4	123.051	0.926	1.403 ± 0.023	Alessi 145	F1 IV (Sr)	F2 IV (Sr)	F1 IV (Sr)
3064536067088101504	J081254.86-054047.3	123.229	-5.68	1.33 ± 0.018	NGC 2548	kA2hA8mA8 Eu	kA2hA8mF1 SiEu	kA2hA8mF0 SiEu
3064474455780216576	J081302.73-055859.1	123.261	-5.983	1.296 ± 0.014	NGC 2548	kA4hA9mF1 SiEu	kA5hA9mF2 Si	kA5hA9mF1 SiEu
3064533180870078976	J081305.38-054500.6	123.272	-5.75	1.394 ± 0.029	NGC 2548	kA2hF2mG2	A1 IV	kA2hA3mG8
3064486516048361216	J081328.66-054815.1	123.369	-5.804	1.347 ± 0.022	NGC 2548	A2 IV	A1 IV Si	A2 IV
3064488135253031936	J081340.39-054220.1	123.418	-5.706	1.366 ± 0.024	NGC 2548	kA2hF5mK0	A2 V	kA3hA3mK0

Continued on next page

Table B.1.: (continued)

Gaia DR3	LAMOST ID	α	δ	$\varpi \pm \sigma_\varpi$	System	libnor36	libr18	libr18_225
3064581971698426752	J081343.38-054133.6	123.431	-5.693	1.292 ± 0.023	NGC 2548	A0 IV	A0 IV-V	kA1hA3mK0
3098358178630780672	J081350.93+083953.8	123.462	8.665	1.91 ± 0.03	Theia 256	A3 mA0 IV-V metal-weak	kB8hB9.5mA1	A3 mA0 IV metal-weak
3064480369952647552	J081352.11-055420.5	123.467	-5.906	1.317 ± 0.016	NGC 2548	A2 IVn	A2 IV	kA3hA6mF7
3064487035741401984	J081352.61-054424.9	123.469	-5.74	1.33 ± 0.028	NGC 2548	kA2hA7mA7 SrEu	A1 IV SrSi	kA2hA7mA8 SrSi
3064482259738248576	J081355.78-055127.7	123.482	-5.858	1.289 ± 0.021	NGC 2548	A3 IV SrSi	A3 IV SrSi	kA3hA7mA7 Sr
3064482294097982208	J081358.96-055040.1	123.496	-5.844	1.316 ± 0.018	NGC 2548	kA2hA3mA5 Si	kA2hA7mA8 SrSi	kA2hA6mA6 SrSi
3064468236668444928	J081402.40-055646.9	123.51	-5.946	1.349 ± 0.026	NGC 2548	A0 V Si	A0 V (Sr)Si	A1 V Si
3064581421942594048	J081403.19-054144.5	123.513	-5.696	1.323 ± 0.023	NGC 2548	A0 IV-V	A0 IV-V	kA1hA3mF9
3064577603714961152	J081406.63-054602.0	123.528	-5.767	1.321 ± 0.015	NGC 2548	F0 IV-V	kA7hA5mF0	F0 IV-V
3064583036850271232	J081420.28-053957.4	123.585	-5.666	1.354 ± 0.022	NGC 2548	A1 V Si	A0 V Si	kA1hA3mA3
3064563623597151104	J081439.16-055147.4	123.663	-5.863	1.35 ± 0.019	NGC 2548	A2 V	A4 mA0 metal weak	kA2hA3mA5
3064466145020928640	J081444.44-055525.9	123.685	-5.924	1.331 ± 0.014	NGC 2548	F1 V	kA7hA9mF1	F1 V
3096687917387288704	J081546.81+062517.1	123.945	6.421	1.812 ± 0.014	Theia 256	F5 V	F6 V (Sr)	F5 V
3097149987148625152	J081706.57+070714.2	124.277	7.121	1.81 ± 0.024	Theia 256	kA3hF3mG2	A3 V	kA3hA3mG2
3097958334354009216	J081720.30+074207.8	124.335	7.702	1.926 ± 0.029	Theia 256	B9 V	B9.5 IV-V	kB9hA3mG2
4469347538066860928	J175919.86+030710.0	269.833	3.119	1.822 ± 0.02	Melotte 186	A5 III-IV (Sr)	A7 II-III	A7 II-III
4469342938160504704	J175945.24+030206.0	269.939	3.035	1.829 ± 0.018	Melotte 186	B9.5 IV-V Si	A0 IV-V SrSiEu	kA0hA7mA9 SiEu
4469477009858348032	J180110.46+032811.6	270.293	3.47	1.794 ± 0.015	Melotte 186	A0 V	A0 V	kA1hA3mK0
4469325071096213504	J180136.56+030952.6	270.402	3.165	1.799 ± 0.017	Melotte 186	A3 III-IV	kA2hA5mA8	kA2hA7mA6
2051105376456445824	J192059.97+374603.2	290.25	37.768	0.191 ± 0.019	NGC 6791	F0 II-III	kF0hA8mF3 Sr	F0 II-III
4214746657076763904	J192335.01-014957.9	290.896	-1.833	1.175 ± 0.015	Theia 202	kA2hF3mG2	A2 V	kA2hA3mK0
4214571830414603648	J192408.01-022402.3	291.033	-2.401	1.18 ± 0.014	Theia 202	F0 V	kA7hA9mF0	F0 V
4214356704088836864	J192412.26-024616.0	291.051	-2.771	1.21 ± 0.016	Theia 202	F0 V	kA7hF1mF2 Eu	F0 V
4214378316364257536	J192448.22-023312.6	291.201	-2.554	1.175 ± 0.019	Theia 202	A4 IV	A7 V	A8 V Eu
4213525615044159744	J192645.31-031639.3	291.689	-3.278	1.21 ± 0.019	Theia 202	A3 mA0 V Lam Boo	A3 mA0 V Lam Boo	A3 mA0 V Lam Boo
2025481361110620544	J193442.58+281638.9	293.677	28.277	1.077 ± 0.013	UPK 80	kA2hA7mA7 SrEu	A3 IV SrSi	kA3hA7mA9 SrSiEu
2025465830511725440	J193535.05+281041.9	293.896	28.178	1.16 ± 0.024	UPK 80	A1 V	A0 V	kA1hA3mK0
2128121493055456512	J193651.91+462320.4	294.216	46.389	0.843 ± 0.012	NGC 6811	A9 V Eu	A9 V	A8 IV-Vn
2128144337980908160	J193717.09+462314.6	294.321	46.387	0.853 ± 0.011	NGC 6811	A6 III-IV	kA7hA8mF0	A8 V
2128108706931869440	J193725.55+461836.3	294.357	46.31	0.825 ± 0.012	NGC 6811	A8 V Eu	kA7hA7mF0	A8 Vn Eu
2128132556891272320	J193727.04+462253.6	294.363	46.382	0.856 ± 0.011	NGC 6811	kA4hF0mA8	kA4hA9mF0	kA5hF0mF0
2128132930547764992	J193744.80+462500.9	294.437	46.417	0.844 ± 0.012	NGC 6811	A5 IV Sr	A7 V Sr	A7 V (Sr)
2085244731463742848	J195727.85+454000.4	299.366	45.667	0.761 ± 0.01	UBC 143	A7 V Eu	A7 V	A7 V
2085246793048249344	J195832.68+454244.8	299.636	45.712	0.743 ± 0.01	UBC 143	A4 III-IV (Sr)	A7 V	A9 Vn Eu
2085197658620931968	J195901.26+453309.3	299.755	45.553	0.753 ± 0.01	UBC 143	A6 V SrSiEu	kA5hA7mA9	kA5hA8mA9 SrSiEu
2030917552726244352	J195917.24+311225.7	299.822	31.207	0.323 ± 0.014	UBC 1078	F0 mB5 V Lam Boo	F0 mB7 V Lam Boo	F0 V Fe-0.9
2076066351994581120	J200315.97+441306.1	300.817	44.218	0.684 ± 0.011	NGC 6866	kA3hA9mF1 SiEu	kA3hA9mF2 SiEu	kA3hA9mF1 SiEu
2075875552369147904	J200336.27+440250.4	300.901	44.047	0.689 ± 0.012	NGC 6866	kA2hA3mA7 Si	A1 V SrSi	kA2hA6mA8 Si
2075877678366383744	J200357.13+440816.8	300.988	44.138	0.685 ± 0.011	NGC 6866	F1 V Sr Sr	F0 V Sr Sr	kF1hA9mF5 SiEu
2075877648313310848	J200404.80+440933.6	301.02	44.159	0.681 ± 0.01	NGC 6866	F0 IV-V	kA9hA9mF3 SrSi	A9 IV-V Si
2081882562346895232	J200416.18+441204.6	301.067	44.201	0.679 ± 0.011	NGC 6866	A4 III	kA7hF0mF0	F0 V Fe-0.5
2081881355448238720	J200419.32+440723.8	301.08	44.123	0.674 ± 0.013	NGC 6866	A5 V SrSiEu	kA5hA8mF1 SrSi	kA5hA5mA9 SiEu
2059202695503955584	J200754.27+361314.1	301.976	36.221	0.316 ± 0.022	Theia 4725	kA2hA3mA6	A1 IV	kA2hA3mA7
2061223872730643584	J202245.59+385511.0	305.69	38.92	0.608 ± 0.014	UBC 374	F0 V SrEu	kA8hF0mF2 SiEu	F0 V SrSiEu
2057949492739155584	J202251.56+371312.2	305.715	37.22	0.463 ± 0.015	Theia 1975	F1 mA1 V Lam Boo	kA0hA3mA7	NaN
2064180322053115520	J202807.79+385714.0	307.032	38.954	0.613 ± 0.015	UBC 1103	F2 V Fe-1.0	kB9.5hA2mA5	F2 V Fe-0.9
2064074184821575040	J202833.98+381035.5	307.142	38.177	0.941 ± 0.015	CWNU 180	B9 V	A0 IV-V (Sr)	kA0hA3mF6
2070722931639133184	J203514.41+450726.0	308.81	45.124	0.322 ± 0.018	HSC 655	kA6hA9mF1 SiEu	kA6hA9mF2 Eu	kA6hA8mF1 SiEu
2070344734000894592	J203638.13+450646.7	309.159	45.113	0.346 ± 0.014	HSC 655	B9 III-IV	B9.5 III-IV	kB9.5hA9mK0 Eu
2070346039671128960	J203733.59+450423.8	309.39	45.073	0.429 ± 0.016	HSC 655	kA1hA2mA3	A0 III	kA1hA9mA6 Eu
1871158238309294208	J204939.62+374732.9	312.415	37.792	1.093 ± 0.012	CWNU 96	F0 V Fe-0.6	kA7hF0mF0	A9 V Eu
1870950430617096832	J205112.59+373348.2	312.802	37.563	1.059 ± 0.013	CWNU 96	B9.5 V	A0 V	A3 mA0 V Lam Boo
1870944452022711808	J205215.09+373400.1	313.064	37.567	0.773 ± 0.014	Roslund 7	B8 III	B8 IV	kB8hF1mG2
1872447106455974144	J205252.68+374425.2	313.22	37.74	0.765 ± 0.01	Roslund 7	A8 mB8 V Lam Boo	B9 V	kB9hA8mK0 Eu

Continued on next page

Table B.1.: (continued)

Gaia DR3	LAMOST ID	α	δ	$\varpi \pm \sigma_{\varpi}$	System	libnor36	libr18	libr18_225
1872468615652420864	J205254.33+375751.7	313.226	37.964	0.778 ± 0.015	Roslund 7	B8 IV	B8 V	kB9hF0mK0 Eu
1872455180994495744	J205318.15+375115.6	313.326	37.854	0.747 ± 0.014	Roslund 7	A9 mB8 V Lam Boo	B9 IV	kB9hA9mK0 Eu
1872477166917054976	J205419.26+375621.9	313.58	37.939	0.834 ± 0.017	Roslund 7	A1 V	A0 V	kA1hA3mK0 Eu
1872491155642932352	J205451.44+381753.9	313.714	38.298	0.788 ± 0.026	Roslund 7	B8 III-IV	B8 III-IV	kB8hF1mG9 Eu
1969549204548089472	J210423.13+420437.5	316.096	42.077	0.505 ± 0.016	FoF 876	A0 IV-V Eu	A1 IV-V	kA1hA3mK0 Eu
2170794879372771200	J212658.92+485921.4	321.745	48.989	0.438 ± 0.015	UBC 156	A0 IV-V	A0 IV-V Si	A1 IV-V
1968023352983317632	J213335.60+441148.1	323.398	44.197	0.696 ± 0.011	HSC 703	A8 mB9 V Lam Boo	B9 V	kB9hA3mG9
1967518642782379136	J213354.32+420926.4	323.476	42.157	1.232 ± 0.012	HSC 696	A0 V	A0 V	A3 mA0 V Lam Boo
1979250470521255424	J214103.58+503109.8	325.265	50.519	0.241 ± 0.019	CWNU 1287	B9.5 II-III	A0 II-III	kA0hF0mA5 Eu
2007069351654097664	J225100.01+570219.6	342.75	57.039	0.297 ± 0.011	HSC 833	kB9.5hF0mG2 Eu	B9 II-III	kA0hF0mG8 Eu
2007098316914234624	J225100.44+571208.0	342.752	57.202	0.303 ± 0.02	HSC 833	A1 II-III	A1 II-III	kA1hF0mA4 Eu
2002643198873911040	J225259.05+541518.9	343.246	54.255	0.39 ± 0.013	UBC 172	A1 V	A1 V	kA1hA3mK0
2002643576831036288	J225324.65+541801.6	343.353	54.3	0.408 ± 0.013	UBC 172	A1 V	A1 V	kA2hA3mK0
1989227164148253440	J225540.79+511036.9	343.92	51.177	0.686 ± 0.011	UBC 6	?	F1 V Sr	F0 V SrSiEu
2010670870703164416	J231008.17+585833.4	347.534	58.976	0.643 ± 0.015	Theia 2902	B9 V	B9 V	kB9hA3mK2
1942267572276004096	J231021.34+471701.7	347.588	47.284	1.378 ± 0.018	Theia 401	kA2hA8mF3 Si	kA2hA7mF5 Si	kA2hA8mF4 Si
1941457026048083456	J231344.75+465257.9	348.436	46.883	1.389 ± 0.019	Theia 401	kA3hF5mK0	A3 IV-V	kA3hA3mK0
1942364054422427264	J232020.89+480552.9	350.087	48.098	1.426 ± 0.019	Theia 401	kA2hF5mK0	A2 V	kA2hA3mK0
1997352035379286144	J232959.83+543048.3	352.499	54.513	1.09 ± 0.014	UPK 214	A2 V Si	A1 V Si	kA2hA3mA5 Si
1994397411416991232	J233807.05+543557.7	354.529	54.599	1.034 ± 0.018	UPK 214	B9 V	B9 V	kA0hA3mK1

B.2. CP stars from Δa photometry

Table B.2.: CP stars detected via Δa photometry with their basic astrometric properties. The columns are as follows: (1) *Source*: the *Gaia* DR3 ID, (2) α: the right ascension in degrees, (3) β: the declination in degrees, (4) ϖ: the parallax and its error σ_ϖ, (5) *System*: The cluster or association the star belongs to, (6) The colour $(g_1 - y)$ from the synthetic photometry, (7) Δa: the Δa value from the photometry. The stars are sorted by their right ascension α.

Source	α	δ	$\varpi \pm \sigma_\varpi$	System	$(g_1 - y)$	Δa
5436414262899903872	144.758	-36.896	0.227 ± 0.044	HSC 2138	15.122	1.707
2930678291716664192	110.647	-18.713	0.251 ± 0.042	FSR 1252	11.584	2.208
461829660022360832	50.986	59.24	0.953 ± 0.015	Theia 1722	10.614	1.777
5960713736908382336	265.155	-40.215	0.673 ± 0.039	Trumpler 29	11.36	1.423
5881393391868603264	226.247	-55.643	0.523 ± 0.014	NGC 5823	9.197	2.32
5881395625251644288	226.379	-55.536	0.566 ± 0.013	NGC 5823	9.957	2.022
5881396037568526336	226.393	-55.515	0.526 ± 0.013	NGC 5823	9.775	1.319
5881345799292540288	226.371	-55.671	0.542 ± 0.013	NGC 5823	9.324	1.371
5881345837987362304	226.387	-55.669	0.593 ± 0.013	NGC 5823	9.113	1.46
5881348414936867584	226.425	-55.581	0.526 ± 0.017	NGC 5823	9.096	1.444
200085728707316096	73.536	40.35	0.932 ± 0.024	HSC 1284	12.231	1.547
4145604723045931136	273.091	-16.472	0.539 ± 0.021	OC 0025	9.862	1.503
5716196751916693760	114.074	-20.58	0.362 ± 0.029	NGC 2421	11.456	1.89
5716196958080774144	114.015	-20.578	0.344 ± 0.043	NGC 2421	11.495	1.698
5715446026000379264	114.086	-20.613	0.405 ± 0.038	NGC 2421	10.768	1.602
436077895107052928	45.559	47.929	0.394 ± 0.038	UBC 1246	11.529	1.429
436088684064785664	45.472	48.101	0.275 ± 0.043	UBC 1246	11.257	1.591
1870942218639565696	312.984	37.477	0.797 ± 0.017	Roslund 7	12.453	1.41
6071466104392664064	186.029	-58.125	0.389 ± 0.024	NGC 4337	11.567	1.583
5520069849191410304	124.238	-44.843	0.055 ± 0.037	OC 0473	10.916	1.468
5520118060206928896	123.822	-44.762	0.103 ± 0.042	OC 0473	10.9	1.543
2031866259474583552	297.863	29.863	0.279 ± 0.029	UBC 1072	12.299	1.852
2031875570964461440	297.845	29.931	0.209 ± 0.029	UBC 1072	10.213	1.393
2028868441028209152	297.991	29.824	0.184 ± 0.022	UBC 1072	9.266	1.895
5538870093575745280	117.995	-38.529	0.662 ± 0.019	NGC 2477	12.006	2.013
2012495574667667712	353.383	61.114	0.318 ± 0.017	UBC 400	10.647	1.437
5626334697376896000	131.133	-35.926	0.352 ± 0.023	Ruprecht 68	9.779	1.46
3129234045689550976	101.5	4.666	0.137 ± 0.035	CWNU 2178	11.087	1.381
3129257582110085888	101.66	4.936	0.193 ± 0.038	CWNU 2178	9.408	1.91
3032866112126207616	110.428	-12.984	0.306 ± 0.035	PHOC 36	9.371	1.699
3344069645563997568	93.448	12.812	0.233 ± 0.046	NGC 2194	9.605	1.623
3344069718583238400	93.438	12.826	0.288 ± 0.031	NGC 2194	11.003	1.839
3126748977611495936	99.689	2.04	0.405 ± 0.042	Collinder 110	7.623	1.387
2071023544997804032	307.073	45.517	0.353 ± 0.026	HSC 650	10.65	1.309
193724435465364864	81.849	39.747	0.218 ± 0.044	HSC 1322	8.039	1.415
2929941137888326144	109.237	-20.528	0.265 ± 0.046	UBC 454	11.415	1.893
2058950666823409152	302.678	35.881	0.574 ± 0.019	Gulliver 17	10.949	1.353
2004507661367254656	331.939	53.07	0.345 ± 0.039	FSR 0342	11.77	1.767
5545788117660638464	121.701	-34.481	0.288 ± 0.02	UBC 1425	9.963	1.491
5545788701776295040	121.587	-34.475	0.332 ± 0.016	UBC 1425	10.173	1.943

Continued on next page

Table B.2.: (continued)

Source	α	δ	$\varpi \pm \sigma_\varpi$	System	$(g_1 - y)$	Δa
5545818422951131136	121.73	-34.234	0.267 ± 0.024	UBC 1425	10.256	1.551
3032315016284058240	108.885	-14.181	0.102 ± 0.04	HSC 1802	9.519	1.39
3032615320394832128	109.767	-14.306	0.186 ± 0.06	HSC 1802	9.504	1.572
3031483579335538432	109.67	-14.606	0.069 ± 0.043	HSC 1802	10.187	2.164
3032256742166503552	109.189	-14.307	0.211 ± 0.03	HSC 1802	9.739	1.39
3032694794471084928	109.58	-13.808	0.216 ± 0.048	HSC 1802	8.906	2.223
5615380159954760064	113.423	-23.918	0.147 ± 0.055	OC 0412	11.716	1.375
2954056279739902464	102.276	-10.527	0.173 ± 0.041	Ruprecht 4	7.894	1.544
2954056966935503488	102.206	-10.497	0.23 ± 0.03	Ruprecht 4	9.278	1.816
524243471939039104	13.432	64.762	0.388 ± 0.013	FSR 0519	7.895	1.531
3038044846244519040	119.988	-10.767	0.234 ± 0.049	NGC 2506	11.189	2.334
5335935942551982080	172.616	-60.775	0.206 ± 0.024	Ruprecht 164	10.513	1.454
5335948105906487808	172.59	-60.745	0.244 ± 0.032	Ruprecht 164	11.188	1.682
5335948110260706944	172.603	-60.746	0.175 ± 0.039	Ruprecht 164	11.628	2.24
5335948247699690624	172.608	-60.726	0.188 ± 0.024	Ruprecht 164	12.803	1.394
3015914151077821440	86.907	-7.126	1.973 ± 0.02	Theia 6046	9.575	2.141
3209125350833404416	80.997	-6.157	0.86 ± 0.023	Theia 6046	12.187	1.703
3010537504859395456	84.296	-10.447	0.479 ± 0.029	Theia 6046	13.231	1.951
5518730442165840768	119.37	-46.929	0.567 ± 0.022	HSC 2097	11.461	1.4
1995013958260475392	359.452	56.726	0.484 ± 0.022	NGC 7789	12.726	1.723
1995013962565654784	359.456	56.724	0.483 ± 0.016	NGC 7789	11.365	1.483
5343948569131942656	177.723	-55.658	0.393 ± 0.027	NGC 3960	12.059	1.651
2055676974020815488	303.412	34.409	0.62 ± 0.015	Theia 2007	10.247	1.39
546642482291623168	36.909	72.641	1.145 ± 0.017	FSR 0569	9.732	1.421
4252282918995359744	282.252	-7.329	0.408 ± 0.031	UBC 1569	11.457	1.826
5865403400411966848	205.209	-62.976	0.439 ± 0.018	HSC 2600	10.947	1.517
2004591018090104064	333.9	53.785	0.295 ± 0.043	UBC 164	11.546	1.713
2004662761226303616	333.724	54.196	0.304 ± 0.029	UBC 164	9.235	1.355
2004978389778437632	334.436	54.161	0.234 ± 0.035	UBC 164	10.906	1.377
5336318302079147520	174.384	-59.382	0.556 ± 0.016	UBC 277	8.855	2.004
5338808317943793920	163.587	-59.14	0.209 ± 0.028	CWNU 2232	9.994	1.62
5338432559848222720	163.417	-59.354	0.227 ± 0.027	CWNU 2232	10.403	1.903
5548324381750261376	123.868	-30.835	0.324 ± 0.038	Haffner 26	11.922	1.399
5548310672214702720	123.913	-30.946	0.324 ± 0.038	Haffner 26	12.309	1.663
428891315316060160	6.281	61.34	0.257 ± 0.03	NGC 103	14.308	1.889
5337929224037553408	165.938	-61.414	0.466 ± 0.026	Ruprecht 93	8.877	1.619
5337935541885338880	166.025	-61.349	0.467 ± 0.035	Ruprecht 93	13.899	3.105
4145751198607788800	274.149	-15.728	0.358 ± 0.023	Theia 1666	9.132	1.324
5886764849763477248	228.565	-54.511	0.475 ± 0.016	CWNU 19	10.292	1.845
505233328211347328	31.38	57.763	0.419 ± 0.031	UBC 1577	11.699	1.581
5547698725276137088	121.764	-32.633	0.525 ± 0.021	CWNU 2065	11.748	1.539
5254321466521773824	158.839	-60.691	0.168 ± 0.034	HSC 2363	16.408	2.596
5254321535241240704	158.811	-60.682	0.146 ± 0.036	HSC 2363	11.62	1.841
3372129324042848000	97.096	18.865	0.2 ± 0.046	Theia 2725	9.164	1.304
3125525015011266304	101.237	0.355	0.164 ± 0.044	Dolidze 25	9.89	1.511
2931333566285206912	109.835	-18.951	0.306 ± 0.034	UBC 634	11.465	1.505
5867067202014937984	208.751	-61.776	0.648 ± 0.023	NGC 5316	11.275	1.356
2028730486687781248	297.445	29.252	0.293 ± 0.022	Theia 5724	10.21	1.397
205547690157197184	75.465	43.878	0.294 ± 0.028	UBC 1270	11.272	1.34

Continued on next page

Table B.2.: (continued)

Source	α	δ	$\varpi \pm \sigma_\varpi$	System	$(g_1 - y)$	Δa
6054102754229605376	182.289	-63.584	0.396 ± 0.029	UBC 517	12.527	1.747
6054029567979605632	182.4	-63.97	0.427 ± 0.03	UBC 517	10.858	1.31
5597788180070424960	119.771	-28.544	0.152 ± 0.034	Ruprecht 44	10.167	1.856
2164328273542938880	317.575	46.758	0.177 ± 0.036	Teutsch 157	11.318	2.349
2164369672703828224	317.458	46.764	0.186 ± 0.028	Teutsch 157	10.035	1.315
422489030905349504	2.464	57.995	0.28 ± 0.025	UBC 1195	10.111	1.761
5990519611687962368	245.337	-45.232	0.779 ± 0.022	Theia 1907	10.56	1.41
423708664179545344	12.125	55.781	0.232 ± 0.037	CWNU 1697	13.239	1.435
4253531787996372480	281.054	-5.695	0.264 ± 0.022	HSC 273	10.049	1.469
5619279474861298304	114.135	-21.442	0.287 ± 0.041	Theia 3849	12.365	2.174
5619305897500780672	113.763	-21.445	0.353 ± 0.024	Theia 3849	10.203	1.386
5619234704120799616	114.099	-21.821	0.351 ± 0.038	Theia 3849	12.14	1.752
5619245974115290496	113.802	-21.725	0.285 ± 0.053	Theia 3849	8.469	2.507
6054273556477806976	180.907	-63.673	0.427 ± 0.028	CWNU 2700	11.783	1.771
6054329940813382016	180.665	-63.482	0.444 ± 0.026	CWNU 2700	12.14	1.404
2005079922809260160	334.948	54.851	0.248 ± 0.035	UBC 1159	11.512	1.51
2005158984565628800	335.375	54.85	0.285 ± 0.032	UBC 1159	9.656	1.689
5311736829814744320	137.447	-53.226	0.477 ± 0.03	UBC 249	13.457	1.502
5311361380957241600	137.237	-53.306	0.526 ± 0.026	UBC 249	13.214	2.36
2202870691566972032	331.293	59.686	0.155 ± 0.035	Theia 4560	11.404	1.946
5352752977223417088	163.002	-55.883	0.375 ± 0.042	UBC 500	11.827	1.93
5352768404745712640	162.928	-55.712	0.362 ± 0.029	UBC 500	12.101	1.367
5856527558444963200	189.474	-68.39	0.329 ± 0.031	Collinder 261	15.131	2.138
5856528761035882496	189.489	-68.334	0.323 ± 0.025	Collinder 261	12.07	1.309
5967636541310787584	250.065	-43.354	0.621 ± 0.015	NGC 6192	11.279	2.027
2178496541693778688	325.13	57.758	1.032 ± 0.012	HSC 764	10.956	2.358
3344712726726459520	94.79	14.522	0.25 ± 0.024	UBC 1316	11.134	1.357
419056046364926848	6.098	52.7	0.571 ± 0.029	Theia 2936	12.133	1.458
2952472020922535680	100.406	-13.283	0.759 ± 0.018	Theia 1769	11.596	1.341
5942553897951002624	250.45	-47.45	0.371 ± 0.017	UBC 1551	10.53	1.533
1824774481337240576	297.491	19.72	0.255 ± 0.037	UBC 1064	17.954	2.381
3109065497745193856	105.509	-1.879	0.255 ± 0.043	HSC 1702	11.611	1.342
3099227170779840640	104.033	-7.181	0.391 ± 0.029	NGC 2309	11.302	1.456
1981253265315002880	329.649	52.816	0.254 ± 0.018	HSC 765	9.681	1.346
182432790350312832	81.94	33.284	0.313 ± 0.054	HXWHB 10	15.327	2.165
182448703206243328	81.754	33.368	0.322 ± 0.043	HXWHB 10	11.016	2.163
5249113835804073856	146.999	-65.212	0.491 ± 0.026	Ruprecht 84	11.206	1.324
5712163502755233152	117.23	-21.326	0.309 ± 0.042	NGC 2455	10.407	2.348
5712177006132352512	117.23	-21.212	0.356 ± 0.033	NGC 2455	11.38	1.498
2005010722293609600	335.473	54.524	0.644 ± 0.019	Theia 4535	12.449	1.314
3432293290346203776	95.389	26.923	0.473 ± 0.032	Gulliver 56	12.392	2.156
5859013073202953856	197.142	-64.753	0.456 ± 0.042	Theia 2478	12.642	1.907
429382934455215360	0.413	60.918	0.277 ± 0.031	UBC 406	11.931	2.591
5338495403810748416	166.244	-59.864	0.381 ± 0.025	Feinstein 1	11.699	1.488
5338502202699086080	166.582	-59.639	0.351 ± 0.03	Feinstein 1	11.113	2.256
2002647047164565760	343.304	54.35	0.376 ± 0.023	UBC 172	11.429	1.341
4065828252486319232	272.386	-24.551	0.766 ± 0.032	ESO 521-38	12.537	1.534
5547978963304967296	123.697	-31.97	0.29 ± 0.049	Ruprecht 58	11.921	2.99
5852249564919229696	207.146	-64.687	0.403 ± 0.02	NGC 5288	11.389	1.404

Continued on next page

Table B.2.: (continued)

Source	α	δ	$\varpi \pm \sigma_{\varpi}$	System	$(g_1 - y)$	Δa
5546093541375220480	121.521	-33.418	0.284 ± 0.022	Theia 5150	12.178	2.576
5547599769226387840	121.869	-33.253	0.208 ± 0.024	Theia 5150	10.273	2.069
5547617464491681280	121.696	-33.067	0.258 ± 0.031	Theia 5150	12.019	1.7
4064497976508146688	269.955	-24.693	0.366 ± 0.023	Ruprecht 138	11.065	2.775
4064498221358869632	270.002	-24.672	0.408 ± 0.021	Ruprecht 138	10.701	1.781
5932321396155218048	244.525	-53.465	0.287 ± 0.031	UBC 310	12.336	1.639
5537397916227924480	118.726	-40.309	0.498 ± 0.022	OC 0448	12.117	1.897
465827037629837696	41.209	62.344	0.279 ± 0.02	Czernik 13	8.921	2.569
5857554674110096128	199.424	-67.081	0.365 ± 0.03	Collinder 268	11.079	1.391
5865028948036956288	202.858	-63.641	0.492 ± 0.035	Theia 3381	13.418	1.656
5865056126594144128	203.062	-63.234	0.375 ± 0.03	Theia 3381	10.429	1.755
5351416585238144384	158.397	-58.571	0.16 ± 0.037	ASCC 60	12.425	3.2
3424065129438776320	89.614	22.093	0.527 ± 0.015	UBC 437	9.68	1.361
3451181834969524992	88.064	32.562	0.716 ± 0.031	NGC 2099	11.448	1.46
5333358343707886336	175.894	-62.504	0.396 ± 0.022	Stock 14	9.371	1.635
3051554957937264128	105.848	-8.409	1.007 ± 0.019	NGC 2323	10.443	1.418
6056513914499972992	189.956	-60.713	0.176 ± 0.048	Trumpler 20	8.575	3.111
6056527417878920960	190.075	-60.587	0.265 ± 0.019	Trumpler 20	11.416	1.813
6056528517390393216	189.832	-60.628	0.28 ± 0.033	Trumpler 20	13.574	3.447
6056528822281714816	189.859	-60.612	0.235 ± 0.032	Trumpler 20	10.509	1.441
6056528895347572352	189.835	-60.608	0.259 ± 0.035	Trumpler 20	12.626	1.754
6056529921800435328	189.832	-60.56	0.3 ± 0.038	Trumpler 20	10.687	1.694
6056530162318616320	189.938	-60.596	0.267 ± 0.04	Trumpler 20	9.55	2.518
3051138071233295488	103.547	-7.807	0.227 ± 0.046	CWNU 1973	10.825	3.142
3051142842935888512	103.515	-7.754	0.207 ± 0.034	CWNU 1973	13.233	2.045
5547527132743054336	122.755	-32.902	0.098 ± 0.036	HSC 2016	11.294	2.585
5547742155982010368	122.613	-32.499	0.109 ± 0.015	HSC 2016	9.288	1.471
5547576198450681728	122.957	-32.444	0.107 ± 0.048	HSC 2016	13.894	2.147
209190161723478656	81.509	46.479	0.194 ± 0.053	NGC 1883	12.423	1.503
5335936531026860288	172.873	-60.81	0.187 ± 0.044	UBC 276	10.462	1.981
4056408628951629696	267.652	-30.214	0.36 ± 0.024	NGC 6451	9.678	1.424
4064449842844939648	269.552	-25.25	0.353 ± 0.026	CWNU 488	9.584	1.524
3045751220171075968	106.736	-11.957	0.592 ± 0.024	Theia 2289	12.258	1.312
2085345164980708096	300.816	46.333	0.45 ± 0.014	FSR 0241	12.008	2.719
5352919209641887744	161.4	-55.634	0.348 ± 0.033	HSC 2340	11.258	2.1
5352859973448858240	161.979	-55.833	0.382 ± 0.023	HSC 2340	10.253	1.603
5352004244161147136	159.746	-56.806	0.347 ± 0.03	HSC 2340	12.582	1.543
5352046021282020096	158.816	-56.723	0.423 ± 0.04	HSC 2340	15.075	4.62
5352139415372672512	159.52	-55.989	0.383 ± 0.012	HSC 2340	9.763	1.387
5351270182715362176	161.332	-57.059	0.388 ± 0.04	HSC 2340	10.665	1.668
5351221941647302912	159.852	-57.299	0.389 ± 0.022	HSC 2340	13.079	1.344
5351231459296329728	160.398	-57.209	0.335 ± 0.031	HSC 2340	14.162	1.49
5351303202425996544	161.479	-56.75	0.435 ± 0.03	HSC 2340	10.718	1.606
5351241973377009280	160.526	-56.969	0.418 ± 0.031	HSC 2340	11.132	1.748
5352450199210439680	158.344	-55.025	0.408 ± 0.041	HSC 2340	12.173	1.786
5352458548628393856	157.749	-55.389	0.418 ± 0.028	HSC 2340	11.782	1.598
5352188515442104832	159.275	-55.887	0.39 ± 0.028	HSC 2340	10.69	1.499
5352424017090200960	158.565	-55.399	0.449 ± 0.035	HSC 2340	12.754	1.716
5353771021913154048	160.004	-54.764	0.419 ± 0.035	HSC 2340	11.996	1.534

Continued on next page

Table B.2.: (continued)

Source	α	δ	$\varpi \pm \sigma_{\varpi}$	System	$(g_1 - y)$	Δa
4062904784444570368	270.885	-27.902	0.519 ± 0.039	NGC 6520	10.209	1.769
4062905712160484352	270.855	-27.866	0.56 ± 0.045	NGC 6520	11.555	1.991
3352218504196934784	99.187	12.442	0.249 ± 0.028	HSC 1593	11.343	2.201
3352222215048693504	99.029	12.452	0.192 ± 0.038	HSC 1593	10.03	1.577
3352129065796751360	99.514	11.981	0.185 ± 0.034	HSC 1593	9.673	1.936
3352166728369846784	98.961	11.991	0.167 ± 0.041	HSC 1593	8.546	1.429
3355188117603280640	98.319	12.219	0.239 ± 0.032	HSC 1593	8.67	1.313
3355218732129849088	98.825	12.441	0.246 ± 0.036	HSC 1593	10.821	1.459
3355244879890630144	98.724	12.732	0.245 ± 0.047	HSC 1593	10.512	2.317
5329369972661944064	130.645	-47.215	0.308 ± 0.041	NGC 2660	10.011	3.179
5329370144460683392	130.688	-47.19	0.357 ± 0.025	NGC 2660	11.196	1.371
5715306662901791232	115.644	-20.679	0.226 ± 0.053	HSC 1886	12.44	2.115
3128813203316883456	105.088	5.289	0.265 ± 0.05	UBC 1335	11.781	1.317
5639492896622948352	130.843	-32.687	0.218 ± 0.035	NGC 2658	12.537	1.363
5639492965342430976	130.825	-32.679	0.261 ± 0.041	NGC 2658	12.465	1.455
5639495233085140480	130.837	-32.645	0.196 ± 0.04	NGC 2658	11.159	1.393
2922489850666603904	104.292	-23.494	0.111 ± 0.046	HSC 1860	10.527	1.697
3373908780534025984	95.134	19.034	0.213 ± 0.052	HSC 1520	10.295	1.588
3373961969408420480	95.326	19.529	0.231 ± 0.041	HSC 1520	9.342	1.877
434876438137982080	48.801	47.205	0.287 ± 0.038	NGC 1245	11.916	1.652
435064214109973248	48.787	47.244	0.336 ± 0.043	NGC 1245	11.778	1.865
435064248469710976	48.812	47.238	0.34 ± 0.043	NGC 1245	13.555	2.701
435064695146351104	48.706	47.236	0.255 ± 0.03	NGC 1245	10.658	1.506
435065244902089856	48.746	47.286	0.32 ± 0.047	NGC 1245	10.982	1.573
435067993681192320	48.654	47.283	0.289 ± 0.039	NGC 1245	11.447	1.383
5310687242880002048	139.208	-54.174	0.229 ± 0.041	UBC 252	11.684	1.702
5310687208537111296	139.211	-54.182	0.14 ± 0.032	UBC 252	10.626	1.502
5310688514207181824	139.249	-54.177	0.169 ± 0.027	UBC 252	10.872	1.31
5310688892164338816	139.265	-54.12	0.16 ± 0.028	UBC 252	9.624	1.371
5310690197834199936	139.131	-54.164	0.222 ± 0.032	UBC 252	12.719	1.756
5310690610151080704	139.129	-54.118	0.199 ± 0.029	UBC 252	11.062	1.338
5310691537863997568	139.034	-54.111	0.175 ± 0.039	UBC 252	10.023	2.808
5339893982590700800	168.742	-57.593	0.403 ± 0.037	Trumpler 19	14.72	1.989
5339894291828433024	168.76	-57.561	0.418 ± 0.027	Trumpler 19	11.824	1.363
5339935145550924544	168.632	-57.579	0.382 ± 0.046	Trumpler 19	12.944	2.477
5339935282997261568	168.585	-57.577	0.375 ± 0.03	Trumpler 19	10.354	1.431
5339935351709362688	168.625	-57.573	0.395 ± 0.025	Trumpler 19	13.457	1.93
5339935553544026880	168.516	-57.605	0.36 ± 0.041	Trumpler 19	11.237	1.786
5339935695306646016	168.517	-57.585	0.338 ± 0.033	Trumpler 19	11.025	1.376
5339941051096276608	168.635	-57.551	0.378 ± 0.033	Trumpler 19	13.691	1.375
5339941124145690752	168.696	-57.552	0.43 ± 0.025	Trumpler 19	12.377	1.523
5339942189297580416	168.559	-57.504	0.438 ± 0.037	Trumpler 19	11.46	1.481
5595806963197638784	120.711	-32.088	0.267 ± 0.028	Ruprecht 48	12.584	1.391
5337166162957067648	166.717	-61.606	0.164 ± 0.024	BH 110	10.221	1.331
3374387377328457728	91.787	19.023	0.464 ± 0.021	FSR 0904	11.432	1.799
506562637767384704	28.166	59.608	0.335 ± 0.016	UBC 1229	9.441	1.803
3056679231876595584	116.706	-4.683	0.188 ± 0.036	Berkeley 39	11.581	1.626
4057397540947144320	267.434	-28.776	0.441 ± 0.029	Collinder 351	9.536	1.361
5254326409970732288	158.783	-60.606	0.384 ± 0.036	Theia 3409	14.856	2.289

Continued on next page

Table B.2.: (continued)

Source	α	δ	$\varpi \pm \sigma_{\varpi}$	System	$(g_1 - y)$	Δa
5254330709292306560	159.336	-60.648	0.366 ± 0.03	Theia 3409	12.706	2.484
5254332770876859008	159.387	-60.574	0.351 ± 0.034	Theia 3409	15.331	1.693
5254346274255285120	159.017	-60.581	0.365 ± 0.03	Theia 3409	11.712	2.768
5306893687257430912	140.465	-56.307	0.227 ± 0.025	Ruprecht 75	10.792	1.337
1989232043231063424	344.043	51.176	0.686 ± 0.02	UBC 6	11.693	1.625
186277816870697728	74.509	36.424	0.163 ± 0.058	HSC 1317	7.533	2.452
186412614417949056	75.44	36.247	0.103 ± 0.049	HSC 1317	10.253	1.463
3032169365352898688	108.364	-14.714	0.439 ± 0.035	CWNU 2677	10.303	2.289
5334206724330377216	174.044	-61.669	0.474 ± 0.036	NGC 3766	9.745	1.38
5334208682835591936	174.144	-61.597	0.433 ± 0.029	NGC 3766	10.096	1.53
5334208815944175744	174.144	-61.568	0.453 ± 0.039	NGC 3766	9.893	1.629
5334209060792840832	174.062	-61.548	0.488 ± 0.038	NGC 3766	12.111	2.213
464638293759397632	44.557	60.558	0.392 ± 0.02	SAI 24	10.566	1.471
3324289470039249408	97.412	6.845	0.323 ± 0.038	NGC 2236	8.644	1.507
246658739159868928	59.055	47.45	0.328 ± 0.018	UBC 1259	8.897	1.683
5239709953387908352	160.574	-65.072	0.464 ± 0.026	Melotte 101	14.036	1.818
5239710674942399616	160.5	-65.057	0.426 ± 0.023	Melotte 101	12.484	1.323
5239687099840634112	160.521	-65.091	0.465 ± 0.038	Melotte 101	12.229	4.262
5333062854296532480	178.038	-63.385	0.256 ± 0.021	LISC 1273	11.025	1.869
5334785136200822528	177.821	-61.469	0.481 ± 0.025	OC 0571	11.564	1.572
3358875948321624192	99.146	16.933	0.188 ± 0.029	HSC 1552	11.696	1.417
5256514751685273984	151.593	-60.291	0.281 ± 0.034	Trumpler 12	15.145	1.876
5256514786045038208	151.605	-60.28	0.28 ± 0.037	Trumpler 12	15.098	2.253
5256515576318991744	151.55	-60.271	0.272 ± 0.033	Trumpler 12	11.532	1.596
3029944469213585024	114.604	-14.88	0.259 ± 0.036	NGC 2425	11.833	1.305
5308609990548375552	147.806	-53.091	0.386 ± 0.017	Pismis 16	9.1	2.429
5337376891236690560	170.448	-61.275	0.478 ± 0.021	HSC 2429	10.663	1.388
5334368386895099904	171.078	-61.337	0.428 ± 0.024	HSC 2429	12.573	1.802
5333220354993835776	175.829	-63.125	0.421 ± 0.028	CWNU 2419	11.214	1.987
5338536394982790144	165.674	-59.701	0.368 ± 0.028	CWNU 2487	10.594	1.491
5338487260551899776	165.718	-59.812	0.39 ± 0.026	CWNU 2487	10.909	1.418
2071126555487650560	308.984	45.664	0.35 ± 0.014	HSC 655	9.329	2.233
2085733430021785856	301.066	46.773	0.313 ± 0.04	UBC 586	9.669	1.437
2015462885981225984	351.463	61.377	0.365 ± 0.019	Czernik 43	10.698	1.301
5339377246496587392	167.65	-59.014	0.43 ± 0.034	Basel 17	13.318	2.04
5891975950758743424	215.702	-58.035	0.572 ± 0.027	HXHWL 14	11.147	1.551
3444725983719985536	87.542	30.365	0.293 ± 0.048	UBC 1290	12.981	2.261
458367607151538048	34.834	57.045	0.413 ± 0.027	NGC 869	10.615	1.576
5334361824184308352	170.69	-61.522	0.266 ± 0.014	OC 0562	8.984	1.695
3058087534475502464	110.491	-6.441	0.259 ± 0.051	UBC 1356	13.09	1.399
5862122251606549504	196.647	-63.922	0.404 ± 0.015	UBC 525	10.075	1.4
427379349388662144	11.963	61.36	0.409 ± 0.018	UBC 1207	10.298	1.327
5528500496331078784	129.123	-40.152	1.268 ± 0.014	Theia 274	14.689	1.957
3124537309971018752	94.768	2.121	0.405 ± 0.028	CWNU 1313	10.817	1.433
3355202857930984448	98.321	12.34	0.459 ± 0.031	Theia 2133	11.766	1.335
3047223466244103808	109.868	-9.943	0.31 ± 0.036	CWNU 2284	13.569	1.756
3047235560871866368	109.462	-9.904	0.324 ± 0.042	CWNU 2284	12.821	1.827
6054914468674507264	186.146	-61.86	0.505 ± 0.019	NGC 4349	12.804	1.355
6054918488763944832	185.953	-61.803	0.536 ± 0.034	NGC 4349	13.922	1.42

Continued on next page

Table B.2.: (continued)

Source	α	δ	$\varpi \pm \sigma_{\varpi}$	System	$(g_1 - y)$	Δa
6054918999820117632	186.049	-61.764	0.476 ± 0.04	NGC 4349	11.376	2.542
6054867189673550080	186.167	-61.909	0.496 ± 0.023	NGC 4349	11.484	1.713
6054868770221377920	186.237	-61.873	0.49 ± 0.045	NGC 4349	11.503	2.717
5977181126903472256	256.845	-35.614	0.964 ± 0.017	OC 0684	10.132	2.188
3351080754475343616	100.724	11.147	0.183 ± 0.046	HSC 1600	12.182	1.744
2060806986047441536	302.747	37.514	1.17 ± 0.013	ASCC 111	11.665	1.388
5240688931053087488	169.867	-63.456	0.399 ± 0.025	Melotte 105	11.629	1.575
464761542138326656	42.669	60.389	0.462 ± 0.017	IC 1848	9.848	1.593
5601940245213539456	117.99	-26.825	0.185 ± 0.044	HSC 1954	11.42	1.472
3372482228617562752	96.22	19.875	0.201 ± 0.042	Bochum 1	10.869	2.069
5339411846756340736	167.978	-58.634	0.313 ± 0.037	Stock 13	13.286	1.913
3126379163747692672	102.252	2.168	0.138 ± 0.041	Alessi 59	9.569	1.717
3126387135207429376	102.54	2.295	0.16 ± 0.05	Alessi 59	10.361	1.349
3114062022175576960	103.057	1.44	0.3 ± 0.039	Alessi 59	8.873	1.468
3114069340800329344	103.256	1.36	0.251 ± 0.035	Alessi 59	9.107	1.461
3114197807563542528	103.801	1.921	0.216 ± 0.04	Alessi 59	10.671	1.409
3046665459786060160	107.045	-9.87	0.841 ± 0.02	Theia 1654	9.429	1.524
2931458360855681408	110.714	-18.392	0.332 ± 0.039	CWNU 2259	10.342	1.491
2931478907978887424	110.528	-18.233	0.295 ± 0.041	CWNU 2259	10.309	2.457
3373664650293368448	93.453	18.793	0.407 ± 0.034	IRAS 06117+1901	10.64	1.301
3429607806213773824	90.288	25.562	0.134 ± 0.037	HSC 1464	10.004	1.439
3325952618815570176	98.95	7.675	0.409 ± 0.023	NGC 2254	9.336	1.396
183561855647646592	80.476	34.747	0.293 ± 0.041	UBC 1281	10.717	1.31
5619286449887793536	114.015	-21.304	0.348 ± 0.039	UBC 460	11.318	1.476
5619306619055311360	113.731	-21.431	0.298 ± 0.036	UBC 460	11.307	1.668
5619308130883674112	113.859	-21.356	0.312 ± 0.044	UBC 460	12.102	1.755
3046127077049839232	106.778	-11.887	0.329 ± 0.032	HSC 1770	11.386	2.076
3045760359861632128	106.406	-11.933	0.408 ± 0.036	HSC 1770	11.056	2.038
3045763933274289920	106.638	-11.914	0.322 ± 0.024	HSC 1770	10.914	1.361
5329162680360708736	130.917	-47.533	0.19 ± 0.03	CWNU 2422	7.42	1.701
5334606465552979840	177.728	-62.742	0.439 ± 0.033	UBC 280	11.409	1.377
505775043845225472	26.944	57.74	0.615 ± 0.022	ASCC 6	11.016	1.389
4145600363673344000	273.151	-16.553	0.606 ± 0.024	HSC 175	11.1	1.611
3047456425266457088	112.01	-9.414	0.264 ± 0.039	Theia 3048	10.346	2.965
5309269697522526976	145.454	-53.675	0.601 ± 0.018	Theia 3127	13.99	1.32
5308897478477703552	145.168	-53.722	0.601 ± 0.026	Theia 3127	11.694	1.382
253428535333057920	66.985	44.475	0.302 ± 0.025	UBC 1264	10.363	1.519
253436747311206528	67.277	44.408	0.35 ± 0.021	UBC 1264	9.823	2.014
5611755379356947072	112.933	-28.246	0.416 ± 0.022	UBC 233	12.051	1.393
5308756156872093312	144.294	-54.494	0.45 ± 0.026	BH 75	11.207	1.488
5619904272346555520	111.254	-21.138	0.332 ± 0.034	NGC 2384	12.801	2.398
469719102632116736	59.741	57.281	0.219 ± 0.044	FSR 0647	9.956	2.027
469666978907469440	59.998	57.152	0.202 ± 0.03	FSR 0647	12.507	1.648
2003954293466235008	341.759	56.389	0.278 ± 0.028	UBC 173	9.766	1.8
2003958008625588096	341.683	56.444	0.3 ± 0.025	UBC 173	9.615	1.741
210735559677409792	86.729	48.251	0.255 ± 0.048	HSC 1282	11.537	1.392
237904599374669312	51.466	41.84	0.855 ± 0.024	CWNU 405	12.205	1.304
3048063321325560960	108.841	-9.421	0.278 ± 0.035	FSR 1180	11.138	1.606
6057345351449944320	180.496	-63.249	0.406 ± 0.036	NGC 4052	10.501	1.53

Continued on next page

Table B.2.: (continued)

Source	α	δ	$\varpi \pm \sigma_{\varpi}$	System	$(g_1 - y)$	Δa
6053508880524960000	186.733	-64.065	0.364 ± 0.015	BH 132	10.751	1.875
5308309480289223168	148.856	-54.037	0.285 ± 0.034	UBC 1470	10.993	1.305
2059111848356956928	301.743	36.153	0.312 ± 0.025	Theia 4725	10.309	1.419
5429398661462465152	139.84	-40.526	0.176 ± 0.037	NGC 2849	10.937	1.304
2051293049345064832	290.249	37.774	0.19 ± 0.032	NGC 6791	12.25	1.972
2930145097297927296	109.454	-19.682	0.346 ± 0.035	HSC 1848	12.156	1.443
2930047653076294400	109.699	-20.192	0.301 ± 0.048	HSC 1848	12.383	1.797

B.3. CP stars from light curves

Table B.3.: Stars with light curves that show CP properties. The columns are (1) *Gaia* DR3 ID, (2) right ascension α in degrees, (3) declination β in degrees, (4) parallax ϖ and parallax error σ_ϖ, (5) the name of the association the star is in, designation from Kerr et al. (2021), (6) variable star type according to the VSX, (7) the FAP of the period, (8) the period of the variability.

Gaia DR3	TIC	α	β	$\varpi \pm \sigma_\varpi$	System	Type	$log(FAP)$	$P(d)$
3314527696567187584	17560109	67.283	18.455	4.531 ± 0.020	taur ori 4	ACV	$-\infty$	1.017
3238478566084270208	397061497	75.275	3.717	3.479 ± 0.048	taur ori 4	SXARI	$-\infty$	2.42
3207058750010997632	306345958	78.520	-7.917	3.728 ± 0.022	greater ori	ACV	-128.252	4.028
3213882697128481792	4070682	80.103	-3.510	3.181 ± 0.020	greater ori	SXARI	$-\infty$	1.043
3346259567786672384	247675468	86.855	12.648	3.351 ± 0.037	taur ori 4	ACV	$-\infty$	0.952
3346656590266363648	247763365	87.357	13.922	3.654 ± 0.030	taur ori 4	ACV	$-\infty$	0.382
3330219445485837184	436332628	91.617	10.750	5.555 ± 0.041	taur ori 2	SXARI	$-\infty$	0.362
3104244792087711360	42884620	97.045	-4.899	3.184 ± 0.045	mon sw	SXARI	$-\infty$	1.173
5514764057046837248	388354822	124.907	-50.382	3.128 ± 0.016	vela cg4	ACV	$-\infty$	1.439
5515989290962253184	82893704	125.065	-47.969	3.400 ± 0.020	vela cg4	ACV	-300.311	2.501
5322386214086050176	89943694	127.570	-50.941	3.082 ± 0.011	vela cg4	ACV	$-\infty$	1.463
5424236729248685824	77105310	141.327	-43.624	5.625 ± 0.012	ic 2391	ACV	$-\infty$	1.471
5232258082033470720	397732137	159.330	-69.363	4.652 ± 0.022	cha	ACV	-222.997	1.584
5239734932919731456	461125565	159.573	-65.042	6.606 ± 0.030	ic 2391	SXARI	$-\infty$	0.549
5239736204230183680	464907721	159.878	-65.083	6.652 ± 0.012	ic 2391	ACV	$-\infty$	0.86
4523888885382756224	50325659	278.215	17.303	3.179 ± 0.019	cerberus	SXARI	$-\infty$	2.99
2262275415015759872	229793060	284.719	69.531	5.115 ± 0.037	cep far north	ACV	$-\infty$	1.126
2254485134616928128	229954300	288.681	65.273	4.858 ± 0.031	cep far north	SXARI	$-\infty$	1.306
2301907242919520640	236003103	305.141	82.848	4.238 ± 0.022	cep far north	ACV	-306.611	1.323
2190139274622512128	429331590	313.699	57.611	3.012 ± 0.021	cep cyg	ACV	-220.353	1.417

B.4. CP stars with IR excess

Gaia DR3 ID	Filter where excess starts
182621906350208384	WISE/WISE.W4
183323227266520704	WISE/WISE.W4
183337177320364928	WISE/WISE.W1
1871158238309294208	WISE/WISE.W3
187964540726357632	WISE/WISE.W1
2007069351654097664	WISE/WISE.W1
2070344734000894592	WISE/WISE.W3
2075877648313310848	WISE/WISE.W1
2075877678366383744	WISE/WISE.W4
2076066351994581120	WISE/WISE.W4
2085246793048249344	WISE/WISE.W3
216590390373910912	Spitzer/IRAC.I4
216617641943232000	Spitzer/MIPS.24mu
251761469543936512	WISE/WISE.W3
253455576447809280	WISE/WISE.W4
3017409624342379520	WISE/WISE.W3
3019790754200699136	WISE/WISE.W1
3019875485316186752	WISE/WISE.W1
3125739694655670912	UKIRT/UKIDSS.K
3209504544905800576	WISE/WISE.W4
3210561587897894528	WISE/WISE.W4
3304135250100217600	WISE/WISE.W2
3330884473923251968	WISE/WISE.W4
3342955019950652928	WISE/WISE.W4
3355226737949262336	WISE/WISE.W4
3355241409558154368	WISE/WISE.W4
3370708239624841344	WISE/WISE.W3
3372437530897057920	WISE/WISE.W4
3372466874113370240	WISE/WISE.W4
3373851365410096896	WISE/WISE.W3
3373860500801601408	WISE/WISE.W3
3377260401211784448	WISE/WISE.W3
3377541841828979456	WISE/WISE.W4
3383565585001209728	WISE/WISE.W3
3383771812150964096	WISE/WISE.W3
3394744216639326208	WISE/WISE.W3
3444662212044370944	WISE/WISE.W3
3445205168927696512	WISE/WISE.W4
3455831880089411072	WISE/WISE.W3
3455880567838460544	WISE/WISE.W3
435065038743702528	WISE/WISE.W1
4469325071096213504	WISE/WISE.W3
458406742891002496	WISE/WISE.W1
473267192293775360	WISE/WISE.W1
48058592395097856	WISE/WISE.W3
1824774481337240576	WISE/WISE.W1
1981253265315002880	WISE/WISE.W3
2015462885981225984	WISE/WISE.W3

Table B.4 List of the CP Stars and candidates that show IR excess.

Gaia DR3 ID	Filter where excess starts
2028730486687781248	WISE/WISE.W4
2055676974020815488	WISE/WISE.W1
2058950666823409152	WISE/WISE.W4
2164328273542938880	UKIRT/UKIDSS.K
2178496541693778688	WISE/WISE.W3
2930678291716664192	WISE/WISE.W1
2931333566285206912	WISE/WISE.W1
2931478907978887424	WISE/WISE.W1
3051142842935888512	WISE/WISE.W4
3124537309971018752	WISE/WISE.W1
3125525015011266304	UKIRT/UKIDSS.K
3126379163747692672	WISE/WISE.W3
3126387135207429376	WISE/WISE.W3
3126748977611495936	WISE/WISE.W1
3128813203316883456	WISE/WISE.W3
3129234045689550976	WISE/WISE.W1
3324289470039249408	WISE/WISE.W1
3352222215048693504	WISE/WISE.W3
3355188117603280640	WISE/WISE.W1
4064497976508146688	WISE/WISE.W2
428891315316060160	WISE/WISE.W1
435067993681192320	UKIRT/UKIDSS.K
464638293759397632	WISE/WISE.W1
465827037629837696	WISE/WISE.W4
5254330709292306560	WISE/WISE.W1
5254332770876859008	WISE/WISE.W4
5310688514207181824	WISE/WISE.W1
5333062854296532480	WISE/WISE.W4
5335935942551982080	WISE/WISE.W2
5337166162957067648	WISE/WISE.W1
5337376891236690560	WISE/WISE.W3
5338495403810748416	AKARI/FIS.WIDE-S
5338502202699086080	WISE/WISE.W1
5339377246496587392	WISE/WISE.W1
5339411846756340736	WISE/WISE.W1
5339894291828433024	WISE/WISE.W1
5339935695306646016	WISE/WISE.W3
5339942189297580416	WISE/WISE.W3
5351221941647302912	WISE/WISE.W1
5351241973377009280	WISE/WISE.W1
5352004244161147136	WISE/WISE.W1
546642482291623168	WISE/WISE.W3
5518730442165840768	WISE/WISE.W1
5520118060206928896	WISE/WISE.W1
5547527132743054336	WISE/WISE.W1
5547599769226387840	WISE/WISE.W3
5547978963304967296	WISE/WISE.W1
5619904272346555520	WISE/WISE.W3
5715306662901791232	WISE/WISE.W2
5865056126594144128	WISE/WISE.W2
6054029567979605632	WISE/WISE.W1

Table B.4 List of the CP Stars and candidates that show IR excess.

Gaia DR3 ID	Filter where excess starts
6054273556477806976	WISE/WISE.W1
6054329940813382016	WISE/WISE.W2
6054868770221377920	Spitzer/IRAC.I4
6054918488763944832	WISE/WISE.W2
6056528822281714816	WISE/WISE.W1

Table B.4 List of the CP Stars and candidates that show IR excess.

B.5. CP stars with Hα emission

Table B.5.: CP candidates that show emission lines. The columns are (1) *Gaia* DR3 ID, (2) LAMOST ID, (3) right ascension α in degrees, (4) declination δ in degrees, (5) parallax ϖ and parallax error σ_{ϖ}, (6) the colour $(g1_{-}y)$ from the synthetic photometry, (7) the Hα index, (8)-(10) the spectral types derived from MKCLASS

***Gaia* DR3 ID**	**LAMOST**	α	δ	$\varpi \pm \sigma_{\varpi}$	$(g_1 - y)$	Hα	`libr18`	`libnor36`	`libr18_225`
183576114939066752	J052117.64+345221.5	80.324	34.873	0.325 ± 0.03	9.529	1.903	kB9hF0mK0 Eu	B9.5 III	kB9.5hF0mG2 Eu
3131334967590689536	J063207.38+045455.8	98.031	4.916	0.649 ± 0.017	11.703	1.729	F0 mB5 V Lam Boo	B7 V	kB8hF0mK0 Eu
182636268718056576	J052815.47+342525.6	82.064	34.424	0.489 ± 0.02	9.835	1.486	B4 IV-V	B4 V	kB7hF2mF9
2059202695503955584	J200754.27+361314.1	301.976	36.221	0.316 ± 0.022	9.638	1.406	kA2hA3mA6	A1 IV	kA2hA3mA7
2007069351654097664	J225100.01+570219.6	342.75	57.039	0.297 ± 0.011	9.616	1.326	kB9.5hF0mG2 Eu	B9 II-III	kA0hF0mG8 Eu
182694783351830912	J052405.96+340124.2	81.025	34.023	0.411 ± 0.016	9.041	1.668	B9 III	B9.5 II-III	kA0hF1mG2
3343027622077611392	J055508.01+115959.2	88.783	12	0.639 ± 0.025	9.763	1.851	F0 mB8 V Lam Boo	B9 IV	F0 mA1 V metal-weak
182635620182511744	J052805.13+342130.3	82.021	34.358	0.461 ± 0.015	9.466	1.871	B6 V	B7 V	kB9hF1mK0 Eu
1979250470521255424	J214103.58+503109.8	325.265	50.519	0.241 ± 0.019	9.172	1.691	B9.5 II-III	A0 II-III	kA0hF0mA5 Eu
3131335040608985216	J063213.98+045514.2	98.058	4.921	0.671 ± 0.017	12.859	1.57	B8 IV Si	emission-line?	F1 V Fe-0.8
182659976937528320	J052819.83+342720.1	82.083	34.456	0.803 ± 0.016	10.12	1.526	kA2hF5mK0	A2 V	kA2hA3mK0 Eu
3372466255638764928	J062601.84+194004.7	96.508	19.668	0.275 ± 0.018	9.576	1.723	kB9hF0mK0 Eu	B9 III	kB9.5hF0mK0 Eu

“Meddl off.”